DEVELOPMENT OF STRETCHABLE SENSORS FOR ENHANCED SHEAR CHARACTERIZATION OF WOVEN FABRIC COMPOSITES

by

Hossein Montazerianoliaee

A THESIS SUBMITTED IN PARTIAL FULFILLMENT OF

THE REQUIREMENTS FOR THE DEGREE OF

MASTER OF APPLIED SCIENCE

in

THE COLLEGE OF GRADUATE STUDIES

(Mechanical Engineering)

THE UNIVERSITY OF BRITISH COLUMBIA

(Okanagan)

June 2018

The following individuals certify that they have read, and recommend to the College of Graduate Studies for acceptance, a thesis/dissertation entitled:

DEVELOPMENT OF STRETCHABLE SENSORS FOR ENHANCED SHEAR CHARACTERIZATION OF WOVEN FABRIC COMPOSITES

submitted by Hossein Montazerianoliaee in partial fulfillment of the requirements of

the degree of Master of Applied Science.

Dr. Abbas. S. Milani, School of Engineering

Supervisor

Dr. Mina Hoorfar, School of Engineering

Co-supervisor

Dr. Homayoun Najjaran, School of Engineering

Supervisory Committee Member

Dr. Shahria Alam, School of Engineering

Supervisory Committee Member

Dr. Ian Foulds, School of Engineering

University Examiner

Abstract

Shear is known to be the dominant mode of deformation in woven fabric composites when forming complex, doubly-curved parts. Picture frame (PF) testing has been widely employed in the literature to quantify the mechanical properties of woven fabrics under shearing, albite a number of uncertainty factors present during this test set-up. In the present study, common sources of such uncertainties (imperfections) are first classified and their effects on characterization data are studied, through both analytical and numerical approaches. Namely, the mechanical response of fabrics under PF testing is recognized to be highly sensitive to the imperfections stemmed from either misplacing the fabric into the fixture, or deviation of fixture from an ideal shearing frame. In addition, to prevent the fabric/fixture contacts, corner cut-offs are usually introduced to the fabric by experimenter during PF testing, exacerbating the shear angle mismatches between the sample center and fixture frame.

Upon the above general, theoretical assessment of PF test imperfections, their adverse effects on shear characterization of fabrics have been experimentally demonstrated through novel sensors integrated within the yarns of a typical polypropylene/glass plain weave, capturing the local tensile deformation of the material during the shear tests. Finally, a novel frameless picture frame (FPF) shear testing approach was introduced for mitigating of imperfections as seen in the conventional PF test. In the new set-up, the frame is inscribed on the sample itself by locally consolidating the fabric at regions corresponding to the clamping areas in the conventional PF. A high controllability was realized over the sample during preparation and installation phases of the new test set-up. Furthermore, high shear strain deformation behavior as well as normalized force-shear angle response of the fabric was assessed during the FPF testing and was proven to be more consistent than the PF test, by means of eliminating sample size effects and significantly improving the data repeatability under cyclic loads. The embedded PDMS/CCF sensor into the fabric further confirmed the performance of the new test by monitoring local yarn strain level; it was significantly lower in a needle integrated version of FPF test when compared to the PF test.

Lay Summary

Woven fabric composites have recently received a great deal of attention by industries as they offer superior mechanical properties, specifically regarding the impact resistance of lightweight structures. Designing optimal forming processes is usually obtained through basic characterization tests at the laboratory (test coupon) level. However, due to the complex multi-scale nature of deformation in such materials, the current testing methods have been unable to fully reflect the fabrics' mechanical properties. In addition, some of the conventional methods suffer from a high amount of manipulations (sources of uncertainty). In this study, a simple fabric shear testing method has been introduced and its functionality was analytically and experimentally assessed, through locally monitoring the material deformation via sensors integrated into the fabric during the tests. Results suggest that the proposed test method can provide a much more realistic quantification of shear behavior of woven fabrics compared to the conventional methods.

Preface

This work has been organized and developed through regular discussions with my supervisors over the past two years. The thesis consists of multiple chapters derived from a series of papers submitted to the journals for consideration as follows:

1. H. Montazerian, A. Rashidi, A. S. Milani, M. Hoorfar, "Integrated Sensors in Advanced Composites: A Critical Review". (submitted)
2. H. Montazerian. A. Dalili, A. S. Milani, M. Hoorfar, "Piezoresistive Sensing in Carbon Fiber Embedded PDMS Yarns". (submitted)
3. H. Montazerian, A. Rashidi, M. Hoorfar, A. Milani, "A Frameless Picture Frame test with embedded sensor: Mitigation of imperfections in shear characterization of woven fabrics". (submitted)

Chapter 2 is mainly from the above review paper (Paper I) that I wrote during my initial literature search in this research. The introductory parts of this chapter pertinent to the common characterization approaches for shearing behavior of woven fabrics are also included in Paper III.

A version of Chapter 3 is under publication as a paper (Paper III), in which I have been responsible for analytical analysis, implementation of numerical procedure and programming, reporting and analyzing the data. This chapter basically emphasizes the necessity of moving towards a new approach for shear characterization of woven fabrics, by highlighting the severe effects of some common flaws seen in the current shear test methods.

Chapter 4 is the answer to the primary question/goal we attempted to focus on in this research: designing and evaluating a new shear testing method wherein the previous imperfections could be obviated. This chapter is mainly published as Paper II and I have contributed to the design, brainstorming, implementation, and experimental parts of the work, as well as analyzing and reporting the data.

Chapter 5 is mainly based on Paper III and outlines the methods that sensors were fabricated and tailored experimentally for monitoring local deformation (along the yarns) in woven fabrics. In this chapter, a throughout characterization for the utilized sensors has also been provided and I conducted the entire research including executing the experiments, writing and analyzing the data.

Chapter 6 provides an experimental evidence and proves the functionality and effectivity of the proposed new test method. This chapter is primarily a summary of the final sections of Papers II and III. Mr. Armin Rashidi and Mr. Arash Dalili assisted me with the experimental works undertaken in the above mentioned papers.

Table of Contents

Abstract ..... **iii**

Lay Summary ..... **iv**

Preface ..... **v**

Table of Contents ..... **vii**

List of Tables ..... **xi**

List of Figures ..... **xii**

List of Symbols ..... **xv**

List of Abbreviations ..... **xvii**

Acknowledgements ..... **xix**

Dedication ..... **xx**

Chapter 1: Background and thesis organization **1**

1.1 Introduction 1

1.2 Motivation and objectives 3

1.3 Thesis Framework 3

Chapter 2: Literature review **5**

2.1 Characterization of shear behavior of woven composites 5

2.1.1 Bias extension test 5

2.1.2 Picture frame test 6

2.2 Imperfections in picture frame test 6

2.3 Experimental analysis of local deformations: Embedded sensors 7

2.4 Piezoresistive sensors – design and fabrication 8

2.4.1 Principles and working mechanism 9

2.4.2 Carbon-based piezoresistive sensors ... 12

2.4.2.1 Carbon fibers ... 12

2.4.2.2 Carbon Nanotubes ... 15

2.4.2.3 Graphene ... 20

2.5 Integrated sensors with composites for SHM ... 23

2.5.1 Structural degradation of composites due to embedded sensors ... 23

2.5.2 Application of piezoresistive composites for SHM of composites ... 25

2.5.2.1 Self-sensing piezoresistive structures ... 25

2.5.2.2 Piezoresistive yarns integrated with materials and structures ... 27

Chapter 3: Analytical analysis of imperfection effects in conventional picture frame test ..33

3.1 Overview ... 33

3.2 Analytical approaches for analysis of imperfection effects ... 33

3.3 An insight into the imperfection sources ... 36

3.4 Imperfection Case 1: Oriented fabric misplacement into the test fixture frame ... 38

3.4.1 Pre-rotated fabric misplacement ... 39

3.4.2 Pre-sheared fabric misplacement: operator error ... 40

3.5 Imperfection Case 1I: Incoincidence of the clamping edge and ideal shear frame ... 42

3.6 Imperfection Case III: Frame/fabric shear angle mismatch ... 44

3.7 Summary of findings ... 47

Chapter 4: Frameless picture frame test setup: An enhanced approach for mitigating the imperfection effects ... 48

4.1 Overview ... 48

4.2 Standard shear characterization procedure (without sensor embedment) ... 48

4.2.1 Normalization of the PFT ... 49

4.2.2 Normalization of the BET 50

4.3 Conventional picture frame shearing test set-up with embedded sensor 50

4.4 A new frameless shearing test set-up with embedded sensor 51

4.5 A new integrated frameless shearing test set-up with embedded sensor 52

4.6 The novel fixtureless shearing tests versus conventional approaches 53

4.7 Severe deformation mechanisms: wrinkling patterns and yarn bending close to arms 54

4.8 Comparing the normalized force-shear angle behaviors 57

4.9 Summary of findings 59

Chapter 5: Sensor fabrication and characterization for integration with woven fabrics.....60

5.1 Overview 60

5.2 Materials and Methods 60

5.2.1 Materials 60

5.2.2 Sensor fabrication procedure 61

5.2.3 Characterization 62

5.3 Results 63

5.3.1 Electrical conductivity and percolation threshold 63

5.3.2 Piezoresistive behavior under cyclic loads 64

5.3.3 Sensitivity analysis in cyclic loading 66

5.3.4 Piezoresistive non-linearity: Piezoresistivity transition in cyclic loading 67

5.3.5 Electrical and mechanical relaxation 69

5.3.6 Failure tests 70

5.4 Discussion 72

5.4.1 Conductivity characterization 72

5.4.2 Structural characterization prior to loading 72

5.4.3 Failure mechanism 73

5.4.4 Piezoresistive mechanism under cyclic loading 74

5.5 Summary of findings 77

Chapter 6: Sensor integrated picture frame test: Monitoring yarn tension 79

6.1 Overview 79

6.2 Attaching the sensors to the fabric 79

6.3 Sensor response to repeated loading in the conventional picture frame test 80

6.4 Comparing local deformations in conventional versus frameless picture frame tests 81

6.5 Summary of findings 83

Chapter 7: Conclusions and future perspectives 85

7.1 Summary 85

7.2 Contribution to knowledge 89

7.3 Future work 89

Bibliography 91

List of Tables

Table 2.1. The piezoresistive sensitivity of conductive composites containing carbon nanotube (CNT) fillers with respect to the effects of carbon mass fraction, the range of applied strain, and sample sizes. 16

Table 5.1. The mechanical properties obtained based on the stress-strain response curves for the composites with different CCF contents. 71

List of Figures

Figure 1.1. The deformation mechanism during forming process of composite woven fabrics and FE optimization procedure for designing the manufacturing parameters 2

Figure 1.2. Organization of the thesis 4

Figure 2.1. The electrical configurations used for the measurement of the resistance change in piezoresistive materials 10

Figure 2.2. Carbon-based piezoresistance materials characterization 13

Figure 2.3. Piezoresistive and mechanical behavior of MWCNT/SPU composites.................... 19

Figure 2.4. Methods utilized for fabricating and processing graphene-based piezoresistive sensors 22

Figure 2.5. Cross-sectional SEM images of the sensors embedded into a composite structure ... 24

Figure 2.6. Application of self-sensing CNT/cement composites in traffic monitoring. 26

Figure 2.7. SEM image of a self-monitoring ceramic-graphene composite fabricated by combining graphene foams with pre-ceramic polymers and spark plasma sintering. 27

Figure 2.8. Examples of methods used for integrating yarn piezoresistive materials for health monitoring of composites.. 29

Figure 2.9. Integration of the carbon fiber (CF) sensors and glass fibers (GF) coated by conductive silver paint into the woven reinforcement textile fabrics. 30

Figure 2.10. SHM application examples by integrating piezoresistive yarns into the woven composite material structures.. 31

Figure 3.1. Illustration of the two approaches taken for analysis of deformation field within the fabric 35

Figure 3.2. Schematic illustration of the imperfection parameters in the conventional picture frame setup and their associated deformation mechanisms at the onset of the test (left figures, γ=0°) and after applying the shear load (right figures, γ°) 37

Figure 3.3. The effects of pre-rotated fabric misplacement as a case of imperfection on shear angle distribution and strain along the yarns 40

Figure 3.4. The mechanical effects of pre-sheared fabric misplacement imperfection case 41

Figure 3.5. The shear angle gradient and axial yarn strain distribution as a result of offset of clamping edge and the shear frame central lines. 44

Figure 3.6. Effect of fabric-frame shear angle mismatch on mechanical behavior of fabric 46

Figure 4.1. Sample preparation process in the conventional picture frame testing procedure. A fabric with corner cut-offs is clamped and mounted to the fixture 51

Figure 4.2. Sample preparation procedure in the frameless picture frame testing approach 52

Figure 4.3. Sample preparation procedure in the needle integrated frameless picture frame testing procedure 53

Figure 4.4. Illustration of severe defect formation mechanisms in woven fabrics 56

Figure 4.5. The shear response (normalized shear force versus shear angle) of the fabrics obtained following different testing methods. 58

Figure 5.1. Overview of the steps followed for fabrication and electromechanical evaluation of the CCF/PDMS sensors. 61

Figure 5.2. Variation in the volume electrical conductivity as a function of the weight fraction of the CCF content. 64

Figure 5.3. First 10 cycles electromechanical behavior of the CCF/PDMS composites at 3% strain amplitude 66

Figure 5.4. Loading gauge factor results obtained after the first-cycle for the CCF/PDMS composite sensors with different CCF contents at cyclic loads 67

Figure 5.5. Variation in the normalized transition strain ($\varepsilon_t/\varepsilon_0$) as a function of loading cycles at 3% strain amplitude 68

Figure 5.6. The relaxation behavior of the CCF/PDMS composites. 70

Figure 5.7. Resistance change and tensile stress induced by tensile loading 71

Figure 5.8. SEM images of the failure surface for the 4.83 wt.% CCF content in CCF/PDMS composite. 74

Figure 5.9. Fiber deformation in the PDMS matrix observed for in-situ macroscopic images 75

Figure 6.1. The change in the resistance of the CCF/PDMS sensors, integrated into the composite glass fiber/epoxy fabrics, during the picture frame test setup 81

Figure 6.2. The sensor signals measured during the tests for the new test setups 83

List of Symbols

V_{out}	The output voltage from the Wheatstone bridge
V_{bridge}	The input voltage applied to the Wheatstone bridge
R	Electrical Resistance
ρ	Material electrical resistivity
L	Length
A	Cross-sectional are
υ	Poisson's ratio
ε_L	The dependency of the relative resistance to the longitudinal direction
ε_T	The dependency of the relative resistance to the transverse direction
γ_L	elasto-resistance coefficients in the longitudinal direction
γ_T	elasto-resistance coefficients in the transverse direction
GF	Gauge factor
π_L	Piezoresistance coefficient
σ_L	Electrical conductivity per unit of longitudinal stress
E	Modulus of elasticity
$\boldsymbol{F}$	deformation gradient matrix
x_i	displacement fiend
X_j	the coordinates in the non-deformed system located on the diagonals of frame
$\boldsymbol{C}$	The Cauchy-Green tensor
$\boldsymbol{E}$	Green-Lagrange strain tensor
w	Fabric sample size in picture frame test
L	Length of the picture frame fixture

L'	Instantaneous length of the yarns of the fabric in picture frame test
δ_i	Misplacement corresponding to each arm of the picture frame fixture
h	Fabric gripping line/ideal shear frame offset
μ	Mismatch factor between the fabric and frame shear angle
γ_{center}	Shear angle at the center point of the fabric
γ_{frame}	Shear angle of the frame
$\varepsilon_{X_i'}$	The strain along the yarns
$\gamma_{ext.,arm}$	The extremum of shear angle over the arm regions
$\varepsilon_{yarn_{max}}$	Maximum induced strain along the yarns
θ	Frame shear angel
δ	Cross-head displacement
$F_{normalized}$	Normalized force
F	Recorded force
F'	Fixture force without mounting a sample
σ_V	Volume conductivity
σ_e	Electrical conductivity
P_c	Percolation threshold
P	Filler concentration
n	Exponent coefficient (or the dimensionality of the conductive network)

List of Abbreviations

BET	Bias Extension Test
CCF	Chopped Carbon Fiber
CF	Carbon Fiber
CNT	Carbon Nanotube
CVD	Chemical Vapor Deposition
DIC	Digital Image Correlation
DMF	Dimethylformamide
ETC-PTHF	Elastomeric triisocyanate-crosslinked polytetrahydrofuran
FEA	Finite Element Analysis
FPF	Frameless Picture Frame (test)
GF	Gauge Factor
GNP	Graphene Nanoplatelets
MEMS	Microelectromechanical Systems
MKF	multi-layered flat-bed weft-knitted fabric
MWCNT	Multi Wall Carbon Nanotube
NCF	Non-crimp Fabric
PAN	polyacrylonitrile-based carbon fibers
PDMS	Polydimethylsiloxane
PEDOT:PSS	poly(3,4-ethylene dioxythiophene):poly(styrene sulfonate)
PET	polyethylene terephthalate
PFT	Picture Frame Test
PJN	Pin Joint Network

PMMA	Poly(methyl methacrylate)
PP	Polypropylene
PVDF	poly(vinylidene fluoride)
PZT	Lead zirconate titanate
SDP	spray deposition modeling
SEM	Scanning Electron Microscopy
SHM	Structural Health Monitoring
SPU	Segmented Polyurethane
SWCNT	Single Wall Carbon Nanotube
TISP	thermal induced phase separation
TPU	Thermoplastic Polyurethane
TWINTEX	Commercial name for comingled E-glass/Polypropylene fabric tested
UHMWPE	Ultra-high-molecular-weight polyethylene

Acknowledgements

I would like to take this opportunity to express my sincere gratitude to my outstanding supervisors, Professor Abbas S. Milani and Professor Mina Hoorfar who steered my thoughts in the right direction from day one and assisted me to thrive in my MASc research. They have thought me many inspiring lessons, not only in my professional academic life, but also in my personal life as their helpful pieces of advice have always provided me with wisdom. Their endless support specially when brainstorming in our monthly update meetings and commenting on my written works line-by-line, notably added to my research motivation and drove me to work harder and practice the effective ways of academic presentation for my future career.

I would like to thank other faculty members at UBC, particularly Dr. Foulds as well as my committee members Dr. Najjaran and Dr. Alam for their valuable guidance and advice. I have been truly inspired by their constructive comments and enjoyed discussing with them my research at different occasions, including the committee meetings and the courses I took.

Many thanks also go to our lab managers Mr. Bryn Crawford and Allen O'brien for facilitating my experiments and their support in our update meetings. Special thanks are also due to Mr. Armin Rashidi, Mr. Arash Dalili, Mr. Mahyar Mohaghegh, Mr. Milad Ramezankhani, my friends and lab-mates at UBC, who tirelessly helped me during this research and made our research groups a great environment to work in.

Above all, none of this work could have happened without my family. I am indebted to my parents for all of their spiritual support and encouragements during the entire journey of my education.

For my beloved parents for all their support and sacrifices to put me through the best education possible…

Chapter 1: Background and thesis organization

1.1 Introduction

The superior mechanical and thermal properties of composite materials have made them a promising material candidate in several industrial sectors including aerospace, automotive, marine, and sports. This high interest is originated from the superior design solutions provided by composites due to their lightweight and high strength properties [1, 2]. However, their complex (multi-scale) material structural nature under mechanical loads has left many questions for the researchers and process designers in terms of predicting their mechanical response [3].

In particular, when it comes to manufacturing and forming woven fabric reinforced composite parts, a combination of shear as well as axial deformations develop over the fabric contribute to conform the fabric to the shape of interest (Figure 1.1). In order to design the optimal manufacturing process, predictive tools are required to reduce time and cost. Today, numerical predictive methods such as finite element analysis (FEA) are the main tools for process design in forming complex-shaped composite parts, which are employed to find the optimum fabrication parameters and yield defect-free forming processes [4]. For an accurate prediction of manufacturing defects such as wrinkles, realistic mechanical responses of the material under shear or axial loading are required in order to define material models as an input for FEA.

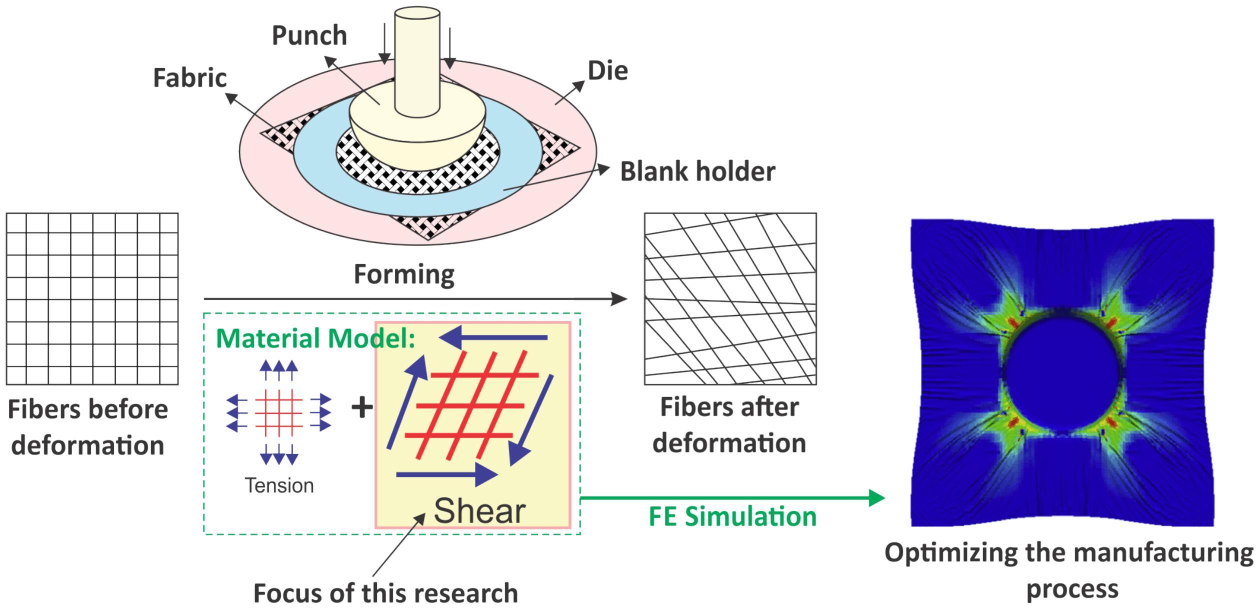

Figure 1.1. The deformation mechanism during forming process of composite woven fabrics and FE optimization procedure for designing the manufacturing parameters. FE analysis requires an accurate material model to precisely predict the manufacturing defects. This can be achieved through an ideal characterization results especially shear behavior of the fabric due to its significant role during the forming.

Severe deformation defects, e.g. wrinkling when forming woven composite fabrics, is basically stemmed from local deviations of the desired deformation modes (e.g. pure shear) as a result of e.g. rotational slippage at the fiber yarns cross-overs [5]. Understanding such defect mechanisms and establishing proper post-processing methods for characterization/test data analysis, such as appropriate force normalization approaches, are mostly sought in the laboratory-scale studies and are yet to be generalized for industrial applications.

Since the lower shear rigid the shearing mode, the deformation in woven fabrics when forming is primarily originated from shear mode of deformation. A few test methods including bias extension test (BET) [6] and picture frame test (PFT) [7] have been widely employed in the literature to characterize shear properties of the fabrics. These methods, however, have been reported to be also vulnerable to multiple test imperfections, the effects of which can be magnified in the characterization/output results. In turn, this can inhibit developing accurate material models for FEA of woven fabrics.

During the last decade, embedded sensors have been exploited to get insight into the structural evolutions of advanced composites under mechanical loads. Although the emphasis of the current state-of-art research in this area has been primarily on the health monitoring of structures during ’service’ [8], their unique capability in addressing the composites behavior during characterization tests has been neglected or received minimal attention. In particular, it is believed the stretchable strain sensors can be a good potential to uncover some of the unknown mechanisms behind the deformation of woven composite materials at large deformation ranges.

1.2 Motivation and objectives

For shear characterization of woven fabrics, the PFT is believed to have several advantages over BET, as in the latter case the sample is formed into three regions with different shear angles and hence a more complicated force normalization procedure is required [7]. In PFT, however, the effect of potential imperfections such as unintentional axial tension/compression along the yarns can cause deviations from ‘pure’ global shearing. It is of great importance that the standard shear tests reflect the pure shear behavior of woven fabrics for material design and FEA purposes. In addition, it is believed that the accuracy of fabric characterization tests can be better verifies at local deformation levels by application of embedded sensing techniques. Hence, the main objectives of the present study are defined as:

(1) better identify and model the sources of uncertainty (imperfections) in the PFT;

(2) propose an enhanced alternative characterization test to relieve most of the above uncertainty sources; and

(3) design and fabricate stretchable yarn-like sensors that can be embedded into the fabrics with sufficient gauge factors to show the effectiveness of the proposed test, and correlate the local yarn axial deformations to the global force measurements.

1.3 Thesis Framework

This thesis is organized based on the objectives outlined above. Chapter 2 defines the basic concepts of mechanical characterization in woven fabrics in details. In addition, a detailed review of the sensor fabrication, characterization, and application based on piezoresistive materials is presented. Chapter 3 is focused on the classification and identification of the sources of imperfections in PFT followed by an analytical study of their effects in terms of the induced mechanical strains due to the identified imperfections. A new testing method has also been proposed in Chapter 4, with an emphasis on mitigating the influence of imperfections. In order to develop an experimental tool for experimentally monitoring and verifying the new testing approach, a yarn-like sensor has been fabricated and fully characterized in terms of its sensitivity and stretchability in Chapter 5. The practical results of the sensors integrated with the fabrics subjected to shear loading in the presence of interpretations, are presented in Chapter 6, which led to new understandings of the fabric deformations. Figure 1.2 demonstrates the organization and flowchart of the chapters presented in this thesis.

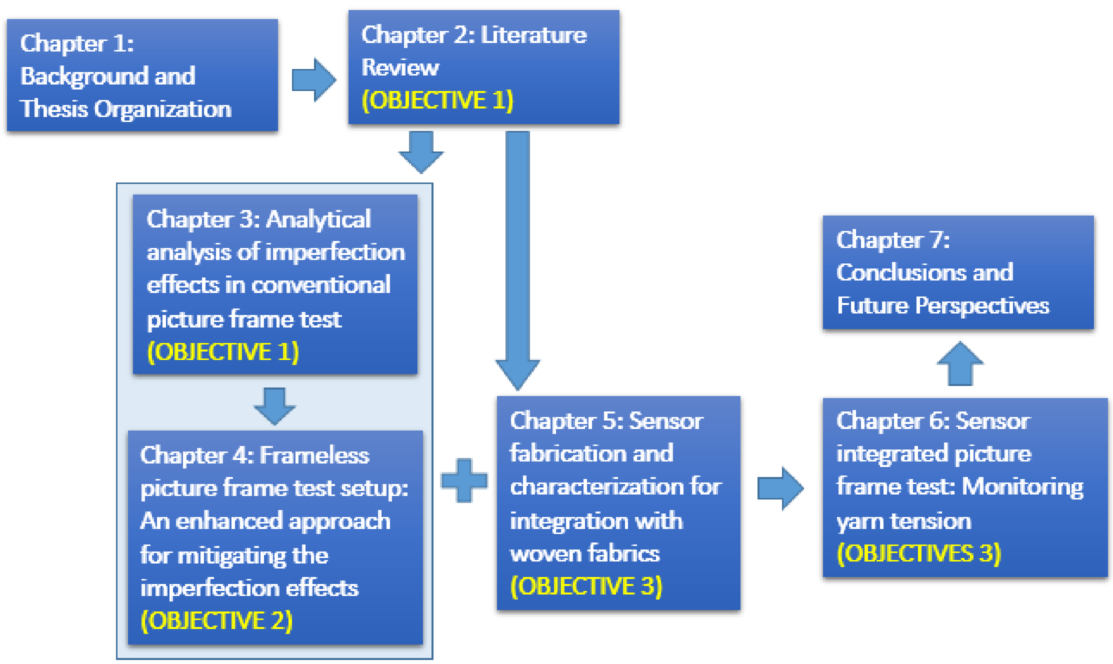

Figure 1.2. Organization of the thesis.

Chapter 2: Literature review

2.1 Characterization of shear behavior of woven composites

In the current state-of-art of composite fabrics' research and technology, the need for highly accurate prediction of the material behavior is increasingly growing for applications such as forming process development [9-13]. Particularly, when it comes to woven fabric structures wherein the yarns undergo large, multi-scale deformations, gaining a deep insight into the underlying mechanical characteristics and deformation mechanisms is essential for developing the predictive material models [14-17]. The forming process of woven composites from two-dimensional plies to three-dimensional composite parts is essentially facilitated by large shear deformation within the fabrics [5, 18-21]. Hence, the shearing properties, as well as deformation analysis of fabrics, have been extensively addressed in the literature, primarily through the bias extension and picture frame test setups. Despite many attempts made to normalize the fabrics shear responses and provide data comparability between these tests [22], there still exists no fully standardized testing procedure for fabric shearing characterization owing to the contribution of deformation mechanisms other than pure shear in the current test setups.

2.1.1 Bias extension test

In the bias extension test (BET), a fully clamped rectangular specimen (normally with the aspect ratio ≥ 2) is subjected to tension while the warp and weft yarns initially form a +45˚/-45˚ angle relative to the loading direction [23-25]. As a result, a non-homogeneous deformation involving three distinct regions (i.e. no shear, half-sheared, and fully sheared) are developed over the fabric sample during loading [26]. Besides, a significant yarn slippage [27-29] (or relative motions at fabric crossovers), as well as intra-tow deformations [30], can lead the shear angle in the central region not to fully follow the gauge length, especially at higher shear angles (e.g. after around 35˚ for a thermosetting and 50˚ for a thermoplastic fabric reported in [31]). Thus, time-consuming and costly visual methods such as digital image correlation (DIC) are often recommended for correlating the force to shear angle during fabric shear tests [32-35]. Nonetheless, the image-based results may not be reliable enough once out-of-plane deformation, namely wrinkling, starts forming in the test specimens (for instance, at shear angles as low as 18˚ in "B1 fabrics" reported in [32]).

2.1.2 Picture frame test

Picture frame test (PFT) involves a pin-jointed square frame where the shearing is directly applied to the fabric boundaries mounted on the fixture arms and by pulling the frame diagonally in one direction [22, 36]. Many researchers are of the opinion that PFT provides a more fundamental understanding of the fabrics 'pure' shear behavior [31]. Besides, in this test, it is feasible to directly control the shearing rate through the cross-head displacement speed (for the normalization purposes). Nevertheless, the PFT is not also free of drawbacks: not only the test results are highly sensitive to the type of clamping (e.g. full clamping vs. needle clamping, etc.) [37], but also even small amounts of imperfections during the sample preparation and mounting (e.g. misalignment or loose/tight mounting etc.) can bring about a high tension/compression into the yarns additional to the desired pure shear, especially at higher shear angles [31, 32, 38, 39].

2.2 Imperfections in picture frame test

It has been hypothesized that force-displacement in a PFT ideally commences with a low shear modulus resulted from fiber-fiber friction at crossovers, followed by a significant load increase at which point the fabric densification (yarn locking) and thereby wrinkles are developed [40]. However, apart from the wrinkling caused by fabric densification, early wrinkling due to the lateral compression of the fabrics is a common issue in the PFT [37, 41]. Moreover, the architecture of picture frame fixtures typically implies introducing corner cut-offs in the test specimen to allow higher shear angles without the fibers touching the fixture arms [37]. This itself divides the fabric into a central region encompassed with four arm regions, through which fixture/global shearing is supposed to transfer to the central area. However, depending on the relative size of the arms/cut-offs and owing to the inherently lower shear rigidity of the arms relative to the central region (since one family of yarns are free-ended in each arm due to the cut-offs), shearing deformation may not be fully uniformly distributed over the sample. Namely, compared to the fixture (global) shear angle, it is possible that the arms undergo a higher shearing while a lower shearing is transferred to the central region [42]. On the other hand, it has been revealed that bending of fiber yarns close to the fixture grips can cause a totally opposite effect of heterogeneous shearing in the samples such that, in comparison with the fixture shear angle, the arms tend to be kept less sheared and instead, a higher shear angle is transferred to the central region (especially in the case of small fabric cut-offs) [43]. Although many approaches have been implemented to relieve the yarn bending close to the grips (e.g. using needle clamping instead of fully bolted clamping [37], removing the perpendicular yarns from the arms [37] etc.), still there exist the evidence of bending in the current test setups [15, 41]. It is worth noting removing the yarns after mounting the fabric remarkably changes the tightness of the fabric [44], yet it is believed to prevent the fabric from early wrinkling during the test [22]. Due to such imperfections, the wrinkling has been frequently seen to develop in the arm regions of the fabric instead of the central region (as opposed to what is usually observed in the case of bias extension test) [45-49].

In order to obviate the above-reviewed issues during shear characterization of fabrics under the PFT set-ups, a few attempts have been made by manipulating the test/sample structure [50]. For instance, Lebrun et al. [38] proposed a modified version of the PFT in which the fabric sample was constrained to the frame through two very narrow strip tabs close to the joints. Their approach remarkably decreased the misalignment effect in the tests conducted on pre-consolidated fabrics. The setup introduced by Hübner et al. [51] used a needle-based clamping outside the frame in order to both let the fibers rotate more freely as well as not require corner cut-offs in the sample. Nevertheless, there exists evidence of yarn bending adjacent to the arms while in both cases, still, a metallic picture frame needed to be fabricated, carefully aligned, and installed in a universal testing machine.

2.3 Experimental analysis of local deformations: Embedded sensors

The advent of stretchable piezoresistive sensors have provided the possibility to fabricate and implement low cost and sensitive resistive sensors into materials, which can be used to monitor local deformations in structures of interest. Sensors embedded into structures can reveal how deformation at local levels develops as specific to the loading applied and the material employed. It is worth noting that the sensors embedded into a structural material can be used for monitoring the health of a structure in service (i.e. after the part is manufactured), and/or to monitor the material behavior during the manufacturing/forming itself, while the latter is mostly characterized in the laboratory-scale tests. For this purpose, conventional foil strain gauges, however, are limited due to the lack of high stretchability, which can significantly affect the characterization test results. The recent advances in resistive sensor development have suggested new possibilities to tailor structural sensors in a way that by far they can less perturb the mechanical properties of the material itself; since these sensors can be made highly stretchable such that once embedded into the material, they do not much change the magnitude of global loads. In addition, mechanically compatible electrodes can be applied to further ascertain minimal structural manipulations during the sensor attachment procedures. In the following sections more details on the principles, basics, design, and fabrication processes associated with the piezoresistive sensors are reviewed.

2.4 Piezoresistive sensors – design and fabrication

Piezoresistive transducers are described as materials in which the resistance varies under application of mechanical strains; unlike the piezoelectric materials which are charged under mechanical loadings. Due to the high conductivity of filler elements (such as carbon, silicon), a combination of such materials with polymeric as well as cement matrices allows for processing piezoresistive composites playing the role of either a self-sensing structure or an external sensor which can be attached or embedded in a material/structure. Therefore, piezoresistive composite materials have extensively been developed in many ways to optimize their electromechanical properties (e.g. sensitivity, signal reproducibility, mechanical stretchability). Due to their composite nature, mechanical properties of piezoresistive materials have been tailored for a wide range of applications wherein strain sensing is essential. An ongoing research is also being carried out on the effect of temperature, crystal orientation, and dopant type and concentration on the piezoresistive behavior of materials. Therefore, processing approaches and their resulted electromechanical characteristics for different types of carbon and silicon-based piezoresistive structure are reviewed here after introducing the working principles of piezoresistive materials.

2.4.1 Principles and working mechanism

A variety of techniques are available for experimental measurement of the material resistance to mechanical strains as illustrated in Figure 2.1. The piezoresistive material is treated as a resistor in an electrical circuit, and instead of direct measurement of resistance, an output voltage is measured for characterization purposes. Simply, a constant current can be applied to the material to measure the resistance through the transduced voltage. Another circuit configuration involves the material in series with a resistor. A Wheatstone bridge is the most commonly used electric circuit that not only enables monitoring of the small variations of resistance, but also compensates for temperature changes [52]. A Wheatstone bridge can also eliminate the capacitive signals in the output of a piezoelectric resonator [53]. The Wheatstone bridge consists of four resistors and the ratio of the change in the output voltage to the bridge voltage (in case of equal initial resistances (R)) is given by Equation (2.1):

$$\frac{\Delta V_{out}}{V_{bridge}} = \frac{1}{4}\left(\frac{\Delta R_1}{R} - \frac{\Delta R_2}{R} + \frac{\Delta R_3}{R} - \frac{\Delta R_4}{R}\right) \tag{2.1}$$

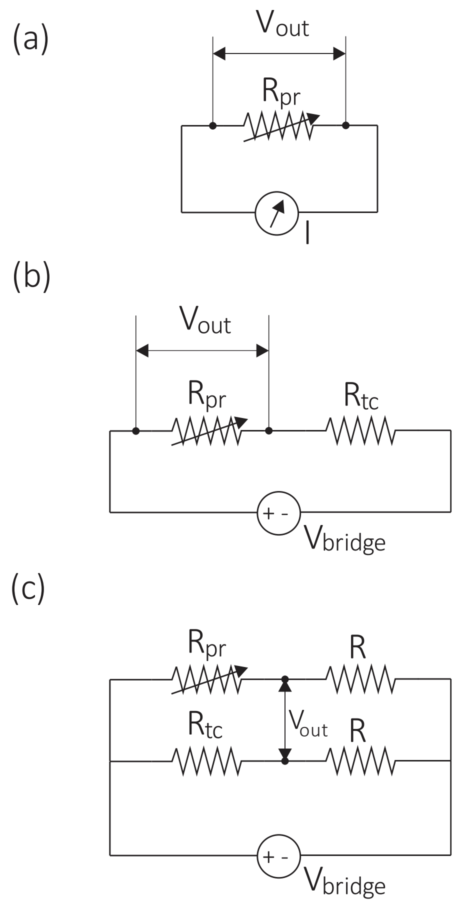

Figure 2.1. The electrical configurations used for the measurement of the resistance change in piezoresistive materials. (a) four-wire (b) voltage divider and (c) Wheatstone bridge circuits.

The theoretical modeling of the piezoresistive behavior of materials is founded based on the equation correlating the geometry of the material to the electrical resistance ($R = \rho A/L$, where ρ represents the material resistivity). For small changes of resistance, the first order Taylor-series expansion of the resistance relation results in Equation (2.2) [54]:

$$\frac{\Delta R}{R} = \frac{\Delta \rho}{\rho} + \frac{\Delta L}{L} - \frac{\Delta A}{A} \tag{2.2}$$

In most metals, the term $\frac{\Delta\rho}{\rho}$ is negligible, and hence, the relative change in the resistivity under uniaxial strain (ε_L) can be expressed as a function of the material Poisson's ratio (v) in the form of Equation (2.3):

$$\frac{\Delta R}{R} = (1 + 2v)\varepsilon_L \tag{2.3}$$

However, the electrical resistance of semiconductor materials basically changes under load due to the resistivity variation. The dependency of the relative resistance to the longitudinal (ε_L) and transverse (ε_T) components of strain can be written in the form of Equation (2.4):

$$\frac{\Delta R}{R} = \gamma_L \varepsilon_L + \gamma_T \varepsilon_T \tag{2.4}$$

where γ_L and γ_T are elasto-resistance coefficients in the longitudinal and transverse directions, respectively. The sensitivity of the piezoresistive materials is characterized with a gauge factor (GF) which is defined by Equation (2.5) [55].

$$GF = \frac{\Delta R/_R}{\varepsilon_L} \tag{2.5}$$

The piezoresistance coefficient is defined as the ratio of the relative change in the electrical conductivity per unit of longitudinal stress (σ_T) as shown by Equation (2.6):

$$\pi_L = \frac{\Delta R/_R}{\sigma_L} \tag{2.6}$$

Combining Equation (2.5) and Equation (2.6) for the linear elastic materials with an elastic modulus of E results in the relationship between the gauge factor (GF) and piezoresistance coefficient as shown in Equation (2.7):

$$GF = E\pi_L \tag{2.7}$$

2.4.2 Carbon-based piezoresistive sensors

Carbon-based materials can be found in different shapes and material forms. Due to their superior electrical conductivity, they have high potential to be combined with various matrix composites. In the following sub-sections, the piezoresistivity of different types of carbon-based materials is discussed and the main challenges and solutions are presented:

2.4.2.1 Carbon fibers

Carbon fibers have high strength, stiffness and temperature resistance, and hence, are typically used to reinforce polymers [56-58], cement [59], and metals [60].They are regarded as *self-sensing* or *self-monitoring* reinforced materials [61]. It is well known that the piezoresistive behavior of carbon fibers is quite depended on the state of the conductive network formed in a matrix. Typically, applying epoxy to carbon fiber increases the electrical resistivity due to the compressive residual stresses induced by epoxy shrunk after curing [62]. For instance, a bare carbon fiber has a gauge factor of 1.9-2.3 while when it is embedded in epoxy and cured, the gauge factor is improved to 217. This value increases to more than 500 when carbon fibers are randomly oriented into a cement-matrix composite [63]. Nevertheless, some conflicting results were reported by Kalashnyk et al. [64] through Raman spectroscopy measurements suggesting higher gauge factors for a bare carbon fiber (values of 1.74 and 1.77) compared to the values obtained for those embedded in epoxy (values of 0.5 and 0.42). This could be, for example, due to the formation of a poor interface between fiber and matrix constitutions. Many studies have revealed the effect of matrix characteristics on the piezoresistive behavior of carbon fiber-based composite materials. A 3D-printing technique was recently employed to embed the continuous carbon fiber tows into the tensile test specimens, resulting in gauge factors ranging from 0.545 to 6.686 [65]. A representation of the fabrication process and the characterization of the resulted sensor is illustrated in Figure 2.2(a-d).

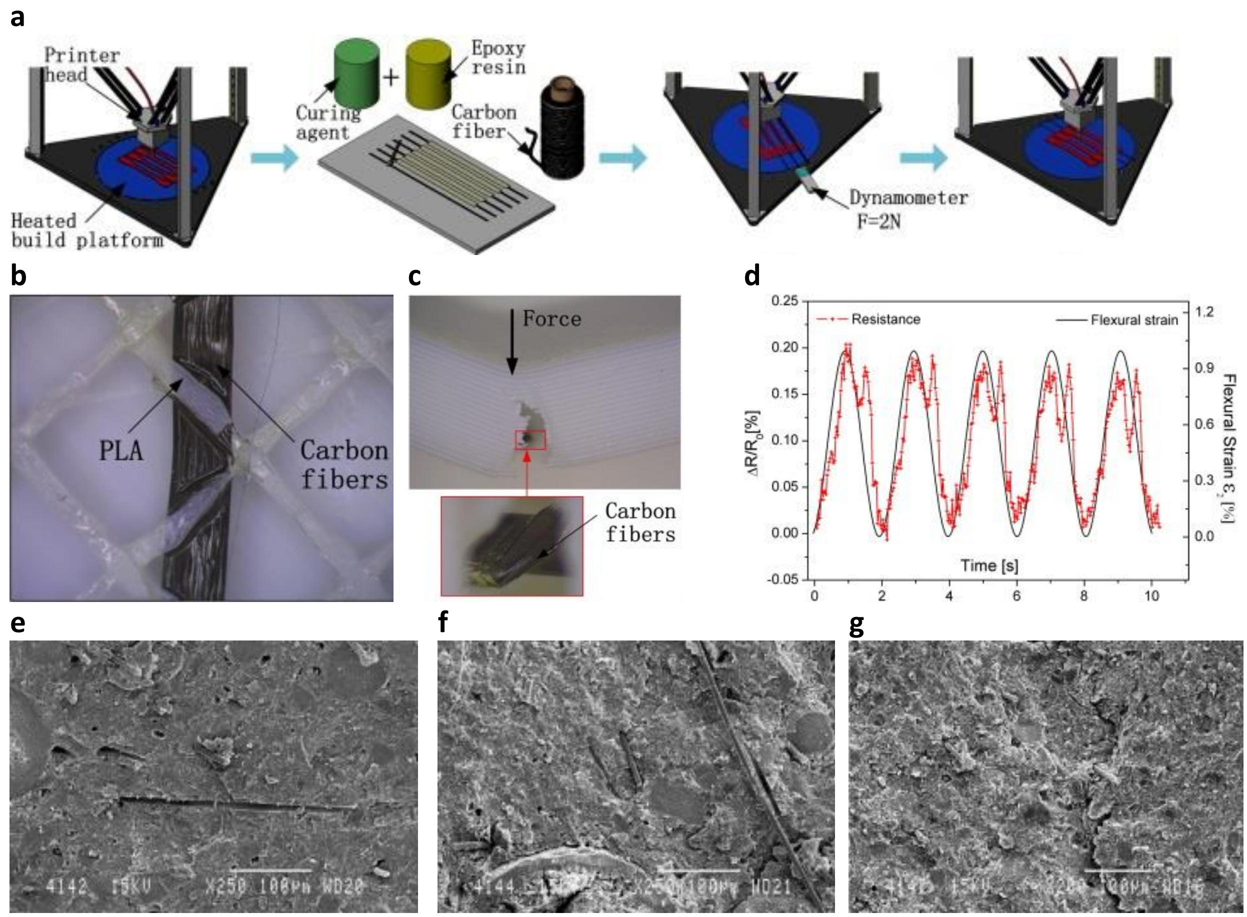

Figure 2.2. Carbon-based piezoresistance materials characterization. (a) Fabrication technique for carbon fiber embedded in the 3D-printed specimens. The carbon fibers are impregnated with epoxy resin adhesive and then manually placed on the print layer while applying 2 N tension to make carbon fibers uniformly placed. Representation of the carbon fiber/PLA interface (b) before and (c) after flexural deformation. (d) The piezoresistive behavior of the embedded carbon fibers after 5 flexural strain cycle, Reproduced with permission. [65] Copyright 2017, Elsevier. SEM images of the piezoresistive materials with the cement paste matrix and chopped carbon fiber lengths of (e) 3 mm, (f) 6 mm and (g) 12 mm, Reproduced with permission. [66] Copyright 2013, Elsevier.

The volume fraction of carbon fibers in the composite materials is one of the parameters crucially affecting the piezoresistive properties [67]. For instance, increasing the carbon fiber content from 15 to 20% in the composites with cementitious fillers have been seen to change the gauge factor from 1250 to 20 [59]. Furthermore, longer fibers are reported to possess greater gauge factors (as reported by Ref. [66] in the case of carbon fiber reinforced cement composites shown in Figure

2.2(e-g)). The longer the fibers, the more manufacturing defects (e.g., porosity), and hence, higher sensitivity. Another parameter affecting the behavior of carbon fiber piezoresistive materials is possibly the length of fibers. Recently, one study has shown a higher non-linear resistance-strain behavior for carbon fibers with a wide length distribution [64].

Piezoresistivity in continuous carbon fibers can be either positive or negative in some loading cases such as in flexural loading due to the presence of compressive and tension regions [68]. Moreover, applying a higher level of loadings is shown to diminish the gauge factor due to the internal micro-damages or irreversible resistance changes which have been evident particularly in cyclic loads [59, 69]. Damage/delamination detection is one of the main applications of carbon fiber contents in nanocomposite materials [70-74]. It is even feasible to estimate the crack location as well as the crack size in a carbon composite laminate using methods such as surface voltage distribution [75]. A number of prodigious studies have been conducted to improve strain sensing and signal processing of carbon fiber based sensors through manipulation of structural parameters and data acquisition system architecture. Saifeldeen et al. [76] stated that signal error compensation can be achieved by using two sets of carbon fiber line sensors. Moreover, a post-tensioning (preferably greater than 200 $\mu\varepsilon$) before applying the resin on the carbon fiber reinforced composite material was seen to considerably enhance the behavior of the sensor in terms of linearity, repeatability in cyclic loading, and fluctuation errors [76-78]. The loading mode can significantly influence the sensing behavior of piezoresistive materials. For instance, an intermittent cyclic loading can result in a higher gauge factor as compared to a continuous cyclic loading [77]. In addition, the electrical resistance typically increases at higher loading cycles due to the initiation and development of internal damages (this behavior was evident in cyclic piezoresistivity of NiNs/Silicone nanocomposite embedded into carbon fiber reinforced plastics although a more consistent behavior was observed for NiNs/Epoxy nanocomposite [79]). Employing an elastic loop test setup, Ramirez et al. [80] addressed the viscoelastic behavior of fibers and its effect on diminishing the electrical resistance at constant strains. They argued that such a viscoelastic behavior is the result of frictional movement of fibers relative to each other within a tow. In addition to the type of loading, the rate of loading can affect the piezoresistive behavior [81]; however, it has shown to have a minimal effect on the piezoresistive properties of polyacrylonitrile-based carbon fibers (PAN) [66]. In addition to loading, the gauge factor for carbon fiber based piezoresistives are also sensitive to temperature [82]; e.g. a composite made of short carbon fibers and vinyl ester resin is thermally stable at temperatures up to 50 °C and thereafter the gauge factor increases with temperature [83].

2.4.2.2 Carbon Nanotubes

Over the past few decades, carbon nanotubes have shown an outstanding potential for piezoresistive devices and materials. Excellent mechanical properties along with thermal and electrical characteristics have made carbon nanotubes one of the best candidates to be used as a filler element in composite materials [84-87]. In the carbon nanotube-based composites, piezoresistivity is basically obtained via sliding/displacement of the nanotubes. Either positive or negative piezoresistivity can be obtained for structures containing carbon nanotubes depending on its wrapping indices [88]. Single wall carbon nanotubes (SWCNT), as well as multiwall carbon nanotubes (MWCNT), are the main elements used to induce piezoresistivity to the composites with polymeric matrices.

Piezoresistive properties of composites fabricated using carbon nanotubes have been studied in combination with different polymeric matrices including epoxy, PDMS, PMMA, polystyrene, polycarbonate [89]. Table 2.1 summarizes the range of sensitivity of piezoresistive materials under full/cyclic tensile loadings for different composites fabricated using carbon nanotubes. As it can be seen, sensitivity highly depends on the matrix material, conductive mass fraction, the type of loading, sample size, as well as the fabrication process. Generally, a higher mass fraction of the conductive filler leads to lower sensitivity. It also diminishes the mechanical properties of the matrix polymer. Hence, an ongoing research is devoted to the development of fabrication processes for composite piezoresistive materials with low percolation threshold [90-92]. For instance, the solvent casting method [93] and aligning carbon nanotubes [94-97] have been successfully employed to form the conductive network at a lower filler mass fraction. Apart from sensitivity, repeatability of CNT-based nanocomposites in cyclic loading is a major concern. The study in Ref. [88] has shown high repeatability in cyclic tensile/compression loadings for MWCNT/epoxy nanocomposites; namely in a small strain range (0.2%) with a gauge factor of up to 78. In another study, the gauge factor for an MWCNT/poly (glycerol sebacate) was found to be significantly dependent on the loading condition (a gauge factor range of -0.5 to -0.8 was reported under tensile loading while a maximum of 42 was observed under 3-point bending) [98].

Table 2.1. The piezoresistive sensitivity of conductive composites containing carbon nanotube (CNT) fillers with respect to the effects of carbon mass fraction, the range of applied strain, and sample sizes.

Matrix	CNT mass fraction (wt. %)	Applied strain	Sample size (mm)	Approx. reported gauge factor	Ref.
Segmented polyurethane (SPU)	4	0-0.1	70×10×0.13	10-5 (varying with cycles)	[99]
Segmented polyurethane	2-6	0.1, 0.5, 1	120×120×0.13	2.16-5223 (varying with strain)	[100]
Polydimethylsiloxane (PDMS)	2.45	0.1	30×5×1	4.36	[101]
Thermoplastic polyurethane (TPU)	2.3-7.1	0-5	20×0.003 fibers	0.2-0.5 (varying with strain)	[102]
Elastomeric triisocyanate-crosslinked polytetrahydrofuran (ETC-PTHF)	15	0.01-5	-	10-8491	[103]
poly(vinylidene fluoride) (PVDF)	0-5	0.006	45×6×1	up to 4.4	[104]

The fabrication processes for integrating carbon nanotubes into other matrices (for the purpose of inducing piezoresistive property) significantly affects the configuration of conductivity network inside the composite materials, and consequently the piezoresistive behavior. There are a large number of fabrication processes (such as mixing and spray coating) for CNT integration into different matrices. For instance, a spray coated SWCNT on the biaxially stretched polyethylene terephthalate (PET) and a polydimethylsiloxane (PDMS) has been shown by Luo et al. [105], wherein they reported a compounding effect of the film thickness when the tensile strain ranged between 20 and 30%. A vast majority of the studies have simply mixed the carbon nanotubes with the matrix in its liquid form and consolidated the composite structure through curing methods. One approach for introducing carbon nanotubes into the thermoplastic polyurethane (TPU) fibers is to disperse CNT in $CHCl_3$ and immerse the fibers into the solution in order to adhere CNTs to the TPU fibers [102]. Moreover, TPU nanocomposites can be obtained by compression molding [106], where TPU is first dissolved into Dimethylformamide (DMF) and then mixed with the carbon content. Then, adding methanol while stirring results in flocculate of the composite that can then be subjected to hot pressing for forming the piezoresistive sensor. Microfabrication techniques can also be employed to fabricate MEMS structures comprising carbon nanotubes for sensing applications. For instance, MWCNT arrays have been formed as cross-contacted electrodes by Li et al. [107] for fabrication of an ultra-high sensitive pressure sensor (with -9.95 kPa^{-1} sensitivity). Carbon nanotube/polymer composites are also adapted to 3D-printing techniques by introducing electrically conductive composite filaments. It has been shown that using spray deposition modeling (SDP), carbon nanotubes can be also printed on the polyurethane substrate and play the role of a piezoresistive material, with gauge factors ranging from 0.61-6.42 (depending on the number of deposited layers) [108]. The piezoresistive behavior is also studied for the fabricated porous nanocomposite structures comprising CNT-thermoplastic polyurethane by Liu et al. [109]. In this study, a moderate piezoresistive recoverability was obtained over a compressive strain range up to 90%, after a mechanical stabilization was applied through cyclic loadings. A few studies also attempted to enhance the piezoresistive behavior by manipulating the dispersion of the conductive filler in the composite. In this regard, the application of an AC electric field (7 kV/m and 60 Hz) to the MWCNT/polysulfone/$CHCl_3$ solution aligned the carbon nanotubes to the direction of the electric field which led to an improved electrical conductivity as well as the sensor sensitivity with respect to the randomly oriented MWCNTs [110]. Furthermore, other methods have been employed for aligning the CNTs in the polymer matrix composites [111] involving magnetic field [112], infiltration [113], shear force [114], mechanical stretching [115] and in-situ polymerization [116].

In the piezoresistive behavior of nano-carbon based composites (especially those with stretchable matrix elements), a positive to negative piezoresistivity *transition* is a common phenomenon [85, 117, 118]. An example of such a behavior is represented in Figure 2.3 for an MWCNT/segmented polyurethane composite. A decay in the relative change of the electrical resistance due to the frequent application of strain can be explained by the time-dependent/viscoelastic behavior of the matrix material (Figure 2.3 (b, d, f)). However, the piezoresistivity alteration (negative to positive piezoresistivity) is seen in some cases/material combination systems as shown in Figure 2.3(g). When these materials are subjected to cyclic loads, on one hand increasing the load cause the electrical network to disconnect along the loading direction leading to increasing the resistance, and on the other hand, the Poisson's effect causes the material to transversely shrink and enhance the conductive network thereby electrical conductivity. At the onset of tension, resistance reduction shows that the transverse shrinkage effect overcomes the unidirectional tension effect. This causes the resistance to drop down to a point where the negative to positive piezoresistivity transition strain occurs. After this transitional point, the resistance starts increasing to a maximum value with loading. Conversely, as the load is removed, the resistance decreases down to another transitional point where piezoresistivity switches from positive to negative. Such a behavior repeats during each cycle of loading and unloading as shown by previous studies (see Figure 2.3). This effect needs to be diminished in nano-carbon based piezoresistive composites [99, 119-124].

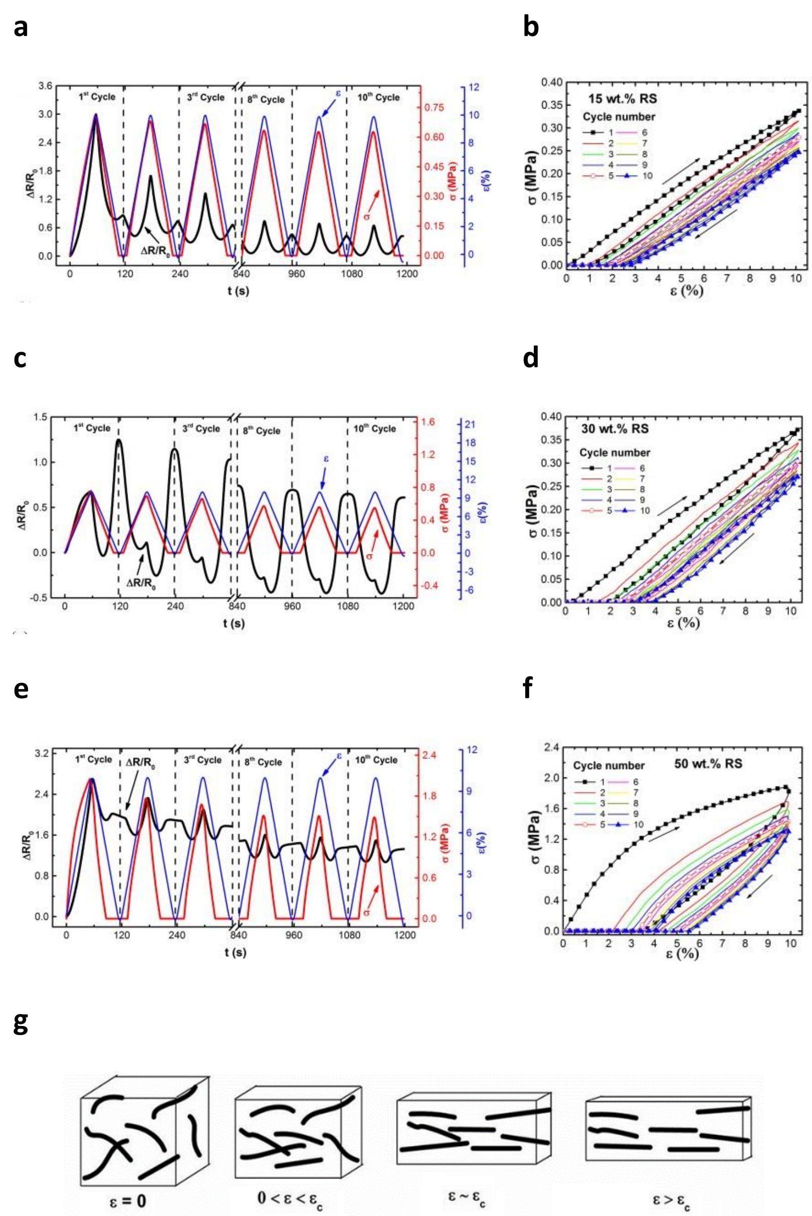

Figure 2.3. Piezoresistive and mechanical behavior of MWCNT/SPU composites. The results for 4 wt% MWCNT/SPU composite are shown for the samples with rigid segment contents of (a,b) 15 wt% (c,d) 30wt% and (e,f) 50%. Negative-to-positive piezoresistivity along with degradation of relative resistance change with strain is due to the permanent deformations caused by viscoelastic behavior as well as the microstructural evolution of conductive network in the composite, Reproduced with permission. [99] Copyright 2016, Elsevier. (g) schematic representation of the fibers at different uniaxial strain stages. Fibers tend to get oriented and compacted due to the Poisson's effect as a result of tensile loading Reproduced with permission. [122] Copyright 2013, WILEY-VCH Verlag GmbH & Co. KGaA, Weinheim.

2.4.2.3 Graphene

Graphene is a 2D carbon nanostructure consisting of highly thin sheets of sp^2 bonded carbon atoms packed densely in a honeycomb lattice structure [125]. Such structure offers promising mechanical, thermal and electrical properties, thereby graphene has found widespread applications in strain sensors, energy technology, aerospace applications, among others [126]. However, one of the main challenging characteristics of graphene is related to its limited stretchability. To overcome this problem, a buckled form of the original graphene structure is used [127]. For instance, graphene ribbons are formed with a uniform and periodic buckled structure on a pre-strained PDMS substrate after removing the pre-strain condition [128]. Integrating rubbery materials with graphene has been used extensively as a promising way for fabricating pressure and load sensors. As an example, elastic graphene-based cellular composites have been fabricated for measuring compressive loads due to its high resistance sensitivity to mechanical compression [129].

One way of fabricating the graphene foam/polydimethylsiloxane (PDMS) composite is infiltrating PDMS into the graphene form, synthesized through chemical vapor deposition on the nickel foam as a template (Figure 2.4(a)) [130, 131]. Furthermore, the thermal induced phase separation (TISP) technique is used to fabricate conductive highly porous (90%) graphene/TPU foams [117]. Given the feasibility of graphite to be grown using methods such as chemical vapor deposition (CVD), a wide variety of fabrication schemes can be developed to control the morphology and structure of graphite in the piezoresistive materials. For instance, gauge factors in the range of 3 orders of magnitude for strain ranges of 2-6% were obtained for graphene woven fabrics integrated into PDMS through the fabrication process shown in Figure 2.4(b) [132]. Such high gauge factor values are extremely desirable specifically for human motion detection and health monitoring applications. Graphite-based nanocomposites have attracted much attention for their high gauge factors. For instance, an epoxy-based nanocomposite with a graphene filler [133] has been used in different applications such as electromagnetic interference, stealth composite coating, and strain sensors. Dispersion properties of graphene and its interface with matrices crucially affect the electromechanical properties of the graphene-based nanocomposites, which are governed by the fabrication process. Moreover, highly stretchable strain sensors (up to 150%) were obtained by dispersion of graphene nanoplatelets (GNP) and stretchable yarns through a layer-by-layer assembly as shown inFigure 2.4(c). In this way, depending on the yarn structure, highly sensitive sensors with a negative sensing response and gauge factors increasing with strain (up to 2000 $\mu\varepsilon$) were achieved [134]. A layer-by-layer spray fabrication method of graphene/polyurethane nanocomposite with magnetite nano-spacers has proven to enhance the sensitivity and robustness of flexible sensors [135]. In another study, cotton fiber films playing the role of supporting substrate for silver nanowires and reduced graphene oxide (that provides dynamic bridging effect), has shown to enhance piezoresistive sensitivity to 5.8 kPa^{-1} [136]. A superparamagnetic composite consisting of PDMS/graphene and Fe_3O_4 (G-F nanosheets) at slightly above the percolation threshold of 3.3 wt.% has shown the high piezoresistive sensitivity of 870. For this purpose, a simple one-step hydrothermal process has been utilized, which is quite advantageous for combining the graphene with various polymeric matrices, and hence, achieving multi-functional composites [137].

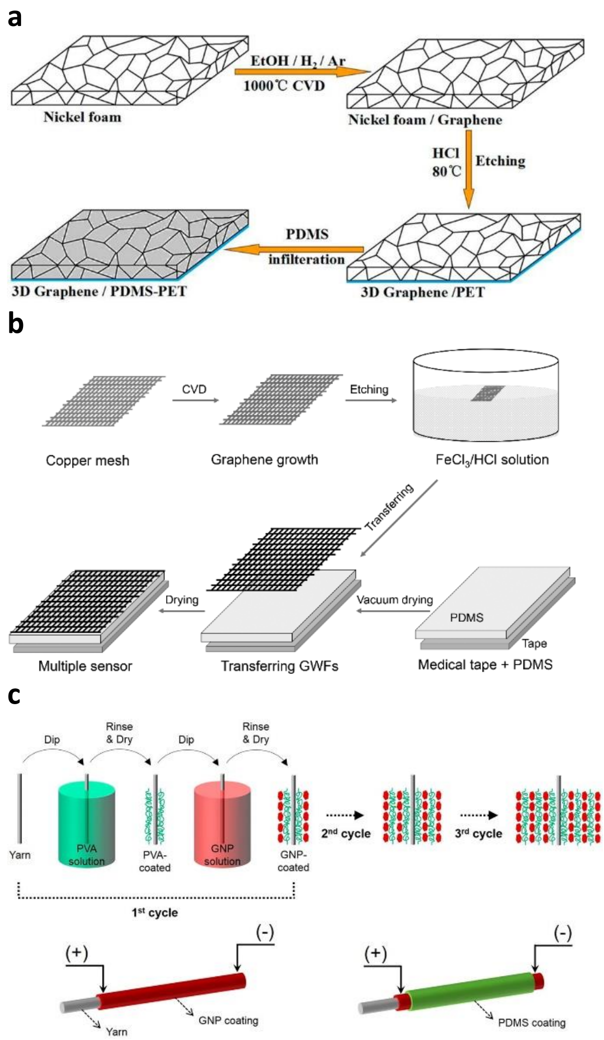

Figure 2.4. Methods utilized for fabricating and processing graphene-based piezoresistive sensors. (a) Graphene-PDMS-poly(ethylene terephthalate) composite fabrication process. The Nickle foam is placed into a furnace and heated to 1000 °C. Ethanol is used as a carbon source by passing it into the furnace. The nickel substrate is then etched by HCl and integrated with PDMS, Reprinted with permission from [130] Copyright 2014, American Chemical Society. (b) Fabrication processes for graphene woven fabric (GWF)-PDMS-tape. GWFs are prepared by growing graphene on copper meshes using CVD. Copper is then etched in a $FeCl_3$/HCl solution and transferred to a pretreated film composite with a medical tape and PDMS, Reproduced with permission. [132] Copyright 2014, WILEY-VCH Verlag GmbH & Co. KGaA, Weinheim. (c) Steps for fabricating graphene using a stretchable yarn. The thickness of the graphene layer can be controlled by the number of poly(vinyl alcohol) and graphene nanoplatelets coating, Reprinted with permission from [134] Copyright 2015, American Chemical Society.

2.5 Integrated sensors with composites for SHM

SHM in composite materials has been implemented by integrating the sensing elements with the composite material either through bounding them on to or embedding them into the material structure. Using the in-situ sensing methods, the performance of composite materials has been evaluated through detecting a wide range of parameters from stress/strain measurement to vibration, temperature, humidity and crack propagation. In the following sub-sections, first, the negative impact of integration of sensors into the material is discussed. Then, applications of three types of sensors explained in the previous sections (piezoelectric-, piezoresistive-, and optical fiber-based sensors) in SHM are exemplified. The applications of these types of sensors are limited to the measurement of temperature and strain in structures. Thus, given the high potential of MEMS for sensing/monitoring a wider range of physical quantities (like humidity, vibration, acceleration, and viscosity), examples of the development and implementation of these sensors into the structures for SHM are also included in this section.

2.5.1 Structural degradation of composites due to embedded sensors

Mechanical degradation due to the poor mechanical properties at the sensor/composite material interface is a common issue in SHM, especially when it comes to the soft and flexible composite structures such as dry woven fabric reinforcements used for forming of doubly-curved parts [138]. In particular, laminar composite materials are extensively suffering from delamination or matrix cracking when it comes to out-of-plane loading conditions [139]. Given the soft nature of unconsolidated textile reinforcement fabrics, the mismatch between mechanical properties of the embedded sensor structure and the fabric is a challenging issue from the perspectives of both sensor measurement and fabric properties. To show this issue, the effect of integrating dummy inclusions into a multi-layered flat-bed weft-knitted fabric (MKF) containing glass fiber (55 vol.%) and polypropylene filaments were compared against the bare fabrics in [329]. In terms of stiffness, the presence of the sensor showed a substantial impact on bending deformation especially on the compressive side of the material. Moreover, inter-laminar fracture toughness was considerably weakened implying vulnerability of shear strength when the sensor is embedded into the composite layers (see Figure 2.5) [140]. Nevertheless, three-point bending tests on the unidirectional glass-epoxy composite with a G-10/FR4 Garolite (a common material used, for instance, in-board circuits) placed at mid-palate has demonstrated the negligible effect on the shear strength [141]. Overall, integration of the sensors with the same chemical and mechanical properties as the monitored material can help to reduce the degradation caused by the embedded sensors.

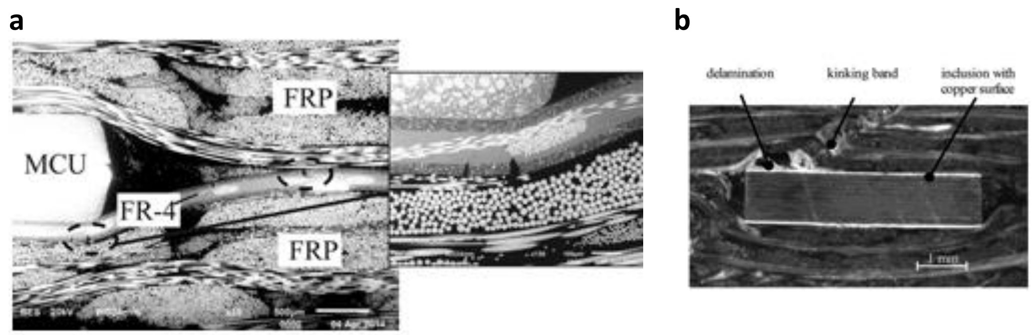

Figure 2.5. Cross-sectional SEM images of the sensors embedded into a composite structure. Integration of sensors led to increased waviness of the fibers in the fabric reinforcement, Reproduced with permission. [140] Copyright 2016, WILEY-VCH Verlag GmbH & Co. KGaA, Weinheim.

The piezoelectric sensors have been used for detection of strain levels at micron levels with a linear behavior (without employing pre-amplification circuits) [142]. Also, by applying thin cyanoacrylate glue and epoxy adhesive layer (<1 µm), mechanical displacements can be well transferred to the transducer. As a result, these types of sensors have been used for the determination of shear strain on the surface of the structure [143]. Integration of PZT fibers in between the flat sheet structures has also been used as a way of health monitoring during manufacturing processes. One proposed approach to implement this integration involves the use of the microvoids and cavities on the metal sheet surface to insert and joint PZT fibers prior to deep drawing a composite into a complex 3D shape [144]. In this work, an array of ten interconnected parallel PZT fibers were fabricated [144] for evaluating piezoelectric function during deep drawing of cup-shape samples (with a double curvature radius of 100 mm and 250 mm). This method was successfully used to permanently detect the local failures in a multiple bolted structure. Despite the fact that embedment itself affects the electrical properties of the piezoelectric materials, it has been reported that impact detection through PZT materials is much better since the superior acoustic coupling with the ambient material [145].

One of the critical issues related to the performance of the piezoelectric-based sensors has been their degradation due to temperature. Previous experiments on the electrical impedance of 5H PZT sensors revealed a frequency-dependent effect of temperature on the amplitude of the impedance [146]. Experimental data revealed that increasing the temperature leads to higher signal amplitudes. This effect was seen to be more significant at low-frequency signals [147]. Based on the aforementioned decays due to temperature, compensatory methods are necessary to be developed in future studies.

2.5.2 Application of piezoresistive composites for SHM of composites

2.5.2.1 Self-sensing piezoresistive structures

Conductive composite materials are widely used either as self-sensing structures or external sensors that are integrated with other materials for sensing their physical properties. One example of self-sensing composites is heterogeneous conductive composites wherein carbon-based fillers (such as short carbon fibers and nano-graphite platelets (xGnP)) were embedded [148] for applications such as traffic monitoring [149] and real-time damage detection in civil structures as shown in Figure 2.6 [89, 150, 151]. Carbon-based fillers have provided a wide range of relatively simple fabrication possibilities. For instance, graphene (as an attractive conductive element in self-sensing composites) has frequently been used to induce electrical conductivity into the ceramic-based composite material. Embedded carbon nanotube sheet layers into the laminated composite structures are another examples that have been used as a versatile tool for detecting tension and compression in the composite materials [152]. Combining graphene with pre-polymers and spark plasma sintering has shown higher conductivity (up to two orders of magnitude) compared to that obtained using carbon nanotube (see Figure 2.7) [153]. Moreover, through the continuous roll-to-roll spray coating process [154-156], dip coating [157], and chemical vapor deposition [158], graphene nanoplatelets and carbon nanotubes have been coated on the fiberglass prepreg laminates [152]. They give information on not only the curing process of the woven laminates but also mechanical strains (e.g. a gauge factor of ~17 has been reported for the graphite nanoplatelet spray-coated fiberglass composite fabric [159]).

Similarly, carbon fiber reinforced composite materials have been proven to be a good example of self-sensing structures [160-163]. The carbon fibers are treated as sensor yarns inside the fabric structure to evaluate mechanical responses not only inside the sensing fibers but also on the adjacent fiber materials joined via methods such as stitching. In this way, a continuous monitoring over the entire fiber-reinforced composites can be achieved by one-step integration of the sensor array into the textile fabrics (examples include the parts used in the wind turbine blades [73, 164]).

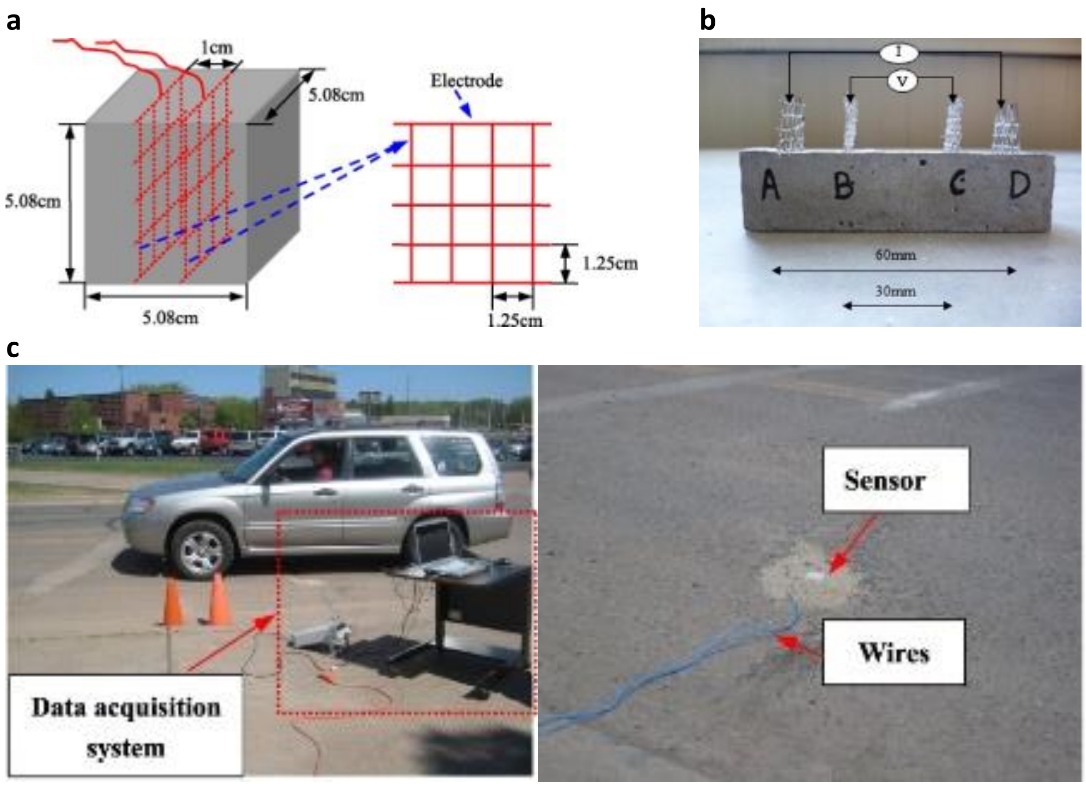

Figure 2.6. Application of self-sensing CNT/cement composites in traffic monitoring. (a) The arrangement of electrodes and design of sensor structure, © IOP Publishing. Reproduced with permission. All rights reserved. Copyright 2009 [149]. (b) Four-point electrical measurement setup in data acquisition, Reproduced with permission. [150] Copyright 2014, Elsevier. (c) Implementation of the sensor for traffic monitoring, © IOP Publishing. Reproduced with permission. All rights reserved. Copyright 2009 [149].

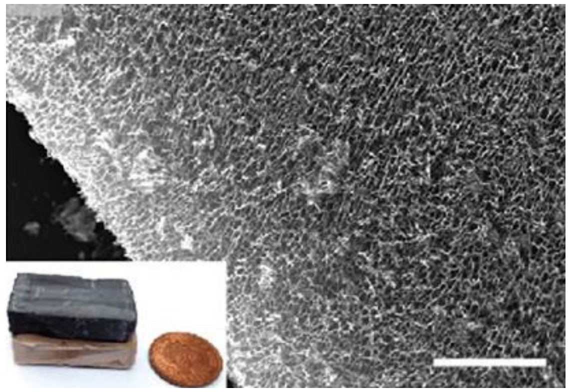

Figure 2.7. SEM image of a self-monitoring ceramic-graphene composite fabricated by combining graphene foams with pre-ceramic polymers and spark plasma sintering. Electrical conductivity was reported to be up to two orders of magnitude higher than typical conductive ceramic composites, Reprinted from [153], Nature Publishing Group.

2.5.2.2 Piezoresistive yarns integrated with materials and structures

Numerous fabrication processes have been suggested to integrate the piezoresistive sensor yarns into composites as seen in Figure 2.8. Detecting curing parameters such as matrix gel point in vacuum infusion forming the process of the glass fiber woven composites is feasible through electrochemical doping of carbon nanotube yarns (Figure 2.8 (a)) [165]. The carbon-based yarn sensors can be easily stitched to the glass fiber laminates with different cross point configurations as shown in Figure 2.8(b, c). Studies on the electromechanical behavior of conductive yarns during manufacturing processes have shown that consolidation of the glass fiber fabrics with carbon fiber in between has relatively low influence on the electrical resistance change of the yarns. However, the same fabrication process resulted in enhanced conductivity of the carbon nanotube coated glass fiber yarns (due to the interphase crack healing effects shown in Figure 2.9) [166]. This implies the significant influence of the chemical and material structure of the yarn and the post-processing steps required for an optimum integration and metallization of the embedded sensors into glass fiber based composites. A wet chemical metallization process can also be implemented to the glass fiber yarns to make them conductive for sensing applications [167]. Another example involves the use of carbon nanotubes grafted on glass fibers through chemical vapor deposition that makes glass fibers electrically conductive [168]. In this approach, the shell thickness, the carbon weight fraction, and accordingly the piezoresistive properties were controlled through the CVD process parameters [169]. It has also been shown that continuous spray coating of SWCNT on the nonconductive fibers (consisted of glass fiber composite) can lead to a gauge factor of 1.25 ± 0.16 [170]. In this method, the temperature and velocity of the coating process play crucial roles in the volume electrical resistance and fiber sensitivity [171]. Graphite nano-platelet thin films are also deposited through a continuous roll-to-roll spray coating process on glass fiber substrate that has been integrated into epoxy/fiber composite structures for life-long structural monitoring (both under mechanical loads and high-temperature manufacturing processes [159]). In-situ polymerization has shown to produce conductive polyaniline composite fibers. By combining this method with aniline, plasma oxygen and then acid doping, polyaniline was coated on the ultrahigh molecular weight polyethylene (UHMWPE). As a result, the piezoresistive behavior was controllable through manipulating the concentration of the reaction mixture [172, 173]. Moreover, a method [174] was developed for metalizing cotton yarns by dipping process in which the cotton yarns were decorated with gold nanoparticles. Then, silver was grown through surface-catalyzed chemical growth. In addition to sensing, metalized fiber yarns can be used to control the heat flow during the cure processes, resulting in high quality manufactured composite parts.

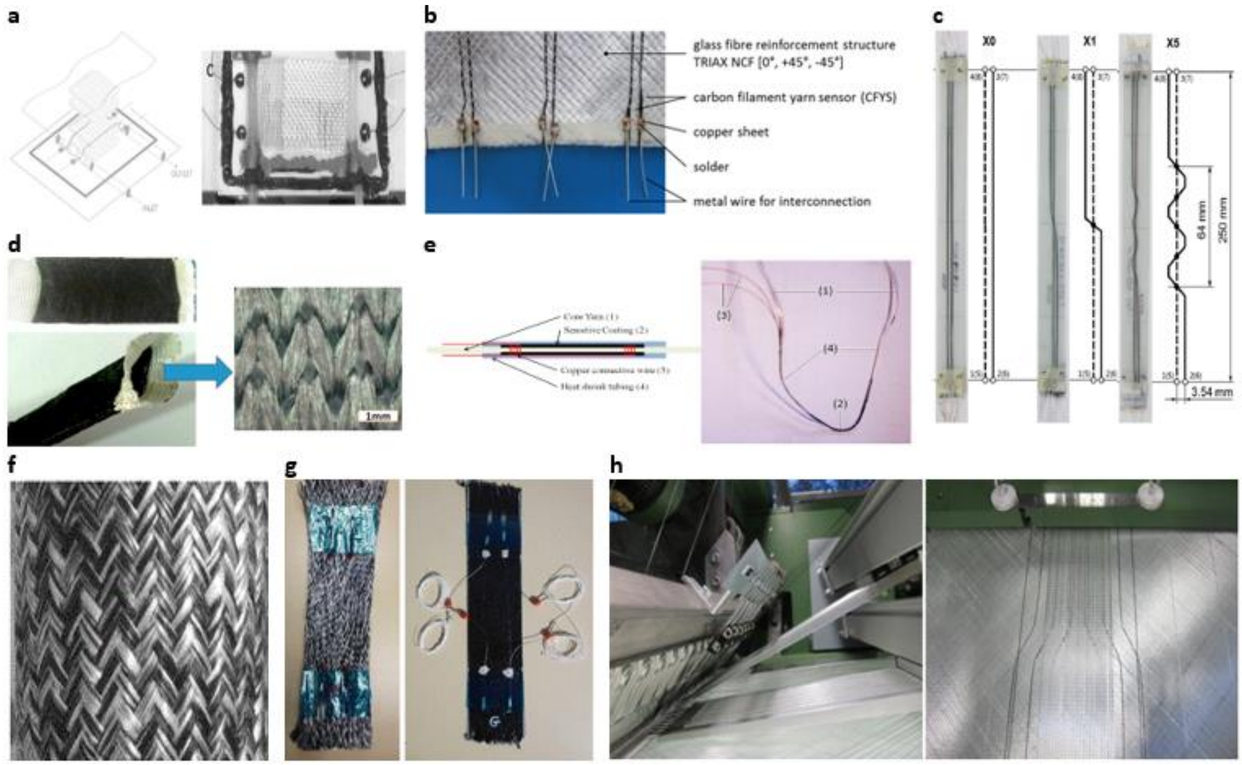

Figure 2.8. Examples of methods used for integrating yarn piezoresistive materials for health monitoring of composites. (a) CNT yarn sensors embedded to monitor flow during vacuum infusion. CNT fibers are placed parallel to the resin flow direction, Reproduced with permission. [165] Copyright 2016, WILEY-VCH Verlag GmbH & Co. KGaA, Weinheim. (b) Representation of the electrical contacts and configuration of the carbon filament yarns embedded into the non-crimp fiberglass fabrics. (c) A cross-point design for embedding the carbon filament yarns in fiber reinforcement plastics, © IOP Publishing. Reproduced with permission. All rights reserved. Copyright 2016 [175] (d) A weft-knitted cylindrical plain fabric with conductive UHMWPE/PANI composite yarns. The electrical resistance of the knitted-fabric sensors increased and then decreased after a critical point with strain, Reproduced with permission. Copyright 2016, Elsevier [123]. (e) Development of yarn sensors based on intrinsically conductive polymers (PEDOT:PSS doped with N-methyl-2-pyrrolidinone, NMP) combined with PVA for woven sensor applications, Reprinted from [176] MDPI Open Access Journals. (f) Braids of hybrid yarns containing PEDOT:PSS polymers. (g) Electrical connections of the sensors embedded into the composite parts before (left) and after (right) consolidation. The sensors are fixed on the fabric using silver paint, Reprinted with permission of Springer. Copyright 2015 [177]. (h) Direct carbon fiber yarn sensor integration into glass fiber non-crimp fabrics in the warp yarn path manipulation (WPM) unit of the knitting machine, © IOP Publishing. Reproduced with permission. All rights reserved. Copyright 2016 [175].

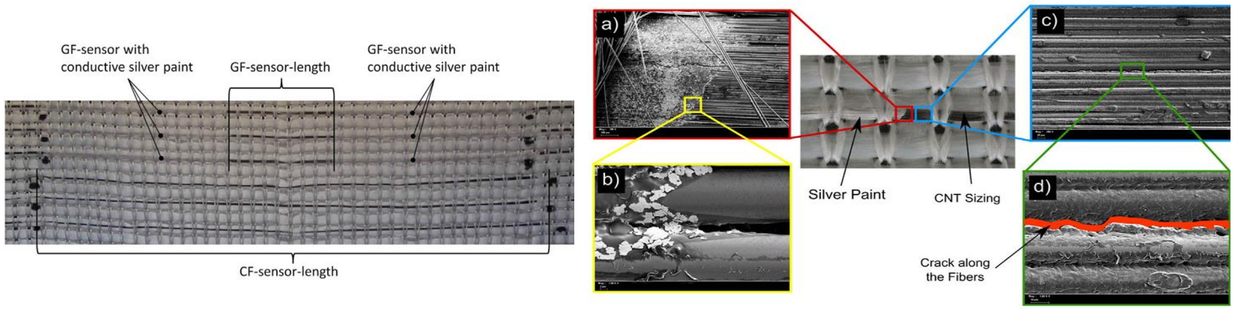

Figure 2.9. Integration of the carbon fiber (CF) sensors and glass fibers (GF) coated by conductive silver paint into the woven reinforcement textile fabrics. No filament failure was observed in both sensor types except the fact that a densification process was accompanied by transverse crack initiation for the silver-coated GF sensors. The adhesion strength difference of the silver-coated GFs and CF yarns is a challenging issue in this sensor configuration, Reproduced with permission [166]. Copyright 2016, WILEY-VCH Verlag GmbH & Co. KGaA, Weinheim.

Since some of the conductive yarns (e.g. carbon fibers) are not stretchable enough for high strains applications, knitting has been done before embedding them into the composite [178, 179]. The knitting pattern and density can determine the stretchability and sensitivity of the sensors: higher linearity and sensitivity has been reported when sensor yarns were knitted with higher densities (Figure 2.8(d)) [123]. Direct integration of carbon fibers in the hybrid PEDOT:PSS can be implemented during knitting process (Figure 2.8(f, g)) or stitching (Figure 2.8(h)) to monitor the deformation through the overall resistance of the structure. Figure 2.9 illustrates example applications of the yarn-like piezoresistive materials embedded into the composites. Integrating conductive carbon fiber yarns into the glass fiber woven fabrics have resulted in fabricating 3D parts during vacuum-assisted consolidation processes with fibers embedded in the structure. This approach has been shown to be applicable for health monitoring of wind turbine blades as shown in Figure 2.10(a) [175, 180]. Combining knitted structures made of spandex with carbon nanotube have also shown to enhance the piezoresistive behavior along the elasticity of the sensor while retaining the sensor performance repeatability [181]. Sensors fabricated by knitted fibers have also been utilized to characterize mechanical properties of woven reinforcement fabrics. Integration of the yarn-like sensors at different regions of a fabric subjected to, for instance, draping process indicated shearing gradient patterns under forming process (Figure 2.10(b)) [182].

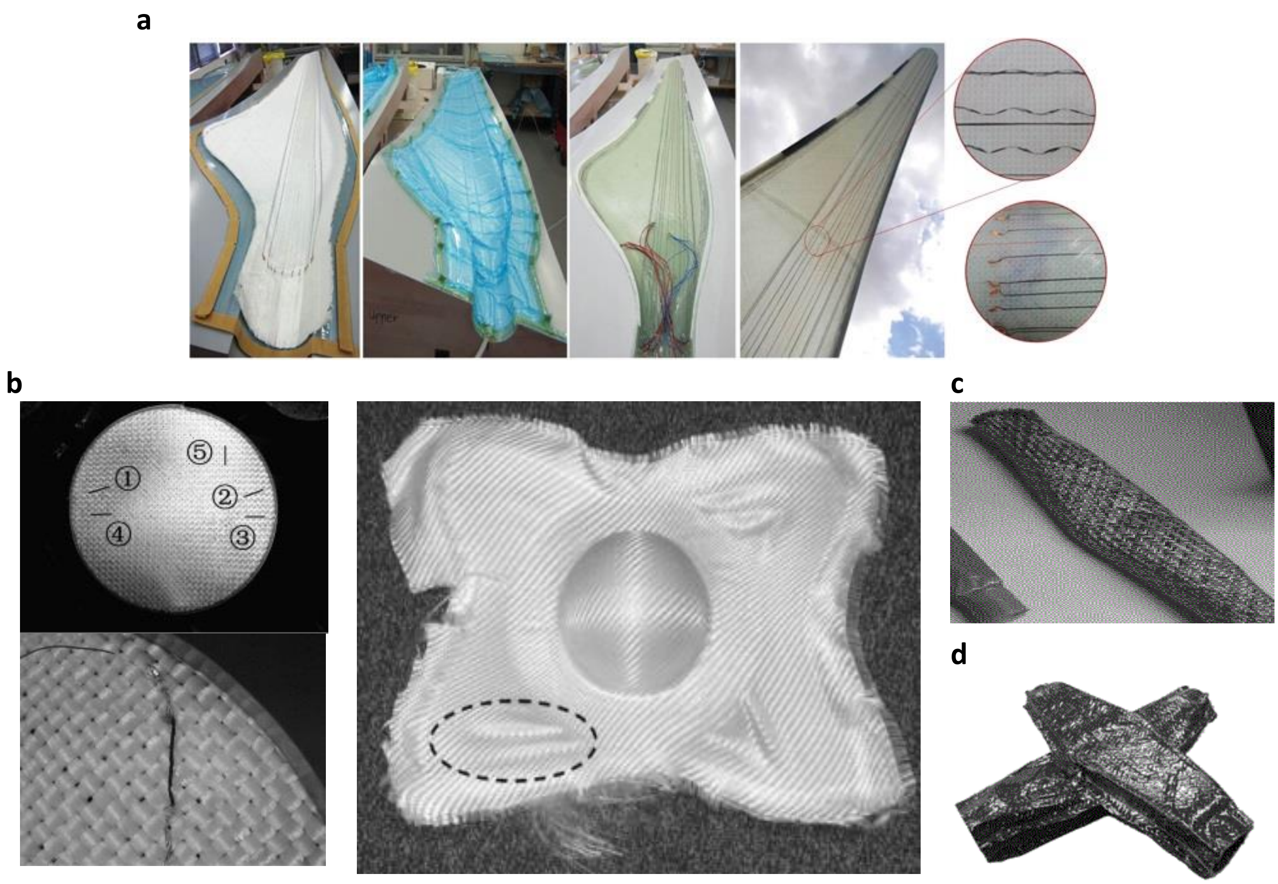

Figure 2.10. SHM application examples by integrating piezoresistive yarns into the woven composite material structures. (a) Integrating textile-based network with wind turbine blades. Fabrics are placed into the blade cast and then vacuumed. Electrical contacts are installed within the blade roots by introducing the crossing points, © IOP Publishing. Reproduced with permission. All rights reserved. Copyright 2016 [175]. (b) Sensors embedded into the woven reinforcement composite fabrics to detect shear angle at a different point in the draping process, Reproduced with permission [182]. Copyright 2011, Elsevier. (c) A 4-layer conductive over braided mandrel and (d) consolidated crossing of stiffeners made from over braided fabrics, Reprinted with permission of Springer. Copyright 2015 [177].

One-dimensional nature of conductive piezoresistive yarns makes them suitable for monitoring the in-situ behavior of composite structures with complex 3D structures such as the cross-shaped body shown in Figure 2.10(c, d) [177]. However, according to the type of health monitoring application (the range of applied strain, load frequency, temperature conditions, etc.), an appropriate configuration of sensors may be essential for reliable electromechanical responses. For instance, previous experiments conducted on yarn sensors made of E-glass/polypropylene commingled through roll-to-roll procedure [183] have shown that utilizing three instead of two roll-to-roll conductive coatings provides higher sensitivity [184]. Weaving the sensor yarns in a warp direction has also resulted in higher sensitivity compared to the woven sensors in weft direction [176, 185]. Furthermore, the piezoresistive yarn orientation and spacing must be taken into account (for instance, a specific yarn orientation of 70° has experimentally shown to possess the highest sensitivity in [186]). Previous studies on textile-based strain sensors also suggest that the more compact the woven structure, the more linear the sensor response. However, the compactness decays accuracy and sensitivity of the sensor during the relaxation period and due to the higher contact area, respectively [187].

Chapter 3: Analytical analysis of imperfection effects in conventional picture frame test

3.1 Overview

Picture frame test (PFT) setup is frequently employed in the literature for characterizing the shear behavior of woven fabrics. Albeit it is believed to provide a fundamental understanding of the fabric shear response in large deformation, there have been frequent reports on the high potential of imperfections during this test mode, especially regarding the induced unintentional axial forces along the yarns. In this chapter, the main sources of such imperfections arising from the operator error during sample installation, to the fixture misalignment, as well as the inherent non-uniformities within the fabric are analyzed, using the kinematic and continuum-based approaches.

3.2 Analytical approaches for analysis of imperfection effects

In the present study, to understand the consequence of the imperfections in the PFT, first, the main sources of imperfections were categorized and the corresponding deformation mechanisms were explored using an analytical framework. In order to mimic a realistic sample boundary condition, clamping edges were defined based on the associated imperfection parameters. The four internal points specifying the joints of the central fabric region (when there are corner cut-offs in the sample) were obtained by intersecting the lines passing through the corresponding opposite clamp edges. Then, those four internal points were modified to adjust the shear angle at the center based on shear angle mismatch imperfection and thereby the state of fabric at each specific shear angle could be determined.

Given the known deformation of boundaries for each region (i.e. central region and fabric arms), two approaches were employed to identify the local strains and local shear angles at every single frame shear angle as shown in Figure 3.1:

(i) *Kinematic analysis*: the length of each fiber in a picture frame test containing imperfection (L') was analytically found from the kinematics of the frame in terms of frame shear angle in order to calculate the induced strain (i.e. the strain is assumed to be uniform over the yarn in this approach).

(ii) *Continuum mechanics based analysis*: having the known initial and instantaneous states of each region in the fabric, local strains were obtained through the displacement field by mapping the initial state to the instantaneous deformed fabric.

It should be noted that in both approaches, the ideal picture frame was considered as the initial state for strain calculation, in order to take into account the strain caused by mounting the fabric onto the fixture. A Matlab code was developed to implement the above approaches for imposing the individual and simultaneous imperfection modes, and finally to obtain the resulting shear angle and local strain gradients.

In the continuum approach, the local strain along the fibers was calculated according to the displacement field corresponding to the mapping obtained by the imposed deformation mechanism ($\boldsymbol{p} = \chi(\boldsymbol{P})$). Then, the deformation gradient $\boldsymbol{F}$ matrix was assembled for every element according to Eq. (3.1) [188-191]:

$$[\boldsymbol{F}] = \left[\frac{\partial x_i}{\partial X_j}\right] \tag{3.1}$$

(i,j=1,2) where x_i is displacement fiend and X_j is the coordinates in the non-deformed system located on the diagonals of the frame. The deformation gradient $\boldsymbol{F}$ was then rotated by 45° to calculate the strain components along the yarns (X'_j) (See Figure 3.1). The Cauchy-Green tensor $\boldsymbol{C}$ was obtained as following:

$$[\boldsymbol{C}] = [\boldsymbol{F}]^T[\boldsymbol{F}] \tag{3.2}$$

And finally, the Green-Lagrange strain tensor $\boldsymbol{E}$ was calculated through Eq. (3.3) from which the strain along the fibers were taken (e_{11}, e_{22}):

$$[\boldsymbol{E}] = \frac{1}{2}([\boldsymbol{C}] - [\boldsymbol{I}]) \tag{3.3}$$

Remark: Either of the two approaches may be applied for characterization/test design purposes, depending on the type/deformation behavior of the fabric of interest. In essence, as opposed to kinematic analysis, the continuum based analysis neglects the existence of the gaps and their disappearance with shearing and also sliding the fibers through the cross-overs. Accordingly, for fabrics in which deformation mechanism is mainly dominated by individual yarns with minimal interactions between them (e.g. similar to a non-crimp fabric/NCF), kinematically driven yarn strains would adequately describe the mechanical response of the material. On the other hand, for fabrics with more (semi) continuous mechanical behavior (i.e. denser fabrics with high friction at crossovers— such as prepreg fabrics), the continuum approach would be realistic and close to the known Pin Joint Network (PJN) [192] but with extendable/compressible yarns. It is also worth noting that at high shear angles, the gaps within a given fabric vanish and its behavior would tend toward a fully continuous material.

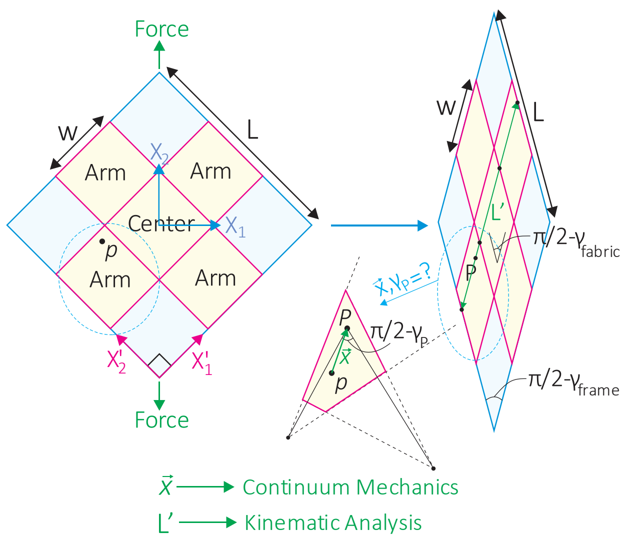

Figure 3.1. Illustration of the two approaches taken for analysis of deformation field within the fabric. A continuum mechanics based approach introduces local strains with respect to the local displacements obtained by the deformation mapping of the regions in the ideal picture frame test to the after shear (deformed) state while considering imperfection. The kinematic analysis, on the other hand, directly uses the instantaneous length of the fibers constrained to the picture frame system (L') in the presence of imperfection.

3.3 An insight into the imperfection sources

The main emphasis of the past studies of enhancing the characterization of woven fabrics has been on the effect of misaligned fibers as a primary source of imperfection in the picture frame setup [190, 193, 194]. In addition, fiber bending close to the fixture arms has been also well recognized. However, for generalizing the sources of imperfections into three main categories from a deformation standpoint, here we propose three uncertainty sources: (i) operator related flaws, which predominantly includes fiber misplacement or misoriented mounting of the fabric from the onset of testing, (ii) fixture related flaws, the main one of which may be the lack of ideal coincidence of sample edge regions with the shear frame central (pin-to-pin) lines; this type of imperfection may be due to the faults in the fixture design itself and/or excessive clamping forces on the fabric which will constrain the free rotation of fibers during shearing, often resulting in the reported yarns bending close to the arms during the test [41]. (iii) Fabric (material) related flaws, arising from the micro/meso-level mechanisms (e.g. lack of sufficient fiber/fiber friction under rotating condition at crossovers, the effect of fabric cut-offs/free yarn ends on intra-yarn shear [15], or non-uniform fiber orientation in the as-received fabric, etc.). The latter category of flaw during the test can yield the partial transformation of shearing from the fixture frame to the fabric's center and also lead to the shear angle non-uniformity over the sample. Considering a picture frame fixture with an effective length L, Figure 3.2 illustrates the abovementioned imperfection parameters and their corresponding eventuated deformation mechanism (from where the strain components are calculated). In the following sections, the consequences of each imperfection source in the conventional picture frame test are discussed from a continuum based and kinematic based point of view.

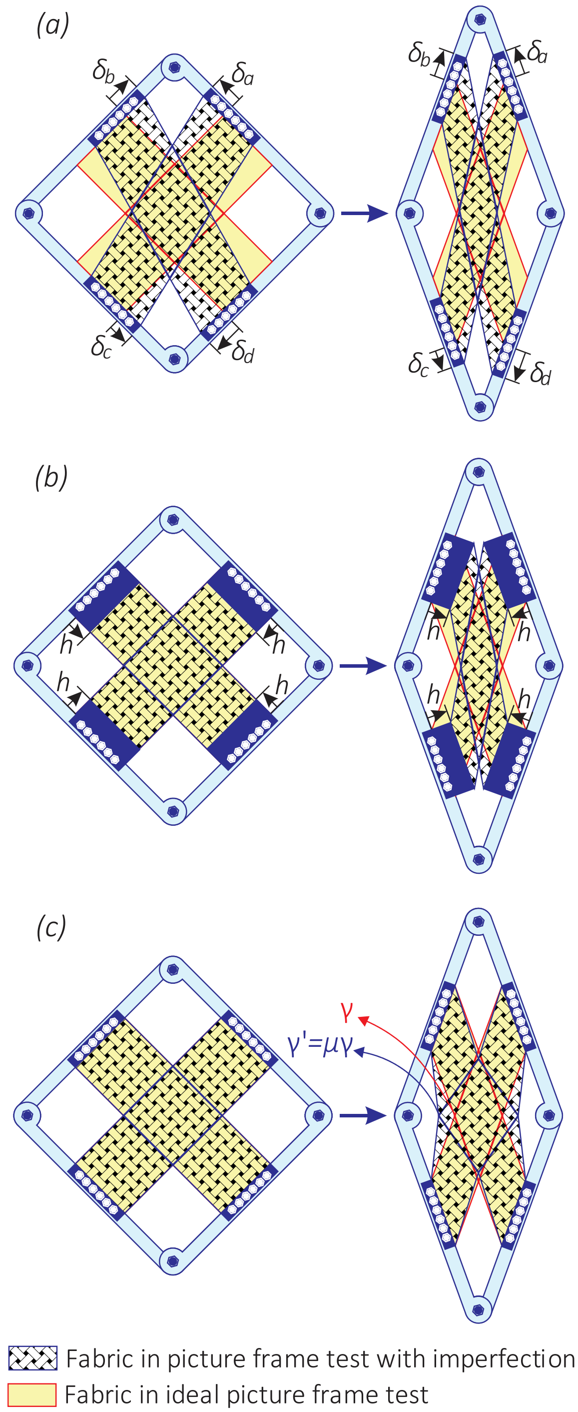

Figure 3.2. Schematic illustration of the imperfection parameters in the conventional picture frame setup and their associated deformation mechanisms at the onset of the test (left figures, γ=0°) and after applying the shear load (right figures, γ°). (a) Fabric misplacement, (b) offset of the clamping edge with the ideal shear frame, (c) mismatch between the frame and fabric shear angle.

3.4 Imperfection Case 1: Oriented fabric misplacement into the test fixture frame

Fabric misalignment is the most recognized and the major imperfection source in the picture frame test. It has been generally characterized by the angular (rigid body) rotation of the orthogonal fabric with respect to the frame arms [190, 193, 195]. Highly sensitive tension/compression is believed to be introduced into the yarns due to the presence of such fiber misalignment with respect to the frame. This state can induce yarn tension in one direction and yarn compression in another direction during the test. More generally, the yarn misalignment can practically arise from the distinct misplacement of four edges of the sample during installment (Figure 3.2(a)). Kinematic analysis of a frame comprising misaligned fabric in this general case gives the shear angle at the central region as a function of frame shear angle in the form of:

$$\begin{aligned}\gamma_{center} = \gamma_{frame} &+ \tan^{-1}\left(\frac{\left(\frac{\delta_a}{L}+\frac{\delta_c}{L}\right)\cos\gamma_{frame}}{1+\left(\frac{\delta_a}{L}+\frac{\delta_c}{L}\right)\sin\gamma_{frame}}\right)\\ &+ \tan^{-1}\left(\frac{\left(\frac{\delta_b}{L}+\frac{\delta_d}{L}\right)\cos\gamma_{frame}}{1+\left(\frac{\delta_b}{L}+\frac{\delta_d}{L}\right)\sin\gamma_{frame}}\right)\end{aligned} \tag{3.4}$$

Moreover, the kinematic yarn strain in directions X_1' and X_2' (Figure 3.1) can be given by Eqs. (3.5) and (3.6), respectively:

$$\varepsilon_{X_1'} = \sqrt{1+\left(\frac{\delta_a}{L}+\frac{\delta_c}{L}\right)^2 + 2\sin\gamma_{frame}\left(\frac{\delta_a}{L}+\frac{\delta_c}{L}\right)} - 1 \tag{3.5}$$

$$\varepsilon_{X_2'} = \sqrt{1+\left(\frac{\delta_b}{L}+\frac{\delta_d}{L}\right)^2 + 2\sin\gamma_{frame}\left(\frac{\delta_b}{L}+\frac{\delta_d}{L}\right)} - 1 \tag{3.6}$$

To better understand the effect of this flaw mode, let us now consider two special cases: (a) pre-rotated fabric misplacement; i.e. when $\delta_a = -\delta_b = \delta_c = -\delta_d$, and (b) the pre-sheared fabric misplacement; i.e. when $\delta_a = \delta_b = \delta_c = \delta_d$.

3.4.1 Pre-rotated fabric misplacement

The results of the kinematic and continuum based analysis as represented in Figure 3.3 for the pre-rotated fabric misplacement suggests no significant shear angle mismatch between the frame and central region. Instead, each of the fabric arms can undergo either more or less shear. Theoretically, the shear angle at the center falls between the maximum and minimum shear angle range. The magnitude of the shear angle difference between fabric and frame increases at early shearing, reaching to a maximum followed by a decrease during the test (Figure 3.3(a)). The peak shear angle discrepancy depends on the sample cut-off size as the bigger sample sizes cause the peak to occur later and also the fabric undergoes more shear angle gradient. Kinematic yarn strain analysis suggests introducing a slight yarn tension at the onset of the test due to the mounting misplacement itself but it is negligible compared to the strain magnitude induced due to the shearing. A pre-rotated fabric misplacement causes this minor tension to exacerbate in the yarns in direction X_1' while it adds compressive strains to the yarns in the opposite direction (direction X_2') as can be seen in (Figure 3.3(b)). Continuum based strain analysis (Figure 3.3(c, d)), however, clearly suggests a strain variation along the yarns in ideal PJN fabrics, with tension on one end and compression on the other end of the yarns. This implies potential of yarn pull out along the crossovers in the absence of sufficient frictional forces. Theoretically, the stain at central region maintains at the maximum compressive strain in both directions.

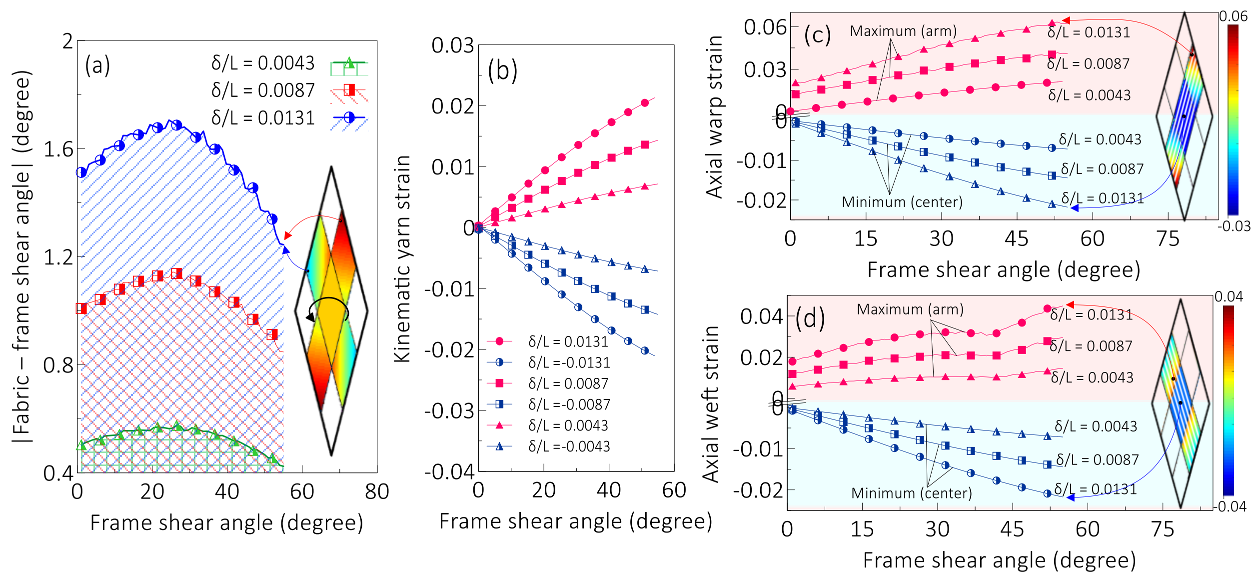

Figure 3.3. The effects of pre-rotated fabric misplacement as a case of imperfection on shear angle distribution and strain along the yarns. (a) the absolute difference between the frame shear angle and maximum/minimum local shear angles using the continuum approach; (b) variation of kinematic yarn strain with frame shear angle using the kinematic model; (c, d) variation of the maximum and minimum local continuum strains along the warp and weft yarns in directions X_1' and X_2', respectively, using the continuum model. Note that both the kinematic and continuum-based strains suggest tensile/compressive strains with high sensitivity to the misplacement parameter $\frac{\delta}{L}$.

3.4.2 Pre-sheared fabric misplacement: operator error

The mechanical effects of pre-sheared fabric misalignment in the picture frame test are illustrated in Figure 3.4. for both positive pre-sheared ($\delta_a = \delta_b = \delta_c = \delta_d > 0$) as well as negative pre-sheared ($\delta_a = \delta_b = \delta_c = \delta_d < 0$) imperfection cases. In the former case, the deformation mechanism implies faster shearing in the central area of the sample compared to the frame, while the latter case is accompanied by faster shearing (and hence possibility of fiber locking) of the sample around the clamp regions. Though, in both cases, the shear angle discrepancies are maximum at the commensurate of loading, and tend to more uniform shear distribution as the frame is further loaded (Figure 3.4(a)). This is actually in accordance with the previous experimental observations where the shear angle difference between the fabric and frame decreased with increasing the shear angle, for some cases pre-shear specimens [196]. Moreover, per Figure 3.4(a), sample size and corner cut-offs do not affect the shearing patterns over the fabric. The analytical yarn strain formulations given in the Eqs. (3.5), (3.6) can be applied to the pre-rotated fabric misalignment, except that in this case the yarns in both directions undergo the same yarn strain sign (i.e. in case of positive pre-sheared misalignment they withstand growing tension, and compression when negatively pre-sheared).

The above imperfection analysis for the fabrics with continuum-like behavior shows a non-uniform tension/compression state in the fabric depending on the state of initial pre-shearing. It is worth mentioning that increasing the sample size (w) leads to regions with higher tension/compression continuum strains, however, the strain in the central region is not affected by the sample size. Also, in the center point of the sample, both strain calculation methods give identical values for all imperfection cases.

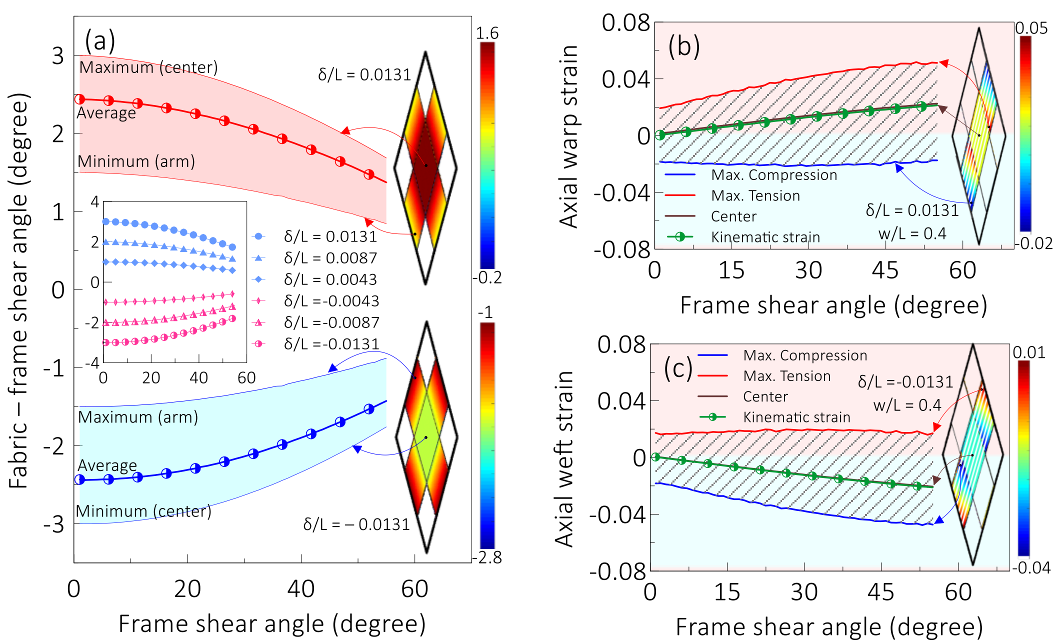

Figure 3.4. The mechanical effects of pre-sheared fabric misplacement imperfection case. (a) variation of the difference between fabric and frame shear angle with frame shear angle using the continuum model, for the case of positive pre-shearing $\left(\frac{\delta}{L} = 0.0131\right)$ and negative pre-shearing $\left(\frac{\delta}{L} = -0.0131\right)$ corresponding to the pre-shear angle of 3 degrees; (b, c) comparison of kinematic-based and continuum strains along the yarns for the positive and negative pre-shearing imperfection cases, respectively. The three $\frac{\delta}{L}$ levels considered here correspond to an initial miss-rotation (mounting error) angle of 1°, 2° and 3°, respectively.

3.5 Imperfection Case 1I: Incoincidence of the clamping edge and ideal shear frame

When the sample clamping edges deviate from the shear frame central lines, a non-uniform shear angle gradient, and thereby yarn tension/compression, is developed over the fabric. This imperfection case basically imitates either the faults in the fixture design itself [197] and/or the bending close to the jaws due to the excessive clamped forces (which cannot allow the fiber to rotate freely under the clamp). Besides, in the studies where simultaneous shear and tension were studied [37, 198-200], an initial yarn tension prior to applying the shear load introduced the same imperfection to the test. The deformation mechanism associated with this type of imperfection in terms of the induced strain into the yarns and shear angle distribution is represented in Figure 3.5. The shear angle gradient (Figure 3.5(a, b)) suggests that an inward offset ($\frac{\mathrm{h}}{\mathrm{L}} > 0$) causes the central region to undergo higher shear angle than the frame. This can explain the previous experimental observations where yarn bending close to the arms led to the higher shear angle in the central region [43]. Likewise, the shear angle at center falls behind the frame shear angle when clamping outside the ideal shear frame ($\frac{\mathrm{h}}{\mathrm{L}} > 0$). In either case, the shear angle discrepancies in this type of imperfection increase with frame shear angle.

A kinematic analysis of the deformation gives the shear angle at the central region as a function of frame shear angle (γ_{frame}) and the gripper offset ($\frac{h}{L}$) as:

$$\gamma_{center} = \gamma_{frame} + 2\tan^{-1}\left(\frac{\frac{h}{L}\sin\gamma_{frame}}{\frac{1}{2} - \frac{h}{L}\cos\gamma_{frame}}\right) \quad (3.7)$$

A continuum strain analysis suggests that the initially applied compression or tension due to this imperfection is locally evolved as shear loading is applied. Namely, the inward clamp edge offset induces extreme continuum compressive strains over the corners of the arms (e.g. 5.48% increase in maximum compressive strain for ($\frac{w}{L} = 0.8$ and $\frac{h}{L} = 0.015$), and tension in the central region. This, in turn, augments the possibility of wrinkling at the corners of the arms as it has been frequently observed in the wrinkling patterns reported before [43, 45, 47, 48]. The outward gripper edge offset affects the fabric deformation during the test inversely (i.e. it leads to compressive strains in central region and tension around the arms' corners). A strain gradient along the yarns in both cases also implies a high possibility towards fiber slippage.

The kinematic analysis of this imperfection case results in a uniform yarn strain distribution over the fabric which can be expressed by Eq. (3.8):

$$\varepsilon_{yarn} = \left(-2\frac{h}{L}\right) + \left(\sqrt{1 + 8\frac{h}{L}\left(\frac{\sin\frac{\gamma_{frame}}{2}}{1 - 2\frac{h}{L}}\right)^2} - 1\right) \tag{3.8}$$

where the right term represents the strain due to the frame shearing and the left term is the induced initial yarn strain due to the imperfection itself. In this equation, $\frac{h}{L} > 0$ and $\frac{h}{L} < 0$ represent inward and outward offsets, respectively as shown in Figure 3.2(b). As opposed to the continuum analysis, using the kinematic model the initial tension/compression induced strain is relaxed (Figure 3.5(c)) during the test (i.e. shearing adds more tension to the compressed state of yarn for inward gripper edge offset and vice versa for the outward offset case). The decreasing trend obtained from the above equation is well aligned with the previous experimental observations where a coupled tension-shear was applied to the fabric and a decreasing axial load was recorded with shearing the frame [201]. It implies that set-up modifications are necessary for those setups studying the mechanical characterization of fabrics under coupled loading; for instance, a roller based clamping which can move with the shear frame may be used for applying the biaxial loads during shearing. Alternatively, such coupling between the pre-tension and shearing can be accounted for during the global to local transformation of normalized forces [202].

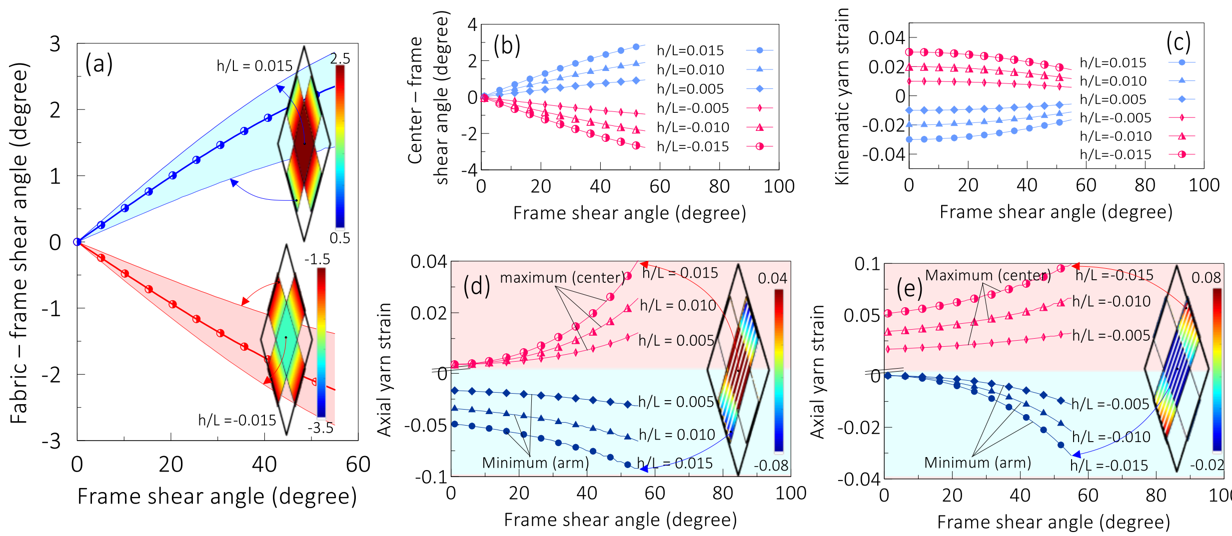

Figure 3.5. The shear angle gradient and axial yarn strain distribution as a result of offset of clamping edge and the shear frame central lines. (a, b) The difference between fabric and frame shear angle versus frame shear angle for different *h/L* values, under continuum based and kinematic analyses, respectively; (c) variation of kinematic strain along the yarns with the frame shear angle; (d, e) changes in the continuum strain for inward and outward offset cases, respectively.

3.6 Imperfection Case III: Frame/fabric shear angle mismatch

The fabrics in the conventional picture frame test are intrinsically susceptible to non-uniform shear distribution (thereby yarn tension/compression) owing to micro/meso-level uncertainty factors such as varying crimp angle, or non-uniform frictional forces at crossovers (at different regions of samples due to cut-offs), local misalignment of fibers etc. This can cause (even in absence of external imperfection) a shear angle gradient over the fabric, and hence a deviation from the frame shear angle.-This effect is believed to be very sensitive to the sample size. For instance, it has been reported that in large-cross samples, the yarn bending close to the jaws is dominant [43] and therefore the shear rate at the center region is faster than the frame ($\mu>1$ where μ is the fabric/frame shear angle mismatch factor as shown in Figure 3.2(c)). In opposite, in the case of small-cross sizes, the different shear rigidity of the center and arms has inhibited full translation of the frame shearing to the central region and hence $\mu<1$ [43]. *This is, in fact, a primary disadvantage of having corner cut-offs when preparing the test sample in the conventional picture frame tests.*

In order to simulate the effects of this imperfection case, the data obtained by DIC measurements in the previous works [33, 196] for TWINTEX fabric were used to define a fabric/frame mismatch factor (μ) as a function of frame shear angle.

An analytical (kinematic-based) relationship in this deformation mechanism can be given for the maximum (when μ<1) or minimum (when μ>1) shear angle (occurring at the corner of the fabric arms, see Figure 3.6(a, b)I) as:

$$\gamma_{ext.,arm} = \tan^{-1}\left(\frac{1-\frac{w}{L}}{\cos\gamma_{frame} - \frac{w}{L}\left(\cos\left(\frac{\gamma_{frame}}{2}(\mu+1)\right) + \sin\left(\frac{\gamma_{frame}}{2}(\mu-1)\right)\right)} + \cot\left(\frac{\pi}{4} - \frac{\gamma_{frame}}{2}\right)\right) \tag{3.9}$$

Under the continuum approach, this effect inherently should induce no axial strain in the central region; however, the arm regions are expected to undergo a type of strain distribution that makes fiber slippage likely similar to that seen in the case of other two aforementioned imperfection types. Figure 3.6 demonstrates the shear angle and strain gradient calculated through both kinematic and continuum strain analyses. In terms of local shearing, in both models, when the shearing at the center falls behind the frame shear angle, the arms make compensate through undergoing higher shear angles, and vice versa. Considering the kinematically calculated yarn strains, a minor tension (with the mismatch factor range of 0.87-1.10 extracted from the literature [33, 196]) develops as a result of this imperfection (Figure 3.6(a)II, (b)II). For the fabrics with more intense mismatch factors, the tensile kinematic strain significantly increases no matter μ>1 or μ<1. A relationship can be derived from the kinematic analysis of the tensile strain induced at the mid yarn (which bears the maximum strain) in form of Eq. (3.10):

$$\varepsilon_{yarn_{max}} = \sqrt{\left(1-\frac{w}{L}\right)^2 + 4\frac{w}{L}\sin^2\left(\frac{\gamma_{frame}}{2}(\mu-1)\right)} - \left(1-\frac{w}{L}\right) \tag{3.10}$$

From the above equation, one can find that the strain induced in the yarns due to the shear angle mismatch remains always tensile and its magnitude depends on both shear angle mismatch factor as well as the sample width as shown in Figure 3.6(c, d). At a constant mismatch factor, increasing the sample width causes higher yarn tension during shearing.

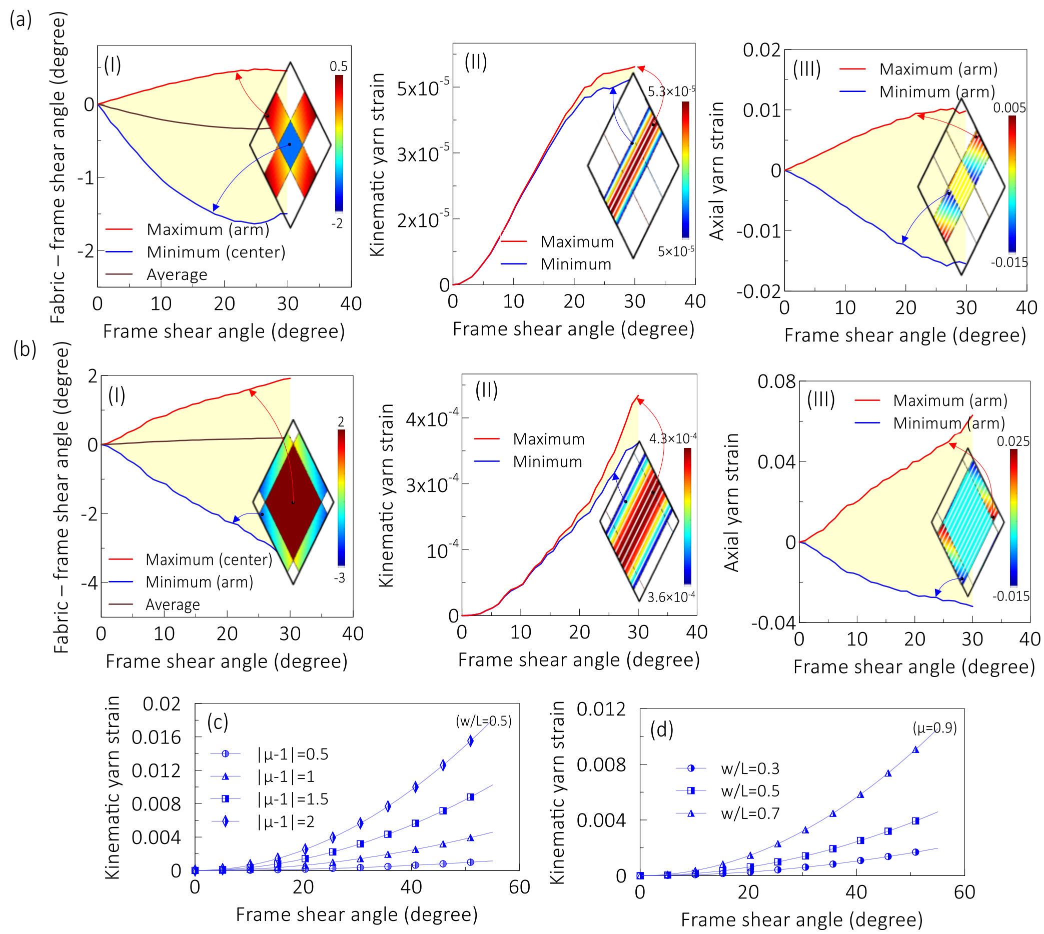

Figure 3.6. Effect of fabric-frame shear angle mismatch on the mechanical behavior of fabrics. Variation of I: difference between fabric and frame shear angle, II: kinematic yarn strain and III: continuum strain with frame shear angle for (a) small sample width (*w/L* = 0.29) wherein the fabric shear angle at center falls behind the frame shear angle and (b) large sample width (*w/L*=0.72) with higher fabric center shear angle than frame. The shear angle dependent mismatch factors were taken from reference [33] and [196], respectively. Variation of kinematic yarn strain for different constant mismatch factors (c) as well as different sample sizes (d) is also shown as a function of shear angle. From comparison of a(I) and b(I) and also from (d) it is evident that the sample size/shape is highly effective under this imperfection mode and can dominantly change the characterization results.

3.7 Summary of findings

In this chapter, the main sources of imperfections in the picture frame testing were studied and modeled, showing how they can lead to the notably adverse effects in the pure shear characterization results. The associated imperfect deformation mechanisms were imposed as boundary conditions and two analytical approaches were undertaken to reveal their consequences in terms of the induced non-shearing strains along the yarns of the fabric. It was discussed that even small amount of imperfections may induce a considerable amount of energy into the yarns by axially stretching them, or it may cause local compressive strains that can expedite the formation of out-of-plane wrinkling defect in the fabric. Based on the literature, and also our experience in this research, the imperfection types were classified as (i) pre-shearing/pre-rotation of the fabric, (ii) fixture design error which can cause an offset during installation of the fabric into the grippers, and (iii) shear angle mismatch between the center of the fabric sample and the frame due to non-uniformities inside the material and/or imposed boundary conditions.

As opposed to what assumed in the literature, fabric misplacement does not seem to essentially affect the deformed areas of the fabric in a similar manner at all of the four clamping areas of the PFT. Defining four distinct misplacement parameters, one can find that either a compressive or a tensile yarn strain can develop over different arm regions, which could well explain the premature arm-induced wrinkles observed in several past experimental studies (while the wrinkling in an ideal shear PFT is expected to form in the central region due to fiber locking at high shear angles).

The results also confirmed that any shear angle gradient or mismatch between the fabric and frame (e.g. due to severe clamping pressures and local yarn bending close to the grippers) can cause notable tensile loads in the yarns. Hence, outmost care should be taken when interpreting the picture frame test results as the current version of this test is highly sensitive to contributions from the non-ideal, axial yarn strains.

Chapter 4: Frameless picture frame test setup: An enhanced approach for mitigating the imperfection effects

4.1 Overview

Upon a systematic understanding of different types of potential imperfections in the current picture frame tests (Chapter 3), a new shear test methodology is proposed in this Chapter, and to be also verified using embedded sensors in next chapter. In the new set-up, the shearing frame boundary condition is inscribed on the fabric sample itself during sample preparation; in lieu of fabricating and installing a metallic picture frame. This so called ‘frameless picture frame’ (FPF) test will be shown to effectively mitigate the previous imperfections and provide a better control and uniformity of the fabric installation and deformation during the test. Contrary to the conventional PFT, the wrinkling behavior and normalized force response in the FPF are expected to be in agreement with the conventional bias extension tests, with no close-to-arm fiber bending, while showing a superior test repeatability at both loading and unloading stages.

4.2 Standard shear characterization procedure (without sensor embedment)

The shear deformation was applied to assess the fabric’s mechanical respond under the suggested picture frame setups. Comingled polypropylene (PP)/glass fibers (TWINTEX® TPP60N22P-as supplied by AS Composites Inc. (Quebec, Canada) with a nominal fiber diameter of 18.5 µm, the thickness of 1.0-1.5 mm and fiber width of 4.3 mm). A tensile displacement exerted on the one corner of the frame (Figure 4.1(IV)) using a mechanical testing instrument (Instron 5960, USA). All tests were conducted with a cross-head speed of 20 mm/min, while a 50 kN load cell was used to capture force-displacement data. The load/unload was repeated for 3 times at 3 replications for each sample to evaluate repeatability as well as the cyclic behavior of the material using different sample sizes. Since the main purpose of this study was to mitigate the test imperfection effects, different sources of uncertainties/flaws during shear characterization of fibers were considered during analysis.

(i) Operator related flaws

(ii) Fixture related flaws

(iii) Fabric related flaws

Additionally, bias extension tests/BET (with 75×150 mm sample size) were carried out in order to compare with the picture frame data. The data were normalized based on Refs. [22, 203] as described below.

4.2.1 Normalization of the PFT

For the tests based on picture frame configuration, the normalized force-frame shear angle curves were calculated from the force-displacement data according to the energy dissipated in the central (effective) region of the fabric. The angle of the frame (θ) was correlated to the cross-head displacement (δ) by Eq. (4.1) [22]:

$$\theta = \cos^{-1}\left(\frac{\sqrt{2}L + \delta}{2L}\right) \tag{4.1}$$

where L is the frame length. Therefore, frame shear angle was obtained by Eq. (4.2):

$$\gamma_{frame} = 90^{\circ} - 2\cos^{-1}\left(\frac{\sqrt{2}L + \delta}{2L}\right) \tag{4.2}$$

The normalized force ($F_{normalized}$) then, for a picture frame with corner cut-offs was calculated by [22]:

$$F_{normalized} = \frac{F - F'}{2\cos\theta}\left(\frac{L}{w^2}\right) \tag{4.3}$$

where F is the recorded force, F' is the fixture force without mounting a sample and w is the sample width (see Figure 3.1).

4.2.2 Normalization of the BET

In order to normalize the force-displacement data associated with the BET, the shear angle at the fabric's central region was determined by:

$$\gamma_{frame} = 90° - 2\cos^{-1}\left(\frac{h - w + \delta}{\sqrt{2}(h - w)}\right) \tag{4.4}$$

Based on the energy dissipated in the central region, the normalized force can be found in the implicit form of [22, 192]:

$$\begin{aligned} F_{normalized} = \frac{1}{(2h - 3w)\cos\gamma_{frame}} \Bigg(\left(\frac{h}{w} - 1\right).F.\left(\cos\frac{\gamma_{frame}}{2} - \sin\frac{\gamma_{frame}}{2}\right) \\ - w.\cos\frac{\gamma_{frame}}{2}.F_{normalized}\left(\frac{\gamma_{frame}}{2}\right)\Bigg) \end{aligned} \tag{4.5}$$

4.3 Conventional picture frame shearing test set-up with embedded sensor

Conventional picture frame test has been extensively employed for shear characterization of woven fabrics. The steps for preparing and mounting the fabric in this approach is illustrated in Figure 4.1. Fabrics with fixture length of L= 24.5 cm and sample sizes of w= 15, 11, and 7 cm were cut. Then two sides of needle clamps were inserted into the fabric. The clamps were subsequently mounted into the picture frame fixture where a shearing load was transferred to the fabric through the axial displacement of the fixture joint. A sensor was also attached to explore the local displacement between two ends of the mid yarn.

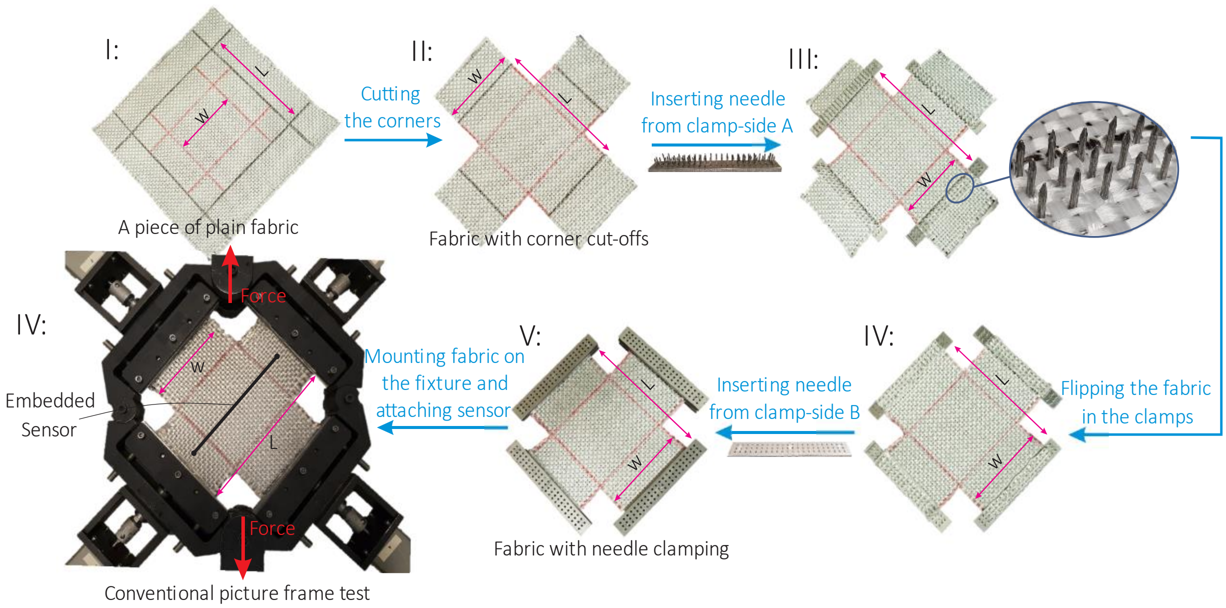

Figure 4.1. Sample preparation process in the conventional picture frame testing procedure. A fabric with corner cut-offs is clamped and mounted to the fixture.

4.4 A new frameless shearing test set-up with embedded sensor

The frameless picture frame (FPF) test process was designed with the sequences represented in Figure 4.2. In this approach, Fabric sample was first placed underneath a rectangular piece of metal sheet, the length of which determines the sample size (here three levels considered: L= 15, 20, and 25 cm). Then, the peripheral fabric frame was exposed to hot air blown by a heat gun to fully consolidate the outer frame. Meanwhile, the metal sheet was pressured to the fabric by a massive block to make sure no hot air leaks to the central region of the fabric. The consolidated frame formed at the edges of the fabric resembles the arms in the picture frame fixture. After consolidating the outer frame of the fabric, the corners were cut to let the arms rotate around the corner joints daring the test. A sensor was attached to the mid yarn in the dry area to monitor the yarn strain during the test. Eventually, the fabric was then fixed at their two joints the axial displacement of which caused a shearing over the fabric.

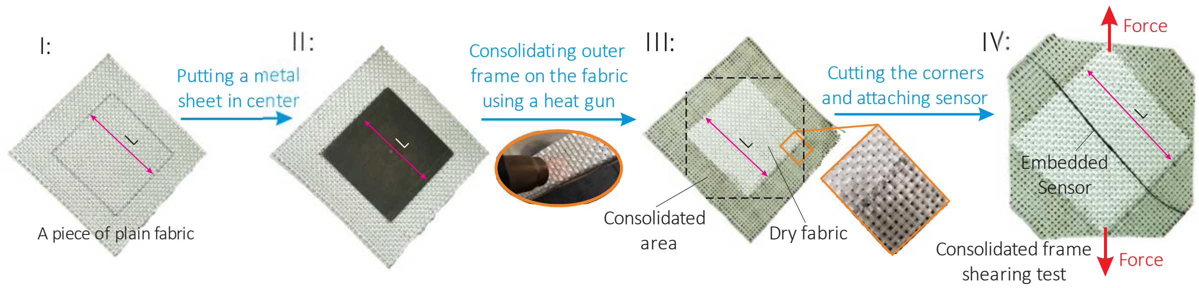

Figure 4.2. Sample preparation procedure in the frameless picture frame testing approach. In this method, the outer edge of the fabric is locally consolidated with a heat gun to introduce the shearing frame on the fabric itself instead of using a fixture.

4.5 A new integrated frameless shearing test set-up with embedded sensor

The shear characterization of woven fabrics was further enhanced through a needle integrated FPF testing scenario where the fabric is expected to undergo an 'ideal shearing'. The idea of using needle type clamping for fabric characterization has been discussed extensively and proven to be more effective for pure fabric characterization in Refs. [37, 204]. Figure 4.3 represents the testing procedure followed in this approach. First, the sample size was marked in a piece of fabric and two yarns adjacent to the four sides of sample region were taken out. Similar to the previous approach, a metal sheet with the same length as the sample size was located on the fabric covering the testing area. Samples were prepared with three different sample sizes of L= 15, 20, and 25 mm. Then, the outer frame was fully consolidated by a heat gun while a pressurized metal sheet avoided the leakage of hot air flow to the central region. Subsequently, the consolidated area with perpendicular yarns was cut so that at this stage the yarns were bilaterally consolidated in the fabric. Afterward, the needles were passed through the crossovers of the yarns at the boundaries (while the edges were sandwiched between the strips of transparency films located at both sides of the fabric for better stabilization of the needles). The locally consolidated ends of the yarns along with the strips of transparency film provided a rigid basis to both stabilize the peripheral yarns on the square boundaries of the fabric while rotating at the cross-overs; and also to avoid the peripheral yarns to be taken out of the fabric when loading. Finally, a sensor was embedded onto the fabric surface via gluing the sensor at two points close to the shearing frame along the mid yarn. The loading was then performed on two opposite crossovers at the frame joints.

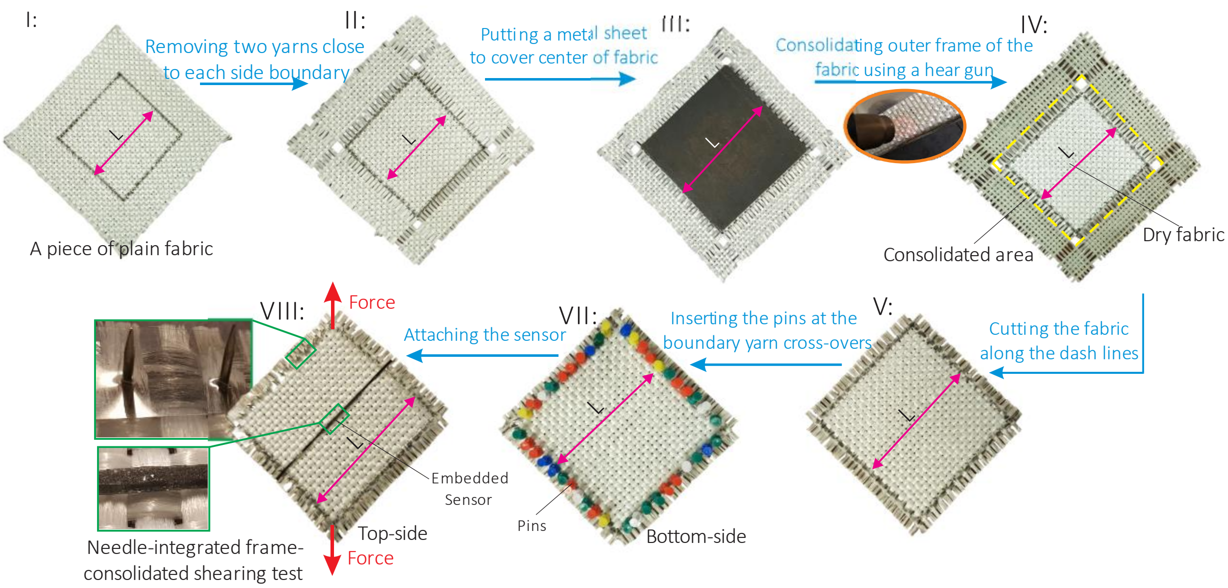

Figure 4.3. Sample preparation procedure in the needle integrated frameless picture frame testing procedure. The adjacent fibers in this approach were fully disconnected to allow the fibers rotate freely at the boundary cross-overs thereby prevent yarn bending during the test. The needles were inserted at the boundary cross-overs and the ends of the fibers were consolidated to provide a rigid basis for the needles and thereby avoid the boundary yarns to be taken out of the frame.

4.6 The novel fixtureless shearing tests versus conventional approaches

The results of the conventional picture frame test are very likely to be accompanied by a combination of the above-mentioned imperfections. The new test design in this study (described in Sections 4.5 and 4.6) is aimed to avoid these imperfections while the characterization of the pure shear behavior of the fabric. In the new frameless picture frame (FPF) test, aside from the simpler sample preparation process, a uniform full-size fabric with no corner cut-offs is subjected to shearing loads. In particular, in the needle integrated version of the FPF (Section 4.6), even the problem with yarn bending close to the frame was solved by letting the yarns to freely rotate around the frame boundary crossovers through the "one-row" stabilized needles in a locally consolidated fiber basis. Furthermore, owing to the high operator's control over the fabric, no misalignment/clamping edge-frame offset was introduced to the fabric due to the mounting. More details of the observations from the new test setups are discussed in the following section.

4.7 Severe deformation mechanisms: wrinkling patterns and yarn bending close to arms

Two most prominent features of the fabric deformation at high shearing loads (i.e. the out-of-plane wrinkling patterns [205] as well as yarn bending close to the clamps [41]) are compared in Figure 4.4 between the currently used as well as proposed testing procedures. The wrinkling in the fabrics can originate either from shearing beyond the locking angle at the local level, or due to the presence of global compressive loads on yarns (note that the latter causes wrinkling ahead of the locking/critical shear angle [206]). In our standard picture frame set-up, similar to previously reported observations [43, 45, 47, 48], the wrinkling commenced at the fabric arms (Figure 4.4(a)II) around frame shear angle of 40 deg. and it propagated over the entire fabric with further loading. In the standard bias extension test, the wrinkle was formed in the center at from shear angle of 40 deg. (Figure 4.4(b)). Among the above-mentioned test imperfections, each of the following cases can be responsible for such wrinkling pattern in the conventional picture frame test:

(i) A pre-sheared fabric misalignment leads to compressive continuum strains in the fabric arms; particularly the negative pre-shearing brings about a notable compressive strain to the arm (as was seen in Figure 3.4(b, c)) which grows faster with frame shearing, and hence adds to the likelihood of faster wrinkling in this region.

(ii) Positive offset of clamping edge from shear frame induces locally compressive strains in the arms (as was seen in Figure 3.5(d)).

(iii) Any frame/fabric shear angle mismatch can cause developing local compressive strains over the arms (Figure 3.6(a, b)III). In case of the shear angle at the central region falling behind the frame ($\mu<1$,) a faster locking is expected in the arms (Figure 3.6(b)I). As the proof of concept for the case of an extreme mismatch, wrinkling pattern formed by manually loading a rectangular fabric sample while one side being held firm (Figure 4.4(a); imitating the rectangular shape of the arms) resembled the core mechanism of wrinkling at the arm regions. This was in accordance with the fact that the locking, and thereby the onset of wrinkling, often occurs in the arm regions in the conventional picture frame test [43, 45].

Wrinkling in the proposed new frameless picture frame (FPF) test methods, however, had very different defect patterns than that of conventional picture frame test. A wrinkle was formed at the center of the sample in both original and needle integrated FPF methods, which was similar to the wrinkle formed in the bias extension test (Figure 4.4(c)II, (d)II). Apart from the wrinkling behavior, fiber bending close to the arms as a problematic issue was observed in both conventional picture frame and the original FPF tests (Figure 4.4(a)III, (c)III), but not in the bias-extension test. In opposite, in the needle integrated FPF setup, the fibers are given freedom to freely rotate at the boundary crossovers and hence, no visible yarn bending was observed at the boundaries of the samples, yielding a highly uniform and pure shear distribution over the fabric (Figure 4.4(d)III). In the bias extension test, as opposed to the FPF, three regions of shear (full shear or γ, half shear or $\gamma/2$, and no shear; $\gamma=0$) were formed [207, 208] (see Figure 4.4(b)).

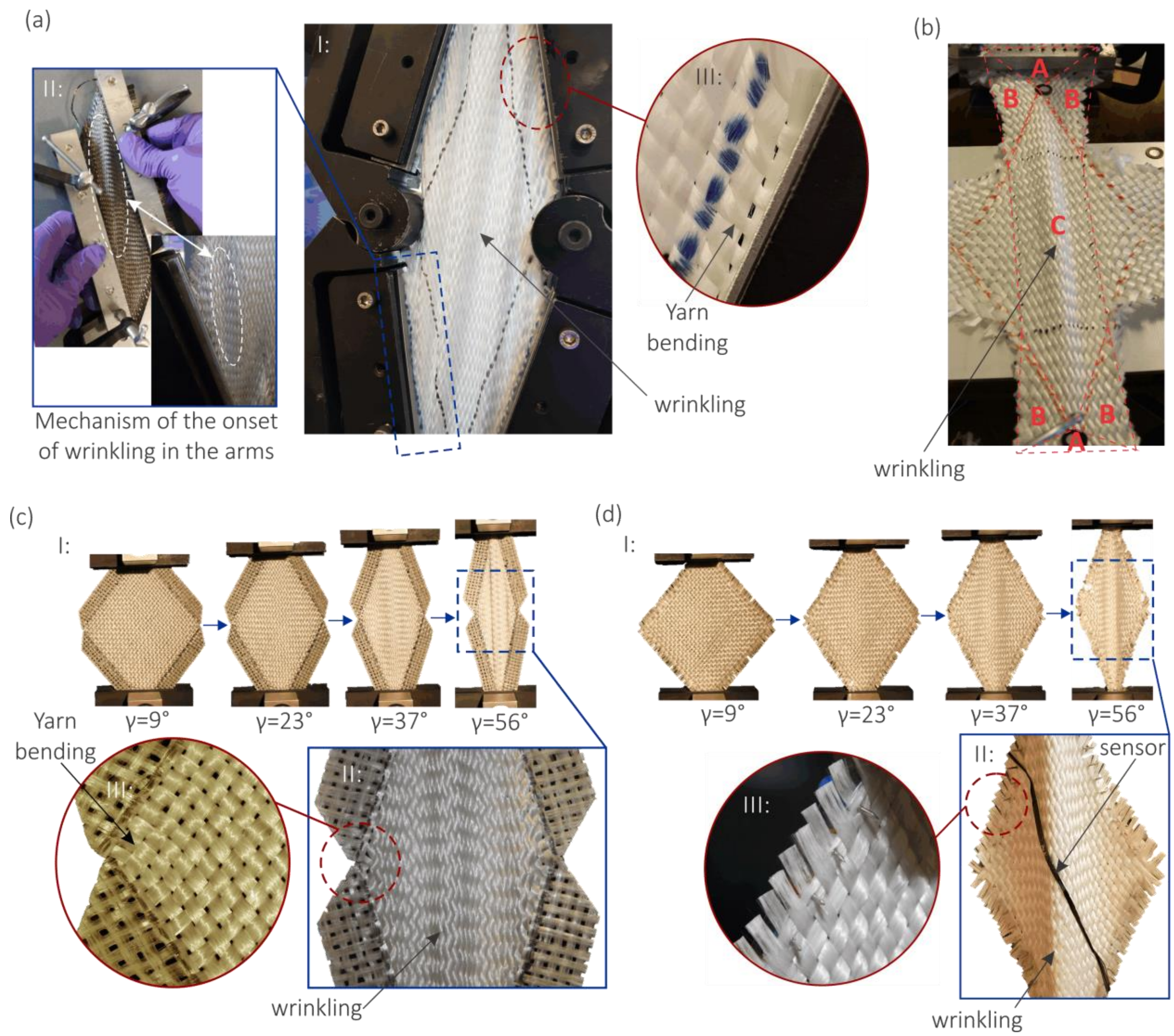

Figure 4.4. Illustration of severe defect formation mechanisms in woven fabrics. Wrinkling and yarn bending close to the arms are illustrated for (a) conventional picture frame, (b) conventional bias extension (regions A, B, and C refer to the areas with 0, γ/2 and γ shear angles, respectively), (c) frameless picture frame, and (d) needle integrated frameless picture frame tests. As opposed to the two proposed FPF setups, the wrinkling observed in the conventional picture frame test initiated from the arms and is not topologically consistent with the wrinkle seen in the bias extension test. In the needle integrated FPF, yarns become free to rotate at the boundary crossovers, thereby no bending close to the consolidated region was observed.

4.8 Comparing the normalized force-shear angle behaviors

The normalized force-shear angle responses associated with the conducted testing methods are presented in Figure 4.5. The reproducibility of the test methods was evaluated by repeating each experiment for three times, with the same sample sizes (w=15 mm in the picture frame and FPF tests, and w=75 mm, h=150 mm in the bias extension test). As seen from Figure 4.5(a), the highest normalized loads (0.173 – 0.312 N/mm) at the maximum 40° shear angle attained for the conventional picture frame test, which is clearly above those obtained for the bias extension test (0.037 – 0.055 N/mm). This can be attributed to the high potential for test imperfections in the conventional picture frame test leading the strain components along the yarns; also one should note that the higher force values, higher deviation from the pure shear mode. Such high forces in the picture frame test can be essentially explained by the local tensile loads induced to the yarns due to the non-uniform shear deformation (as shown theoretically in Sections 3.4-3.6). This can also account for the poor test reproducibility in the conventional picture frame setups since the imperfections can randomly vary from one test to another.

The amount of normalized load at 40° shear angle was reduced to (0.144 – 0.221 N/mm) for the FPF setup. Under a more controlled test sample preparation, mounting, as well as uniform fabric shape (with no corner cut-offs), the FPF provided a closer behavior to ideal shear, where the bending close to the arms still implied some flaw (thereby the discrepancies with the forces from the bias extension test). On the contrary, a highly reproducible shear response in the needle integrated FPF test was achieved where the maximum normalized load range (0.033 – 0.043 N/mm) was observed to be well within the range of bias extension test. In essence, treating the boundary conditions in this testing procedure has led to an ideal shear deformation mechanism, without different shear zones as present in the bias extension test.

The shear loads applied to the fabrics with different sample sizes suggest that the normalized shear response in the conventional picture frame test is size dependent (Figure 4.5(b)I), especially when it comes to smaller sample sizes. The larger the sample size, the higher normalized load is eventuated. This issue, though to a much less extent, still remained in FPF test (Figure 4.5(b)II). However, *in the needle integrated FPF test, the normalized force-shear angle behavior was seen* *to be by far less dependent on the sample size (*Figure 4.5(b)III). For the bias extension test, it is known that the choice of sample aspect ratio can have a significant effect on the occurrence of slippage and early wrinkles (the aspect ratio should be smaller than 2 [26]). Finally, the loading/unloading up to 40° shear angle (Figure 4.5(c)) indicated that the force dropped when loading was repeated for the second time in the FPF setup; and then subsequent loadings followed a consistent behavior. More consistent loading loops for the needle integrated FPF setup was obtained compared to the FPF test.

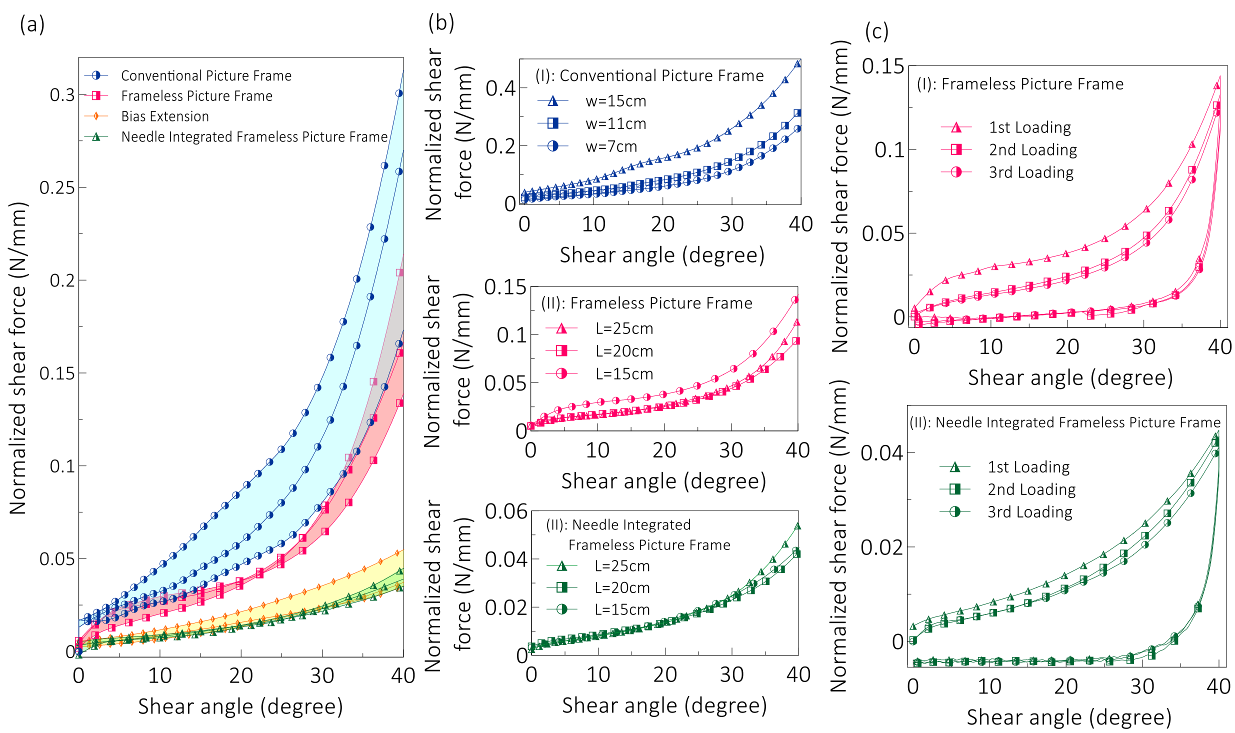

Figure 4.5. The shear response (normalized shear force versus shear angle) of the fabrics obtained following different testing methods. (a) repeatability of the tests through three repeats of each experiment, (b) the sensitivity of the normalized results, and (c) the loading/unloading response of the woven fabric obtained through I: FPF and II: needle integrated FPF tests. The needle integrated FPF test shows very promising results in terms of test reproducibility, sample size independency, and consistency of results with the bias extension test.

4.9 Summary of findings

Based on the comprehensive study implemented to find possible flaws in the PTF, a new testing scenario was designed in this chapter and its ability to express a more realistic shear behavior of fabrics was assessed compared to the PFT. The suggested testing approach involved inscribing the frame on the fabric sample itself, by means of locally consolidating the image of a PFT fixture on the fabric. In this way, a minimal manipulation is applied to the fabric during the sample preparation and subsequent mounting procedure, relieving the test from the misplacement and the potential faults related to the fixture as in the conventional PFT. In a second version of the new test, to remove close-to-clamp bending effects, a one-row needle set was employed at the cross-over located on the boundary edges and the adjacent yarns were disconnected by cutting the consolidated area after attaching the needle joints.

The mechanical behavior of atypical PP/glass fabric was characterized and compared through different shear test types. The random nature of normalized load-shear angle response stemmed from the imperfection effects can lead to a poor test reproducibility in the conventional PFT, while clearly more repeatable data were obtained in the case of PFTs. In particular, more repeatable results were attained for the needle integrated version of FPF test. Since there have been some debates in the literature in terms of force normalization and generalizing the mechanical behavior of the fabrics, the conducted study on the sample size effect in this Chapter also revealed consistent results (with very minimal dependency on sample size) in the case of needle integrated FPT.

From the perspective of deformation mechanism, a center-originated wrinkling could be observed in both FPF versions, similar to that of the BET. This is mainly owing to the square-shape sample in FPF with more uniform shear angle distribution, rather than a cross-shaped sample in the conventional PFT which divides the fabric into different deformation regions with different shear rigidities and thereby a shear angle gradient over the sample (especially in the presence of common imperfections as discussed in Chapter 3). In addition, letting the yarns to rotate freely at the cross-overs in the needle integrated FPF could overcome the issue of local yarn bending and further minimized the shear load magnitude. The above observations confirmed that the new suggested testing method can significantly enhance characterizing shear behavior of fabrics.

Chapter 5: Sensor fabrication and characterization for integration with woven fabrics

5.1 Overview

In order to apply strain sensors for a specific monitoring application, the piezoresistive characteristics such as resistance-strain behavior should be studied, in order to confirm that the sensor is properly sensitive and stretchable in the given range of loads. The strain sensors are basically obtained by introducing electrical pathways into a non-conductive matrix of the composites which induces piezoresistive properties for measuring strain. When deformations in the internal material structure under mechanical loads occur, the electrical resistance changes due to the reconfiguration of the electrical network. In this chapter, the electromechanical behavior of new yarn-like chopped carbon fiber (CCF)/polydimethylsiloxane (PDMS) composites as a promising sensor for capturing the deformation ranges occurring in the picture frame test is evaluated. The sensor was specifically tailored for integrating within woven composite structures and its performance was evaluated under tensile, cyclic, and monolithic loads. Due to the high specific surface area of the CCF fillers, a low percolation threshold of 1.41 wt.% was attained with high sensitivity and stretchability for the samples with low CCF contents (gauge factors as high as 700 at first cycle). The piezoresistive behavior was observed to be uniquely strain-reversible at higher cycles.

5.2 Materials and Methods

5.2.1 Materials

Twill weave carbon fiber fabrics were supplied by ACP Composites Inc. (Livermore, CA) with fibers of 0.012" in thickness and 3K Carbon Fiber Standard Modulus PAN, 33MSI fiber type. The carbon fibers were chopped manually (referred to CCF from now on) to the segments of approximately 1 mm and soaked in acetone for 2 hours to remove the non-conductive thermosetting epoxy resin layer coated on the fibers. This process enhances their electrical conductivity. PDMS (Sylgard 184 Silicone Elastomer) and its curing agent were purchased from Sigma-Aldrich Corp., USA. The PDMS monomer and curing agent were prepared by mixing with

1:10 weight ratio. Then, the CCF/PDMS mixture was obtained through mechanical mixing with the specific weight ratios (including 1.90 wt.%, 2.46 wt.%, 4.83 wt.%, and 5.88 wt.%).

5.2.2 Sensor fabrication procedure

The fabrication steps followed for preparation and testing of the CCF/PDMS composites are illustrated in Figure 5.1. To fabricate the CCF/PDMS piezoresistive composite sensors, two 1.25-mm thick glass slides were put next to each other on the top of a glass plate at a 3-mm (edge-to-edge) distance (specifying the width of the samples) forming the mold. Two carbon fiber (CF) tows were used as electrodes since (i) they are structurally similar to and compatible with fabrics, and (ii) can be better integrated with the CCF/PDMS piezoresistive sensor. The CF tows were located into the channel(s) at a 22-mm distance (this distance defines the length of the sensors). Then, the prepared CCF/PDMS mixture was injected (using a syringe) into the channel(s), formed through the gap between the two glass slides. To prevent the CCF/PDMS mixture from flowing further into the CF electrodes, the samples were cured on the hotplate at 150˚C for 30 min. Thereafter, the composite sensors were obtained by peeling the cured sensors off from the channel.

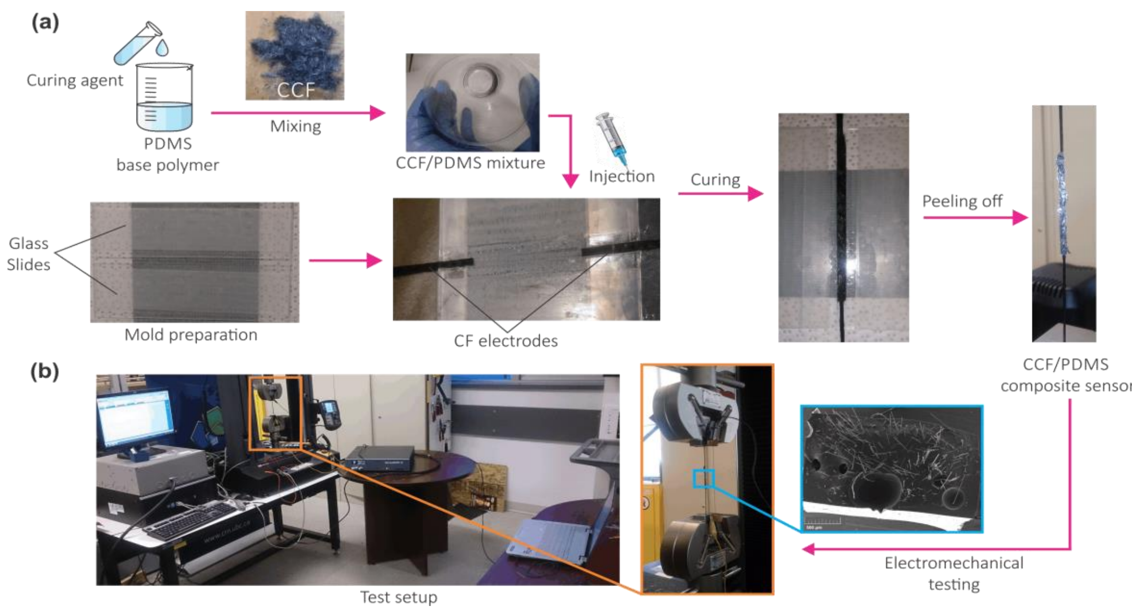

Figure 5.1. Overview of the steps followed for (a) fabrication and (b) electromechanical evaluation of the CCF/PDMS sensors. The sensors were fabricated through mechanical blending of CCF and PDMS base polymer.

5.2.3 Characterization

Mechanical performance evaluation and loading were conducted using a universal testing machine (Instron 5960, USA) as shown in Figure 5.1(b). The fixtures were electrically insulated to prevent electrical leakage through the testing instrument. Since the CF electrodes were well incorporated into the cured sensors, the samples were mounted into the fixtures through the CF electrodes with no pre-conditioning. Hence, the results present the properties of the sensors as fabricated. All of the mechanical tests were executed with a cross-head loading rate of 8 mm/min. In order to evaluate cyclic piezoresistivity of the composite, the loading was repeated for 100 cycles at 3% and 5% strain magnitudes, separately, and thereafter the load was held for 600 s to capture the electrical and mechanical relaxation behavior of the composite. Another set of samples was also subjected to the full-tensile loading to address the failure characteristics of the sensor material. The force-displacement data was generated during the tests, based on which the stress was defined as the axial loading per unit of the initial cross-sectional area ($\sigma = F/A$). The corresponding strain was obtained by dividing the cross-head displacement by the initial sensor electrode-to-electrode distance ($\varepsilon = \delta/L_0$). Elastic modulus of the specimens was obtained from the linear portion of the stress-strain data in full tensile loading tests.

The electrical conductivity of the samples was measured by a VersaSTAT4 potentiostat (Gamble Technologies Ltd., Canada) through a two-probe configuration using the CF tows as the electrical electrodes. During the experiments, the instantaneous resistance was calculated for the samples through the current response measured under 1 V (DC) applied to the sensor probes. Subsequently, the change in the resistance was normalized by the initial resistance. This is presented as the relative resistance change (${}^{\Delta R}/{}_{R_0}$). The gauge factor (GF) is typically defined as Eq. (5.1):

$$GF = \frac{{}^{\Delta R}/{}_{R_0}}{\varepsilon_0} \quad \textbf{(5.1)}$$

in which R_0 is the initial resistance. ε_0 is the amplitude strain.

The GF is basically obtained from the slope of the line fitted to the non-linear resistance-strain curve loading and unloading regimes of each cycle. The volume conductivity (σ_V) was also obtained by Eq. (5.2):

$$\sigma_V = l/R_v A \qquad \textbf{(5.2)}$$

where R_v is the resistance. A and l represent the cross sectional area and sensor length, respectively.

To understand the microstructural mechanism of failure in the sensors, the scanning electron microscopy (SEM) images were taken from the samples (using a Tescan Mira XMU Scanning Microscope) at 20.0 KeV accelerating voltage. For this purpose, the sample surface was sputtered with platinum and then placed into the vacuum chamber for subsequent imaging processing. Moreover, the in-situ deformation mechanism of the CCFs into the PDMS matrix was visualized by manually pulling and releasing the sensor under a microscope.

5.3 Results

5.3.1 Electrical conductivity and percolation threshold

Figure 5.2 represents the variation in the volume conductivity of the CCF/PDMS composites as a function of the CCF filler content. Similar to the typical carbon-polymer based composites [209], increasing the concentration of the CCF leads to a drastic increase in conductivity at a certain CCF concentration which is referred to as percolation threshold (P_c). Conductivity of the CCF/PDMS composites increases by ~6 order of magnitude as the CCF loading is increased from 0.75 wt.% to 1.5 wt.%, implying the formation of the percolation network in this range of the CCF content. The conductivity measurements were performed for three samples of each CCF concentration. The range of the values obtained for the samples with the same weight percentage indicates the non-uniformity of CCF distribution and the dispersion quality.

A classical percolation model is used to correlate the electrical conductivity to the filler concentration (P) and the percolation threshold (P_c) as indicated in Eq. (5.3) [210]:

$$\sigma_e = \sigma_{e0}(P - P_c)^n \tag{5.3}$$

where σ_e is the electrical conductivity, σ_{e0} is the scaling factor, and n represents the exponential coefficient (or the dimensionality of the conductive network). Fitting the above equation to the data presented in Figure 5.2 provides the values of $P_c = 1.41\ wt.\%$ and n=1.14.

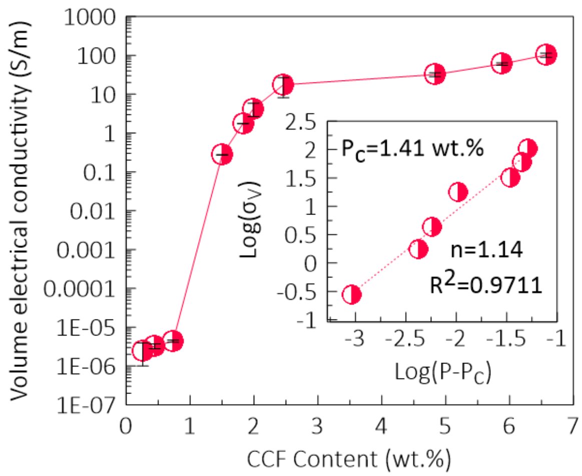

Figure 5.2. Variation in the volume electrical conductivity as a function of the weight fraction of the CCF content. A percolation model implies the threshold of 1.41 wt.% for the CCF/PDMS composites (the inset represents the parameters associated with the scaling percolation model).

5.3.2 Piezoresistive behavior under cyclic loads

In order to examine the cyclic electromechanical behavior of the CCF/PDMS composites, the tensile stress, as well as the resistance change, was monitored in 100 tensile loading cycles. Figure 5.3 depicts the results of the first 10 cycles for different CCF concentrations at two strain levels (i.e. 3% and 5%). The results show that the tensile stress varies linearly with the strain. At the 3% strain level, there is no obvious mechanical hysteresis in the stress response over the entire cyclic load; whereas the magnitude of stress decreases with time for the 5% strain level. On the other hand, the change in the relative resistance exhibited a more complex behavior: the first cycle showed a highly-sensitive and linear response with a smooth increase in the resistance value; in the subsequent cycles a decrease in the resistance was observed at the onset of each cycle indicating a negative piezoresistivity. This behavior in the loading portion of each cycle was altered to a positive resistivity at a transition strain where a change from negative to positive piezoresistivity occurred and caused the resistance to increase to a maximum value at the highest strain level. Likewise, the unloading portion of each cycle commenced with a decrease in resistance followed by a positive to negative piezoresistivity change at a transition strain. Comparing the results in Figure 5.3 for different CCF contents demonstrates that the extent to which the electrical resistance amplitude reduces in each loading/unloading regime is proportional to the CCF concentration.

Albeit the resistance change was seen to significantly decrease at the first cycles, the resistance-strain behavior was highly repeatable as the loading was repeated at higher cycles. The results in Figure 5.3 also show more degradation in sensitivity for 5% cyclic strain compared to that of the 3% cyclic strain. Overall, ${\Delta R}/{R_0}$show a significant variation range over time: at the lowest CCF weight ratio (i.e. 1.90 wt.%), the resistance increases by 32.5 and 40 times for the strain levels of 3% and 5%, respectively. The comparison between the corresponding maximum values of ${\Delta R}/{R_0}$ for each cycle and different CCF ratios suggests a decrease in the peak resistance value (from one cycle to the next) as the CCF concentration increases for both strain levels. For instance, at the 5% cyclic strain, the maximum value of ${\Delta R}/{R_0}$ in the first cycle is 40 for 1.90 wt.% CCF which is reduced to 3.3 when the CCF content is increased to 5.88 wt.%. It is worth noting that the maximum of ${\Delta R}/{R_0}$ in the first cycle of the 5% stain is significantly higher than that of 3%; however, in the subsequent cycles this trend is reversed.

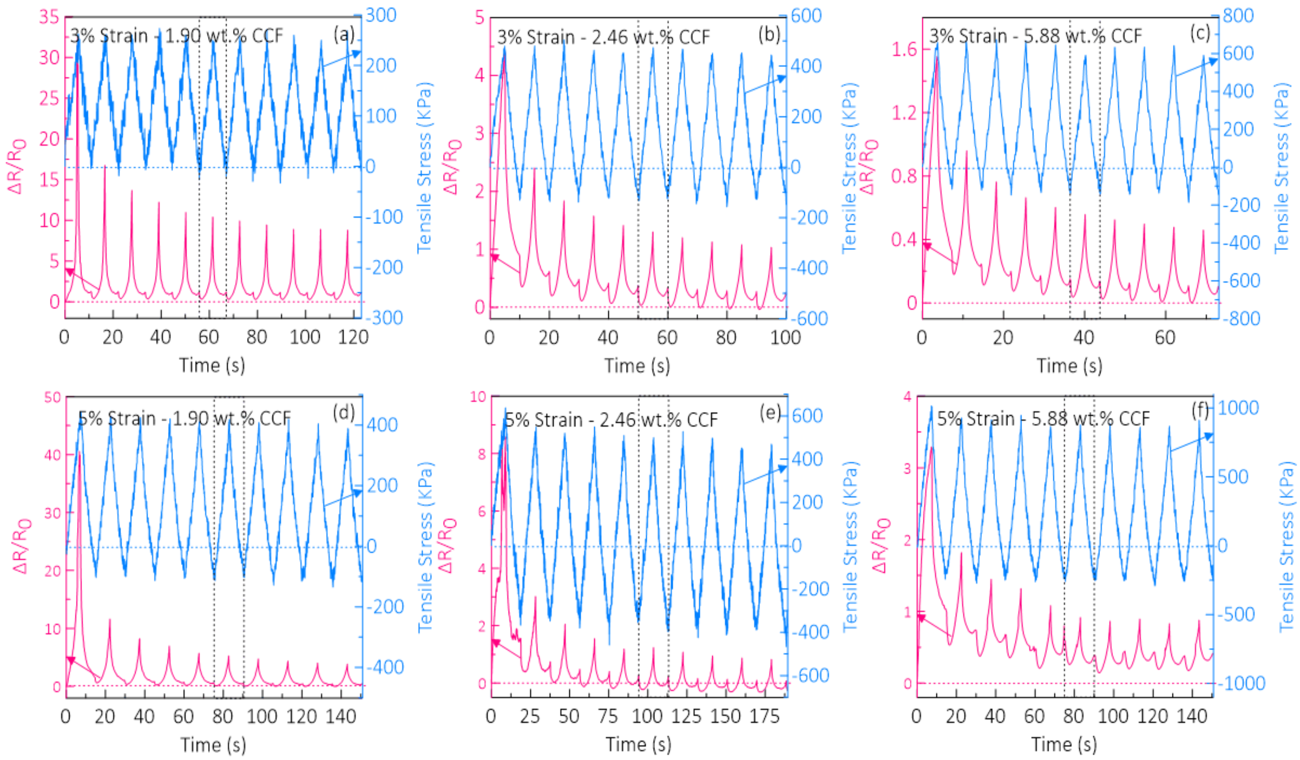

Figure 5.3. First 10 cycles electromechanical behavior of the CCF/PDMS composites at 3% strain amplitude. The results obtained for (a) 1.90 wt.%, (b) 2.46 wt.%, (c) 5.88 wt.% CCF contents and for 5% strain amplitude for (d) 1.90 wt.%, (e) 2.46 wt.%, (f) 5.88 wt.% CCF contents. The electrical resistance continuously increases in the first loading and the next cycles are commenced with decreasing the resistance up to a piezoresistivity transition point (negative piezoresistivity) after which the resistance is increased with the load (positive piezoresistivity).

5.3.3 Sensitivity analysis in cyclic loading

To gain better insights into sensitivity and the electromechanical performance of CCF/PDMS sensors, the gauge factors (GFs) are obtained at each cycle for both loading and unloading regimes at two different strain magnitudes of 3% and 5%. The results, presented in Figure 5.4, indicate a large gauge factor in the first-cycle (for all of the sample configurations) followed by a sudden drop reaching a plateau at subsequent cycles. This steady value of the gauge factor implies a satisfactory strain-reversible behavior. As it can be seen in Figure 5.4, the GF results demonstrate that increasing the CCF contents leads to a significant decrease in sensitivity.

for the smaller cyclic strain magnitude of 3%, the highest gauge factor was observed for the sample with the lowest CCF weight ratio (i.e., 1.90 wt.% CCF). In this sample, a first-cycle loading gauge factor of 233 was attained reaching to the steady value of 50 (at 3% cyclic strain) at subsequent cycles; the corresponding gauge factors were 195 and 25 in the unloading regime. In general, the gauge factor during unloading was found to be lower than that of loading for all of the samples. The comparison between the results obtained at 3% and 5% cyclic strains signifies that the application of higher strain levels yields a lower gauge factor at steady state (after the first cycle) and by far higher at first cycles. For example, the first-cycle loading gauge factors at 5% and 3% were found to be 702 and 233, respectively, for the sample with 1.90 wt.% CCF while the figures at the last cycles were almost 25 and 50, correspondingly.

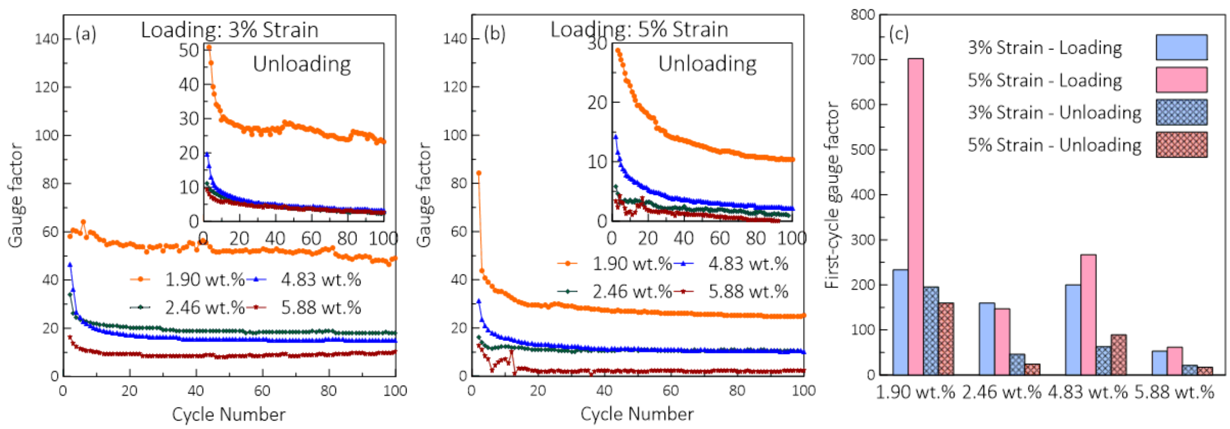

Figure 5.4. Loading gauge factor results obtained after the first-cycle for the CCF/PDMS composite sensors with different CCF contents at cyclic loads. The results are presented for (a) 3% and (b) 5% strain amplitudes (the insets show corresponding gauge factors in unloading regime). (c) The first-cycle loading/unloading gauge factor results for different strains and CCF concentrations. Lower CCF weight ratios lead to higher sensitivity and piezoresistive stability. The results imply a strain-reversible piezoresistive behavior at higher than ~10 loading cycles with more sensitivity in loading than unloading.

5.3.4 Piezoresistive non-linearity: Piezoresistivity transition in cyclic loading

As shown in Figure 5.5, the electromechanical behavior of the CCF/PDMS composites were accompanied by a negative-to-positive piezoresistivity transition at transition strain (ε_t). In order to characterize this behavior in more depth, the normalized transition strain ($\varepsilon_t/\varepsilon_0$) in the loading and unloading regimes for each cycle is obtained for different CCF weight ratios and at two strain levels (see Figure 5.3). Overall, the transition in piezoresistivity is observed to delay after the first cycle. Then, for the subsequent cycles, the transition strain gradually reaches a plateau (referred to as steady transition strain). The results indicate that the magnitude of the applied cyclic strain has a significant effect on the transition point: at 3% strain, the steady transition strain is reached at almost 20% of the total strain in the loading regime and between 20% and 40% in unloading regime (regardless of the CCF content ratio). However, the effect of the CCF concentration is clearly evident at 5% strain such that a faster transition is observed in the samples with the lower CCF ratio while a normalized transition strain as high as ~0.6 is found for 5.88 wt.% CCF.

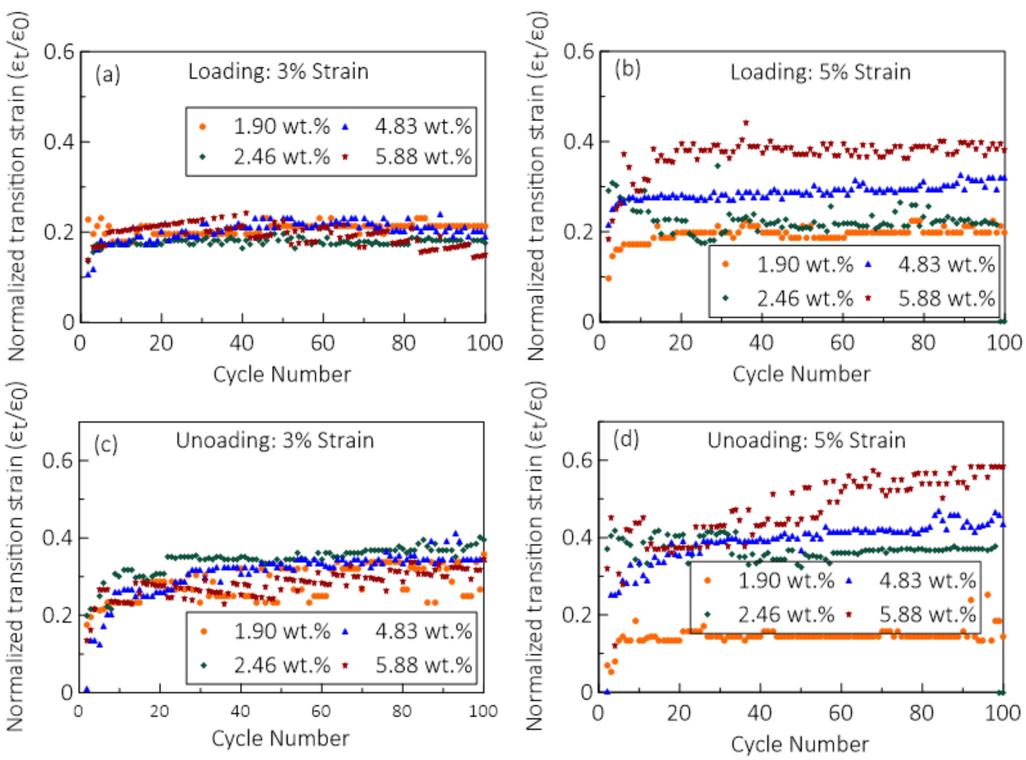

Figure 5.5. Variation in the normalized transition strain ($\varepsilon_t/\varepsilon_0$) as a function of loading cycles at 3% strain amplitude. The results presented here are related to (a) loading and (c) unloading, as well as 5% strain amplitude in (b) loading and (d) unloading regimes. The piezoresistivity transition effect is exacerbated with the increase in the CCF content and the load amplitude.

5.3.5 Electrical and mechanical relaxation

One of the main issues associated with the polymeric piezoresistive composites is their time-dependent electromechanical properties [211]. Figure 5.6 compares the electrical as well as mechanical relaxation behavior of the CCF/PDMS composites after application of the cyclic strains. For the electrical relaxation curves (Figure 5.6(a, b)), the electrical resistance diminishes abruptly at the beginning of the relaxation process. Then, it continues to decrease at a lower rate until reaching a steady resistance. Generally, increasing the CCF content not only leads to a lower resistance drop but also causes the relaxation process to reach the steady state faster. For instance, the resistance after 10 minutes of holding 3% tensile strain decreases by 10.3% and 32.9% for the 5.88 wt.% and 1.90 wt.% CCF/PDMS composites, respectively. Mechanical relaxation almost follows the same behavior/trend as the electrical relaxation, except for the fact that no drastic drop in stress was observed at the start of the relaxation process (see Figure 5.6(c-e)). Also, the time-dependent stress variation is less than time-dependent resistance variation, as observed for different CCF contents in Fig. 6(c-e): e.g., 12.8% mechanical relaxation versus 23.8% electrical relaxation after 10 min for the 2.46 wt.% composite subjected to 3% loading.

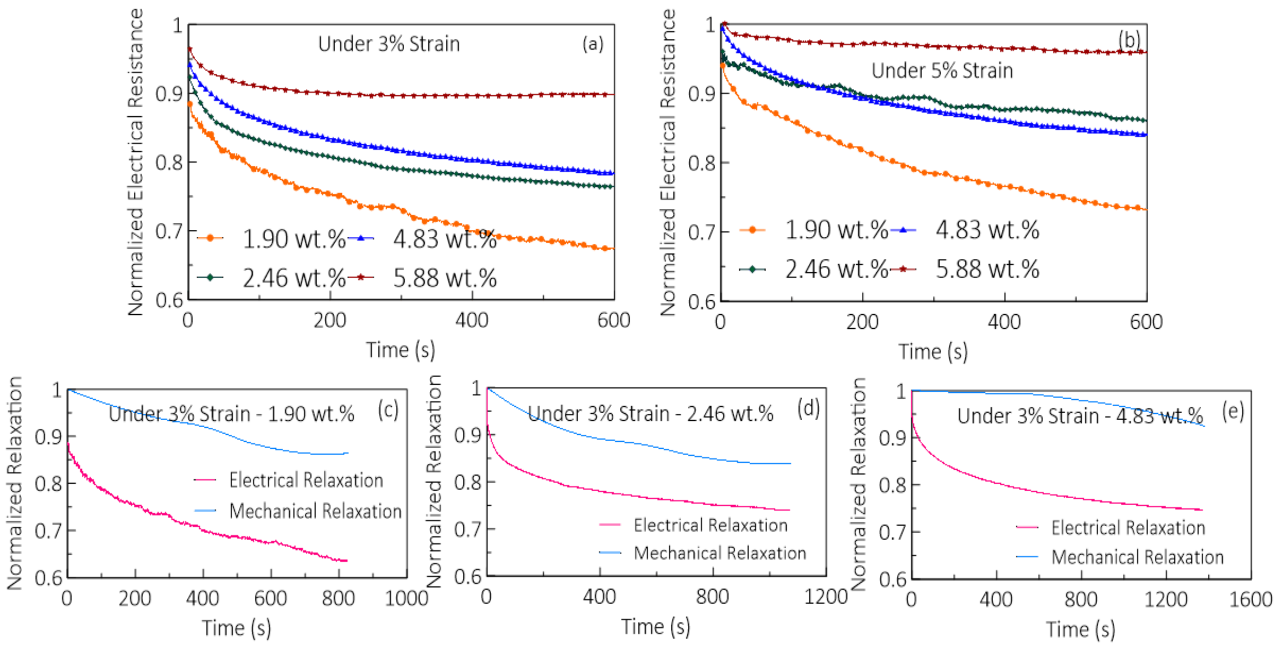

Figure 5.6. The relaxation behavior of the CCF/PDMS composites. Electrical resistance versus time at (a) 3% and (b) 5% tensile strain for the composites with different CCF contents. Mechanical stress and electrical resistance relaxations at 3% strain for (c) 1.90 wt.%, (d) 2.46 wt.%, (e) 4.83 wt.% CCF contents. The less relaxation behavior was observed for the CCF/PDMS composites with higher CCF contents. Electrical relaxation is mainly originated from the polymer matrix creep; whereas the mechanical stress relaxation is related to inherent properties of the polymer.

5.3.6 Failure tests

The electromechanical response of the piezoresistive composites under a continuous tensile loading up to the fracture point is illustrated in Figure 5.7 for different CCF contents. From a mechanical standpoint, the stress-strain behavior of the samples initiated with a linear portion (elastic region) followed by a post-yield hardening until the breakpoint was reached. Table 5.1 summarizes the mechanical properties obtained from the stress-strain curves. Generally, the elastic slope, as well as the elastic limit, increases with the addition of the CCF content; however, a rupture occurs at higher tensile strains for lower CCF contents as compared to higher contents. Increasing the CCF content from 2.46 wt.% to 4.83 wt.% increases the elastic modulus and elastic limit by 101.3% and 60.5%, respectively. The variation in the relative resistance as a function of the tensile strain follows an identical trend for the samples with 4.83 wt.% and 5.88 wt.% CCF. In these samples, specifically, the electrical resistance persistently increases with the tensile strain up to the elastic limit ($^{\Delta R}/_{R_0}$ reaches ~6 at this point for both CCF concentrations) and thereafter becomes unstable as the fluctuating signals are observed at higher strains. However, for the case of 2.46 wt.% CCF content, the resistance was drastically augmented after 0.07 strain due to conductive network disconnection [64].

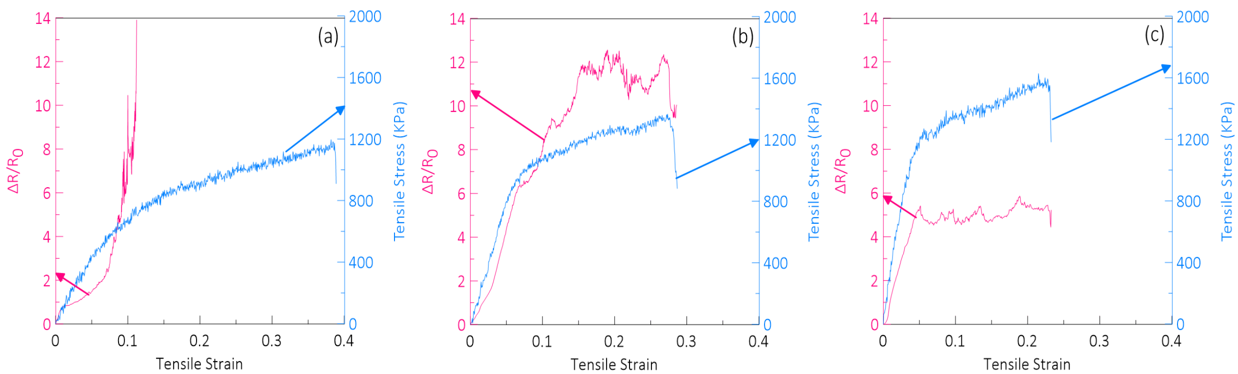

Figure 5.7. Resistance change and tensile stress induced by tensile loading. The results presented for composites with (a) 2.46 wt.% (b) 4.83 wt.% and (c) 5.88 wt.% CCF contents. Although piezoresistive composites with lower CCF contents possess higher sensitivity, disruption in the conductive network occurs faster at high strains. For higher CCF contents, the same trend is observed in terms of the resistance change and mechanical stress.

Table 5.1. The mechanical properties obtained based on the stress-strain response curves for the composites with different CCF contents.

CCF content (wt.%)	Elastic Modulus (MPa)	Yield Strength (MPa)	Rupture strain
2.46	8.17	0.58	0.39
4.83	16.45	0.93	0.29
5.88	32.56	1.11	0.23

5.4 Discussion

5.4.1 Conductivity characterization

Chopped carbon fibers (CCFs) are mechanically dispersed in the PDMS matrix, randomly and non-uniformly fiber distribution is expected. Consequently, different electrical conductivities, and thereby different electromechanical responses, were obtained for samples with the same CCF concentrations (Figure 5.2). In terms of the general percolation model (presented in Eq. (5.3)), the exponential value of n is believed to show the conductive mechanism such that the values of $n = 2$ and $n = 1.3$ refer to the 3D and 2D conduction networks, respectively.[212] Hence, in the present work, the exponential value of $n = 1.14$ implies a 2D conductive network which is close to those reported for the case of poly(ethylene)/carbon nanotubes (CNT) ($n = 1.4$) [213] as well as PDMS/CNT composites ($n = 1.42$).[212] Although high values of n are assigned to the quantum tunneling effect [101], the low exponential constants can also be due to high polarity of the polymeric matrix [214].

The resistance while holding the strain (followed by cyclic loading) shows a time-dependent behavior. The observed resistance relaxation in Figure 5.6 is similar to the stress relaxation, except that the stress relaxation is originated from the polymer chain motion, while the resistance relaxation comes from the change in relative distance between the CCFs [214].

5.4.2 Structural characterization prior to loading

In CCF/PDMS composites, the chopped fibers are randomly distributed but remain straight in the PDMS matrix during and after the curing process. Dispersion of the fibers seemed to be non-uniform, as in some regions more aggregated/concentrated fibers are observed (see Figure 5.8(b)). This is due to the fact that the PDMS/CCF mixture was made through mechanical stirring. Also, the bilateral flow of PDMS during the curing process can exacerbate fiber aggregation. Prior to loading, CCF/PDMS samples fabricated contains CCFs forming channels inside the PDMS matrix. These CCFs are connected in a way that an electrical network is formed within the structure.

5.4.3 Failure mechanism

Figure 5.8 illustrates the SEM images of the cross-section of CCF/PDMS samples after failure. These samples contained 4.83 wt.% CCFs and were exposed to the full tensile load. The footprints of the CCFs pulled out from the channels can be observed in Figure 5.8(c). As the PDMS matrix undergoes high strain tensile load, the channels become tighter due to the Poisson's effect. Then, CCFs are separated or pulled out from one side of the failed sample while the polymer flows until rupture. Also, there is an evidence of CCFs locally confined in the composite where wall separation and local breakage can be observed (see Figure 5.8(d)). As the full tensile test was performed after the cyclic loading, the channels containing CCFs seem to loosen progressively as demonstrated in Figure 5.8(d). The electromechanical responses under tensile tests (Figure 5.7) reveal that at the low CCF concentration of 2.46 wt.% the sensor loses its conductivity far prior to the material failure. However, it does not apply to the case of 4.83 wt.% and 5.88% wt. CCF contents. For the two latter cases, post-yield resistance fluctuations can be interpreted due to the high local concentration of CCFs and/or high void density at the failure areas.

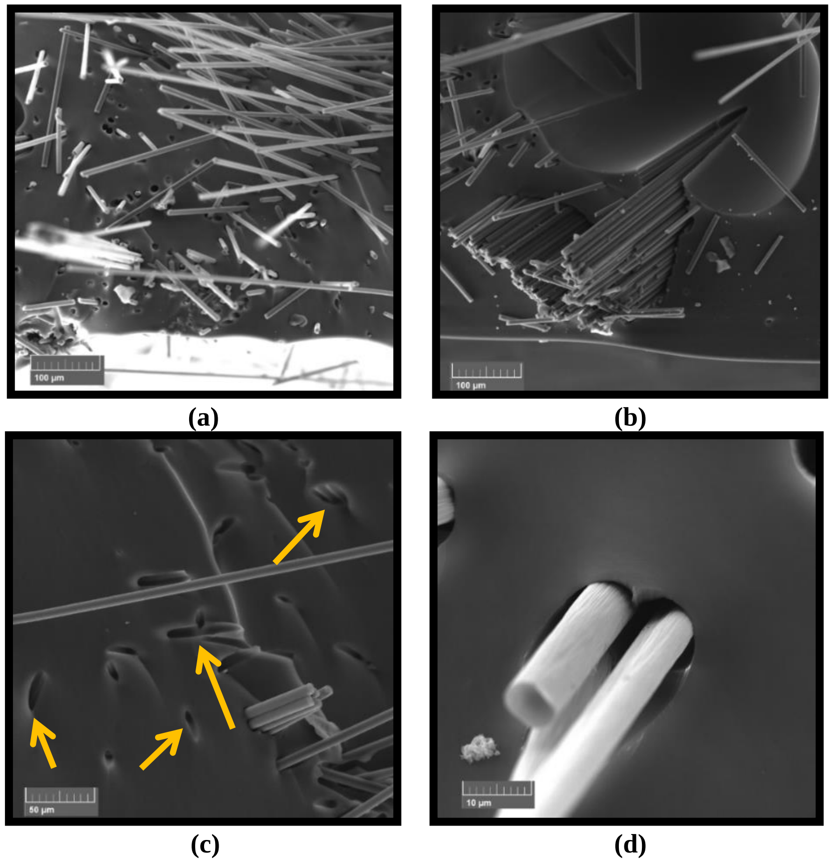

Figure 5.8. SEM images of the failure surface for the 4.83 wt.% CCF content in CCF/PDMS composite. (a) The overall random distribution of the carbon fibers into the PDMS matrix. (b) Carbon fiber aggregation and voids formed into the PDMS matrix. (c) The channels where the carbon fibers are trapped in and pulled out after failure. (d) The carbon fibers loosened into the channels due to the severe deformation.

5.4.4 Piezoresistive mechanism under cyclic loading

It is expected that the change in resistance in the piezoresistive materials primarily occurs due to the structural evolutions and reconfiguration of the conductive network when the material is subjected to the external loading [215]. Figure 5.9 presents schematically the progressive structural evolutions (or deformation mechanism) based on the in-situ microscopic images of the CCF/PDMS deformations. As the tensile strain is applied to the sensor for the first time (point I in Figure 5.9(c, d)), the channels containing the CCFs are deformed according to their orientations relative to the loading direction. The channels parallel to the loading direction (vertical channels) are enlarged; whereas those perpendicular to the loading direction (horizontal channels) tend to radially expand. In all cases, the CCFs inside the channels remain intact due to the weak adhesion at the interface between CCFs and PDMS. As a result, bilateral gaps start to develop at one or two sides of every single carbon fiber (inclined and vertical fibers), leading to a full disconnection between the adjacent fibers at these local areas (as shown in Figure 5.9(a)). This disconnection is the main reason for the increase in the electrical resistance (see the increase between points I and II in Figure 5.9(c, d)). The radial expansion of the horizontal channels also exacerbates the separation of crossing carbon fibers (which are electrically in touch), leading to deterioration of the conductive network as the loading is applied for the first time. Meanwhile, the viscoelastic properties of the matrix polymer cause residual/permanent deformations, thereby carbon fibers are loosened into their channels.

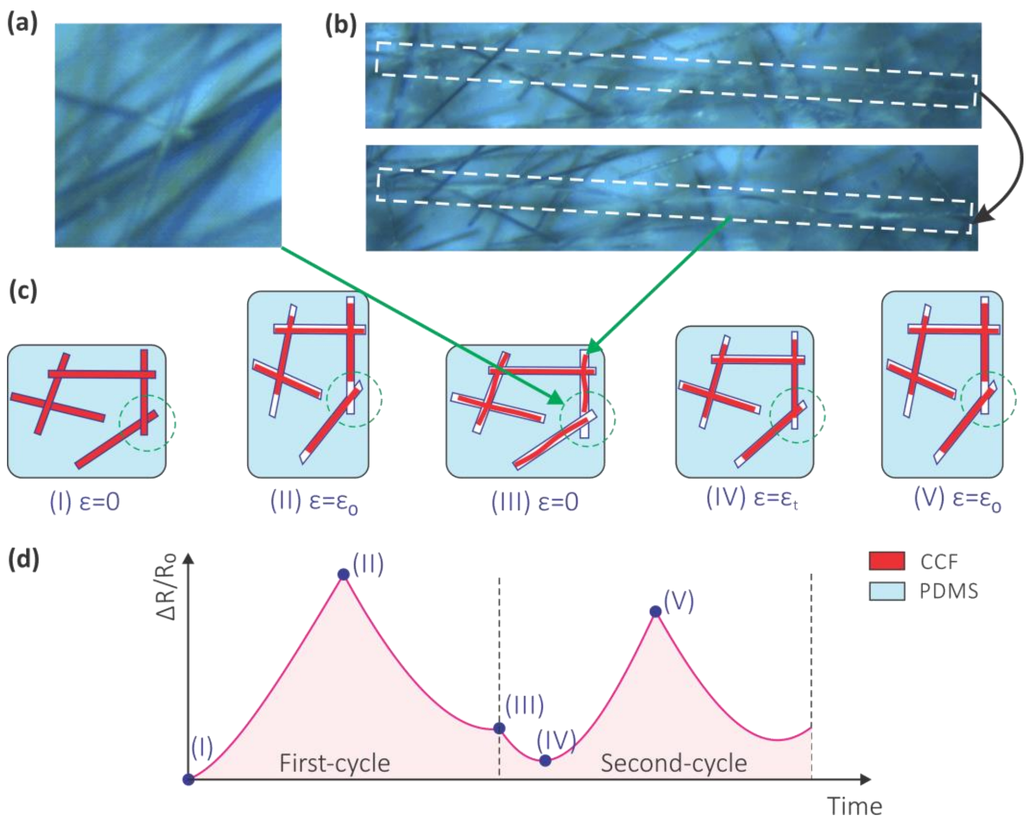

Figure 5.9. Fiber deformation in the PDMS matrix observed in the in-situ macroscopic images. (a) Formation of the bilateral gaps in the stretched channels carrying CCFs. (b) Buckling mechanism of the CCFs during the unloading period. (c, d) Schematic representation of the resistance-strain-structure relationship with regards to the presented deformation mechanism.

The described deformation mechanism explains the reason for the increase in the resistance with strain (pure positive resistivity) in the first loading. However, when the sensor is unloaded for the first time (see point II in Figure 5.9(c, d)), the fibers do not essentially come back to their original state. Instead, the interfacial friction at the CCF/PDMS interface causes the carbon fibers to permanently buckle and hence shrink [216] instead of switching back to their initial state and filling the bilateral gaps as illustrated by microscopic images in Figure 5.9(b). As a result, the carbon fibers form into a helical shape after unloading (Point III in Figure 5.9(c, d)). This along the viscoelastic deformations introduces permanent deformations (interfacial friction induced deformation) to the entire sensor structure, and as a result, sensor loses its strain recoverability. Hence, a higher electrical resistance (relative to the initial resistance) is expected at the end of the first cycle, which is confirmed by the results shown in Figure 5.3 where the difference between the initial and after-first-cycle resistances are also augmented with increasing the CCF content.

At the onset of the second cycle, the sensor was slightly under compression due to the above-mentioned residual deformations. When the loading is repeated for the second time, the fibers initially resume their original straight shape (from the helical shape), leading to a decrease in the resistance (implying a negative piezoresistivity). This behavior continues up to a transition strain (point IV in Figure 5.9(c, d)). Upon the application of further loading, the distance between the fibers increases with strain, similar to the process occurred in the first-time loading (point V in Figure 5.9(c, d)). In essence, the transition from negative to positive piezoresistivity due to loading (and vice versa during unloading) can be explained based on the transition from the straight to helical shape; the mechanism which repeats over the subsequent cycles. However, the magnitude of $\Delta R/R_0$ decreases in the following cycles (Figure 5.3) which is attributed to the accumulated loosening of the carbon fibers and residual deformations during cyclic loading.

It is worth adding that the piezoresistivity transition strain (Figure 5.5) overlaps with the strain at which the stress approaches zero (zero-stress point or $\varepsilon_{(\sigma=0)}$), which further supports the deformation scenario explained above. The previous researchers have also reported the same transition for piezoresistivity in case of carbon nanotube/polyurethane [99, 119, 217], weft-knitted UHMWPE/PANI yarns at high strains [123]. However, they have suggested that when the sensors are loaded (although the load itself causes the conductive network to disrupt and thereby the resistance to increase) the transverse shrinkage due to the Poisson's effect improves the conductivity (since it strengthens the tunneling quantum conductivity). Since at the beginning of each cycle, the Poisson's effect dominates fiber separation, the electromechanical behavior is said to commence with negative piezoresistivity followed by positive piezoresistivity after a transition strain. Yet, this hypothesis alone does not explain the continuous increase in the resistance at the first-cycle loading. Despite the justification made by others for negative piezoresistivity through the transverse shrinkage [218], this shrinkage ‘alone’ does not necessarily lead to higher electrical contacts as a result of narrowing the distance between the fiber (happening as a result of applying the axial tensile strain). This is due to the fact that there still exists dielectric material in between fibers (inhibiting them to contact) despite the compactness of the fibers are compacted (due to Poisson's effect). Nonetheless, it is undeniable that the Poisson's effect can potentially strengthen tunneling and lead to larger charge transfer through the adjacent fibers located into the loosened PDMS channels. Our results shown is Figure 5.5 reveal a more severe transition behavior at higher strain amplitudes, which is well in line with the results reported for other composite sensors; namely, for the case of PDMS/carbon black the transition effect has been reported at higher than 10% cyclic strain [121, 218, 219].

5.5 Summary of findings

Many different strain sensors been introduced in the literature by employing different materials systems and fabrication methods. For the applications where very low/high strains need to be captured, a high/low sensitivity is normally required, respectively. In this chapter, a low cost and simple fabrication process was followed to make highly sensitive strain sensors, mechanically compatible with the composite fabrics (i.e. causing minimal structural disturbance during health monitoring tests). Namely, a mixture of stretchable PDMS with CCFs was fabricated in form of the yarns, and piezoresistive assessments were conducted by simultaneous measurements of load, displacement, and resistance to ensure the sensor performance in the application of interest (monitoring local yarn strains in the composite fabrics during shear testing). The deformation mechanism which results in the resistance change was found to originate from the fiber/fiber reconfiguration when the PDMS matrix deforms under loading. This potentially involves fiber separation, compaction due to the Poisson's effect, creep in the polymer and the structural friction at the interface between fiber and polymer. The results suggested high sensitivity (gauge factor as high as 700) and high stretchability (as high as 25%) of the developed sensor, which would make it suitable for the study of sensitive deformations such as those in soft materials as dry woven fabrics.

Chapter 6: Sensor integrated picture frame test: Monitoring yarn tension

6.1 Overview

In the previous chapters it was shown that conventional picture frame test (PFT) is vulnerable to imperfections and can induce strains along the yarns rather than pure shearing. The range of induced strain was also calculated through analytical methods. A combination of PDMS/CCF sensor was found to be able to detect the strain ranges induced along the fabric yarns, while it is stretchable enough that when attached to the yarns and would not cause perturbations in the natural mechanical behavior of the fabric. Given the potential of the PDMS/CCF sensors in detecting strains at large deformation (Chapter 5), in this chapter, the improvements suggested through the modified version of picture frame test (namely the frameless picture frame test as discussed in Chapter 4) will be further assessed by attaching the sensors to the fabrics and subjecting the material system to different shear tests.

6.2 Attaching the sensors to the fabric

In order to monitor the relative displacement along a yarn during the PF tests and subsequently assess the analytical methods in Chapter 3, yarn-like sensors were fabricated and integrated within the mid yarn of the sample subjected to the shear test. Embedded mechanically compatible sensors should not affect the mechanical response of the fabrics and hence, stretchable piezoresistive sensors were made of stretchable polymers. For this purpose, following the procedure described in Chapter 5, carbon fibers supplied by ACP Composites Inc. (Livermore, CA) were chopped with non-uniform length distribution (between ~0.5-3mm) and soaked in acetone overnight to wash out the polymeric coatings on the carbon fibers and enhance their electrical conductivity. Polydimethylsiloxane (PDMS) base polymer (Sylgard 184 Silicone Elastomer) and its curing agent purchased from Sigma Aldrich Corp., USA were mixed with a 10:1 ratio. PDMS was then mechanically mix blended with the chopped carbon fibers in 3.5 wt.%. The mixture then was injected into a 1 mm thick, 3 mm width channel (formed by the gap between two glass slides) in which two carbon fiber electrodes were already embedded with a 20 mm distance (the length of the sensor). Carbon fiber electrodes were used due to their high mechanical compatibility and integration potential with fiberglass woven fabrics. The piezoresistive composite sensors were cured at 150 ˚C for 30 min and then peeled off. Integrating the sensors with the woven fabric was performed by locally gluing the carbon fiber yarn electrodes to the two ends of the mid yarn in the sample (attaching points close to the shear frame as seen in Figure 6.1(IV)) while a slight pre-tension was applied to the sensor for capturing compression strains in addition to the tensile deformations. During the tests, the electrical resistance change of the sensors was measured by a VersaSTAT4 Potentiostat (Gamble Technologies Ltd., Canada) under a 1 V applied DC voltage through the carbon fiber electrodes.

6.3 Sensor response to repeated loading in the conventional picture frame test

Forming and deformation of the composite glass fiber/epoxy woven fabrics heavily rely on the internal shearing of the yarns and hence, shearing characterization of these materials is a critical issue for design purposes [37, 220, 221] and analysis of their forming process [202]. Picture Frame (PF) test setup has widely been used to determine the shear characteristics of woven fabric composites [222]. However, the test imperfections (e.g. misalignment when mounting the sample, and fixture-related problems) [15, 223] cause the fabric to undergo inevitable tension/compression additional to shearing, the effect of which is usually exacerbated at high shear angles [195, 224]. To address these effects, CCF/PDMS sensors developed here were incorporated into the fabric next to the middle yarn in the PF setup to monitor the mechanical state of the yarns during the test; the loading was repeated for three times. As shown in Figure 6.1, the load required for applying shear deformation steadily increases at the beginning; while at high shear angles a rapid decrease in the load is observed due to the development of the wrinkles over the fabric. The resistance was found to increase from the beginning of the test to a maximum point, implying the existence of tension in the yarns which increases with the shear angle. Thereafter, especially for the first-loading, a decrease with a serrated profile was observed in the electrical resistance of the sensor, which continued while the wrinkles in the fabric started to develop. Since the sensor was not fully attached to/woven along with the yarns, the formation of wrinkles is expected to relax the sensor and hence to decrease the resistance. The resulting serrated profile in the response (as magnified in Figure 6.1(a)) can be basically attributed to the progressive slippage of the yarns into the clamps due to the present tensile loads. The results showed a more consistent force-displacement behavior when the loading was repeated in the second and third cycles (Figure 6.1(b)). The resistance peaks clearly elucidate the points at which an out-of-plane deformations occurred at shear angles of ~14˚.

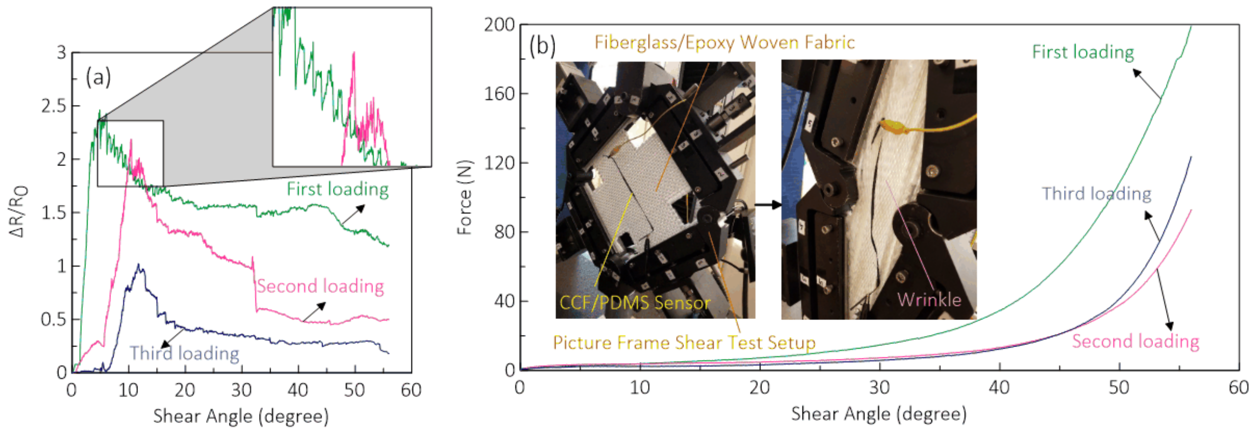

Figure 6.1. The change in the resistance of the CCF/PDMS sensors, integrated into the composite glass fiber/epoxy fabrics, during the picture frame test setup. (a) The change in the relative resistance as a function of shear angle, and (b) force-shear angle behavior of the glass fiber/epoxy fabrics in response to repeated loadings. Due to the imperfections (originated from sample preparation, mounting and clamping etc.), the yarns bear tension at the beginning of the tests up to a point where a compression/out-of-plane deformation relaxes the sensor.

6.4 Comparing local deformations in conventional versus frameless picture frame tests

Integrating sensor with the fabrics allows for locally monitoring the relative deformation of the yarns. The above-discussed test imperfections signify that the yarn tension/compression is a primary sign of non-ideal shear tests. In the current study, yarn axial deformation in the center region was monitored during fabric shearing by attaching a piezoresistive sensor with a slight pre-tensioning at the two ends of a fiber. Using sensors made of stretchable materials such as PDMS, one can ensure a minimal mechanical disturbance by the sensor on the characterization results.

The results of sensor resistance change with shear angle is illustrated for the picture frame based setup configurations in Figure 6.2, where the change in resistance is proportional to the strain induced in the yarns. In the conventional picture frame test, a sharp increase is seen during loading at the onset of the test. It can be explained by the yarn bending that is induced by the static friction at the beginning of the test. As it can be seen in Figure 6.2(d), the typical force-displacement behavior of woven fabrics starts with shear with static friction in which while the frame deforms, the yarns resist to deform at the cross-overs [15]. This leads to the yarn bending (see Figure 6.2(e)), the effect of which is reflected in the sensor's signal as an initial increase in resistance. At shear angles of ~5°, this resistance starts decreasing as a result of lessened tensile strains which can be attributed to the switch between static and kinetic friction forces at crossovers as discussed in [15]). Non-uniformity of fabric deformation in the frame, due to the combined imperfection parameters, can also be evidenced by the fluctuations of the sensor yarn's response over the shear test. A similar but much more consistent trend was observed in the resistance change-shear angle behavior in the FPF test. An initial increase in resistance is in accordance with the tension induced due to the yarn bending close to the arms followed by a decrease to a plateau due to the kinetic friction dominant behavior in the entire fabric [15]. In opposite, a slightly decreasing trend at the beginning of the test in the needle integrated FPF setup implies no tension along the yarns, which confirms the absence of yarn bending in this set-up. In essence, the sensor is slightly relaxed in this initial stage along with some signal fluctuations.

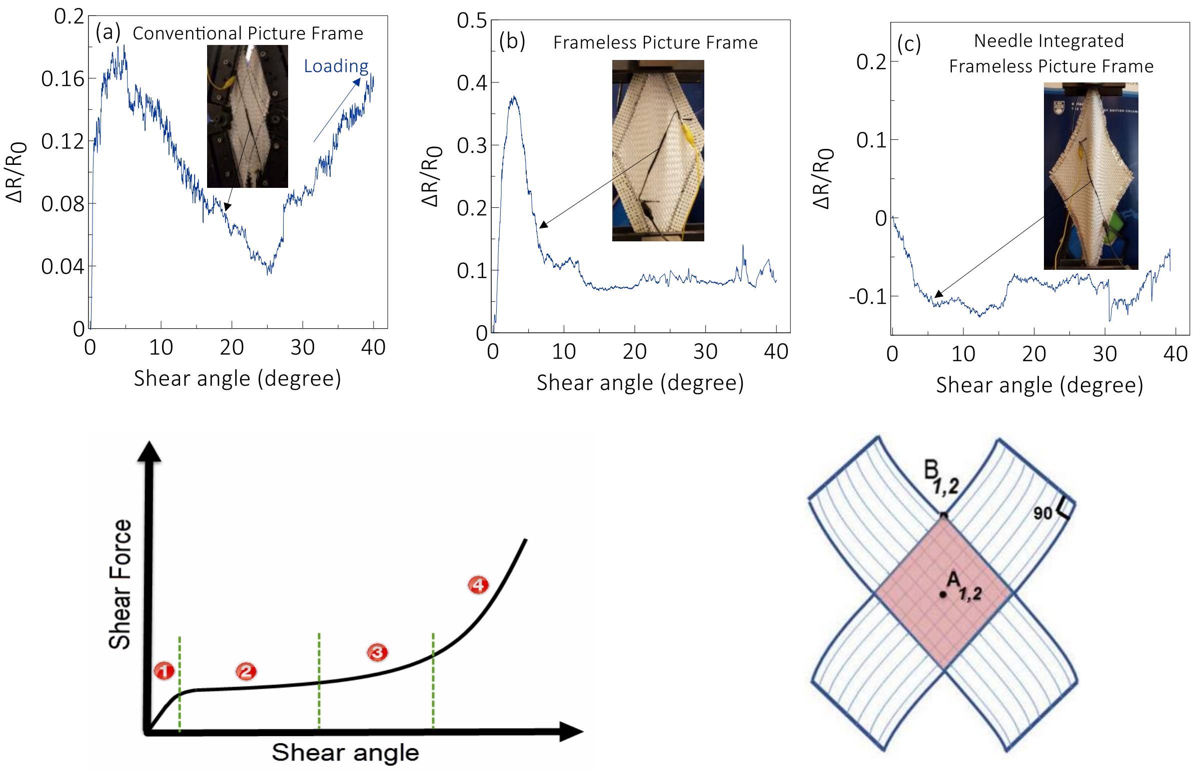

(d) (e)

Figure 6.2. The sensor signals measured during the tests for the new test setups. (a) Conventional picture frame, (b) frameless picture frame, and (c) needle integrated frameless picture frame tests. An initial increase in resistance in the picture frame and consolidated frame setups are indicative of yarn tension followed by a decreasing signal once out-of-plane deformation/wrinkling develops over the fabric. (d) a typical picture frame force-shear angle response of woven fabric at macro-level, showing four phases of deformation evolution [15]: 1- shear with static friction, 2- shear with dynamic friction, 3- locking, and 4- wrinkling; notice the correlation between these phases and those seen in the response of the sensor. (e) Mechanism of yarn bending during the shear with static friction [15].

6.5 Summary of findings

Taking advantage of the embedded strain sensors, in this chapter it was shown that the fabric shear test health monitoring can be verified experimentally at the local yarn level. Namely, the PDMS/CCF composite piezoresistive sensors were integrated within the fabric and subjected to shear loading following different shear testing scenarios. Sensor signals were captured while the shear deformation developed over the fabric samples. The recorded signals showed that the sensor can represent the local structural evolutions occurring due to the static friction and internal relative displacements due to the out of plane deformations in the fabric. The results also confirmed that the new needle integrated FPF test set-up could be very close to an ideal shear mode, as the sensor signals in this case did not show the initial yarn tensions (increase in resistance) as opposed to the case of conventional PF and un-needled frameless picture frame tests.

Chapter 7: Conclusions and future perspectives

7.1 Summary

The present study aimed to fabricate a mechanically-tailored stretchable strain sensor based on PDMS/CCF piezoresistive composites that could assist monitoring the test accuracy when shear characterization of woven fabrics. The sensors were tailored for integration with composite fabrics and served in order to ensure that the shear test results resulted by the woven fabrics can provide reliable understanding of the material behavior by monitoring the presence of test noise effects. In this regards, PDMS/CCF sensors were developed and the characterized in order to prove that they can be used for monitoring the shear test health in composite fabrics. It was basically achieved through the adequate stretchability (up to 25%) and high sensitivity (gauge factor as high as 700) obtained through the proposed material composition.

An analytical-experimental approach was implemented in the present work to gain better insight into the main sources of imperfections and their consequences in capturing shear response of woven fabrics using picture frame setups, based on which a novel testing procedure was introduced to mitigate/minimize those effects. The capability of the introduced "frameless picture frame" testing method along with its needle integrated version was evaluated in comparison with that of the conventional shear test methods, including the picture frame and the bias extension tests. It was discussed that a sign of the presence of the imperfection in the fabric shear tests can be the induced axial deformations along the yarns, as they lead to non-pure shearing modes in the fabric a typical PP/glass twill fabric to monitor such deformations during different shear tests.

It was highlighted that the application of sensors is not limited to the in-situ measurements for structural health monitoring (SHM) of large mechanical components, rather it can offer a great promise for laboratory-scale applications such as characterization of fabric composite materials. For instance, the deformation analysis of woven reinforcement fabrics under combined loading conditions has been proven to be difficult, if not impossible, due to the complex nature of their deformations. Integration of sensors into the woven fabrics can provide valuable information regarding the gradient of local shearing as well as local planar strain components in the woven fabric. Piezoresistive materials are the principal element of the currently used strain gauges as above-mentioned in SHM, but they are not free of drawbacks. In terms of electromechanical characterization, the time-dependent behavior of piezoresistive sensors (which is mainly originated from the viscoelastic behavior of the sensor material) has been the primary limitation of these materials. Furthermore, different electrical circuit configurations have hindered unique interpretations of piezoresistive-based sensors. More importantly, a substantial degradation of sensitivity (especially in the case of composite piezoresistive sensors comprising of flexible matrix materials) has put the repeatability of piezoresistive sensors under question. In fact, the electrical resistance in many cases significantly changes due to the fabrication process or embedment procedure itself, which is not desirable and can potentially alter the piezoresistive behavior. In order to ensure the acceptable performance and suitability of the fabricated PDMS/CCF sensor in this work, a full piezoresistive characterization of the sensor was implemented and then the sensor was applied to capture the local deformation in the woven fabrics subjected to different shear testing scenarios. The main findings of the work may be summarized as follows:

Fabricating and characterizing a highly sensitive yarn-like sensor for monitoring the fabric test imperfections:

- As for cyclic piezoresistivity, the CCF/PDMS sensors exhibited a linear resistance-strain behavior in the first cycle; the behavior became highly nonlinear but repeatable at the subsequent cycles wherein piezoresistivity altered from negative to positive in loading (and vice versa during unloading).
- The main deformation mechanisms from which the electromechanical response of the sensors is eventuated were as follows: (i) carbon fiber (CF) separation due to the axial deformation, (ii) buckling/shrinkage and de-buckling of the CFs into the CF carrier channels during the cyclic loading due to the CCF/PDMS interfacial friction, (iii) polymeric matrix creep and loosening of the channels due to the radial pressure applied by the CFs to the PDMS channel walls when the sensor is stretched multiple times, and (iv) transverse shrinkage of the material due to the Poisson's effect, thereby compressing the fibers and yielding more electrical contacts/pathways.

- The electromechanical properties of the CCF/PDMS sensors were tunable by the CCF content. Given a low percolation threshold of 1.41 wt. % due to the high specific surface area of CCFs fillers, lowering the CCF concentration (i) led to a higher mechanical flexibility, (ii) increased sensitivity especially during the first cycle of loading (GF up to ~700), (iii) reduced the piezoresistivity transition strain, and (iv) delayed the rupture. However, this expedited the electrical disconnection under loading and intensifies the electrical and mechanical relaxation, and thereby introduced more time-dependency of the sensor response.
- The piezoresistive properties of the CCF/PDMS sensor were found to be sensitive to loading configuration. Applying higher strain was observed to not only decay the piezoresistive performance (i.e. sensitivity) but also intensify the drop in the resistance amplitude (in the cyclic loading) and delays the piezoresistivity transition.

The study of imperfections of PFT and providing an alternative testing method as a solution to mitigate the test flaws:

- The current picture frame test (PFT) setup is vulnerable and sensitive to the imperfections that can originate from either the operator, fixture design, or the fabric itself.
- Depending on the state of fabric misplacement, the yarns in each direction can undergo increasing tension or compression during the test; while the shear angle discrepancies between the fabric and frame decreases with shear loading.
- Offset of the clamp edges from the ideal shear frame is a neglected source of imperfection in the current literature, while it can occur frequently (e.g. in the coupled tension-shear setups or via the fixture design tolerances). In particular, an inward clamping offset can imitate the typical fiber bending close to arms in the conventional picture frame tests and be responsible for faster locking in the arms than the central region, as well as tensile loads along the fibers. The outward offset, on the other hand, leads to compressive yarn strains and hence the likelihood of global wrinkles early in the test.
- Any mismatch between the fabric and frame shear angles brings tension to some yarns, especially when there are cut-offs in the picture frame sample. While this is highly

dependent on the sample size and possibly other discussed imperfections in Chapter 4, in the case of cross-samples with long arms, the center shear angle is lower than the frame angle, and hence the possibility of faster wrinkling in the arms.

- As opposed to the conventional PF test method, the proposed FPF test approach needs no fixture and is implemented with higher control over the fabric mounting, thereby minimizing the effect of imperfections. The test also indicated identical wrinkling behavior to that of the bias extension test, while showing only one/uniform region of deformation as opposed to the three regions (full share, half shear, and no shear) seen in the bias-extension test.
- The needle integrated FPF test provided enhanced shearing characterization capability due to: (i) resolved yarn bending issue at the sample boundaries, (ii) very notable reproducibility, (iii) minimized size effect dependency, (iv) more consistent load/unload behavior of the fabric.
- By far a higher normalized shear force in the conventional picture frame test was obtained compared to the bias extension test. This would suggest the formation of local yarn tensile forces in the picture frame test due to the imperfections.

Integrating the sensors with the fabrics for real-rime monitoring the strains along the yarns during shear tests

- Integrating the sensors with the fabrics subjected to shearing load showed the relative deformation between the two ends of a fiber yarn and could capture the axial deformations induced along the yarn.
- In the conventional picture frame setup, the sensors showed an increase in the signal which recovered at between ~5-14°. This increase in resistance occurred as a consequence of the combined effects of the imperfections identified in the previous sections. It also could be attributed to the static friction occurs at the very beginning of the deformation in force-shear angle behavior.
- The initial increase in resistance of the attached sensors was observed in the case of PFT and FPFT, but not in the needle integrated FPFT, which is indicative of the effect of

bending of the yarns when applying the shear load. The results of the sensor signals confirm that the new proposed test methods could more effectively reflect the pure shear properties of the composite fabrics.

7.2 Contribution to knowledge

- Fabricating a highly sensitive and stretchable piezoresistive sensor through a low cost and simple fabrication process.
- Better identifying and analytically ‘modeling’ unknown sources of imperfections in the conventional picture frame test, which had been mostly neglected in the past literature.
- Introducing a new shear testing method wherein the sources of uncertainties were mitigated and a more realistic ‘pure’ shear behavior of woven fabric could be gained.
- Proving the feasibility of shear test health monitoring by means of attaching the above sensors along the yarns of a fabric and correlating the sensor resistance change to the global fabric force measurements.

7.3 Future work

In terms of sensor development for test health monitoring, future work can also be sought to improve the piezoresistive sensor behavior and diminish transition effects of the CCF/PDMS composites; specially by optimizing its manufacturing parameters. For instance, a solvent blending approach (by dispersing the composite elements into a solvent before mixing) could enhance the polymer viscosity and consequently the dispersion quality and electrical conductivity of the ensuing sensor. The effects of contact resistance can be studied in the present study through the four-point configurations for a more accurate sensor characterization. Also, several methods are available to align the fibers into the matrix to potentially obtain higher sensitivity, more linear piezoresistive behavior, and lower percolation thresholds. Finally, a detailed sensitivity analysis can be conducted to explore the piezoresistivity mechanism by investigating the parameters such as the CF length, pre-conditioning, pre-tension/compression, and sample size effect. Sensors with the ability to capture biaxial sensors could be developed and attached to the fabrics e.g. for the biaxial tests to capture the strain components along two directions. Such a sensor could involve either a cross-shape or an asymmetric conductive network wherein one can find the strain in different directions.

This study may be further expanded by tailoring the FPF testing process for other types of fabrics. Locally applying adhesives (e.g. glue or a resin) can be useful to form the shearing frame on the fabric itself, in lieu of heating/consolidation as was applied here on a thermoplastic prepreg. One may also stitch the fabric through the boundary crossovers instead of manually putting needles in the needle integrated FPF test; which would result in even higher test repeatability and better confidence in capturing pure large shear deformation. Furthermore, the shear characterization results of this study may be used practically as the material model in finite element simulation and validated with experimental tests to evaluate the reliability of the presented testing approach.

Composite testing in the thesis has been solely characterized by attaching the sensors to the mid yarn. One can use an array of sensors attached to the fabric at different locations to provide information regarding the way the material deforms in different regions during testing. Attaching the sensor to the fabrics could impact the signals; hence, other methods than gluing at the cross-overs could be implemented to integrate the sensor to the fabric. Besides, the relative displacement between the two points across the wrinkle becomes smaller which can assist characterizing the strain at which wrinkling occurs. It is worth noting that the current sensors should be also characterized in terms of bending deformation if the wrinkling detection is of interest. The current approaches (such as optical methods) lack reliability as the deformations at the beginning of the wrinkling are very small. Different yarn-like sensors can be developed using methods such as dip coating, PDMS microtubes etc. These methods allow researchers to weave the sensors along with the yarns and make sure the sensors are fully laid along with the other yarns as well.

Bibliography

[1] Khedari J, Suttisonk B, Pratinthong N, Hirunlabh J. New lightweight composite construction materials with low thermal conductivity. Cement and Concrete Composites 2001;23:65-70.

[2] Wycech J. Method of manufacturing a lightweight composite automotive door beam. Google Patents; 1990.

[3] Duhovic M, Bhattacharyya D. Simulating the deformation mechanisms of knitted fabric composites. Composites Part A: Applied Science and Manufacturing 2006;37:1897-915.

[4] Alfano G, Crisfield MA. Finite element interface models for the delamination analysis of laminated composites: mechanical and computational issues. International journal for numerical methods in engineering 2001;50:1701-36.

[5] Wang P, Legrand X, Boisse P, Hamila N, Soulat D. Experimental and numerical analyses of manufacturing process of a composite square box part: Comparison between textile reinforcement forming and surface 3D weaving. Composites Part B: Engineering 2015;78:26-34.

[6] Boisse P, Wang P, Hamila N, Lemeur K, Rusanov A, Guzman E, et al. Bias Extension Test for In-Plane Shear Properties during Forming-Use at High Temperature and Limits of the Test. Key Engineering Materials: Trans Tech Publ; 2015. p. 369-74.

[7] Dangora LM, Hansen CJ, Mitchell CJ, Sherwood JA, Parker JC. Challenges associated with shear characterization of a cross-ply thermoplastic lamina using picture frame tests. Composites Part A: Applied Science and Manufacturing 2015;78:181-90.

[8] D'Alessandro A, Ubertini F, Materazzi AL, Laflamme S, Porfiri M. Electromechanical modelling of a new class of nanocomposite cement-based sensors for structural health monitoring. Structural Health Monitoring 2015;14:137-47.

[9] Liu L, Chen J, Li X, Sherwood J. Two-dimensional macro-mechanics shear models of woven fabrics. Composites Part A: Applied Science and Manufacturing 2005;36:105-14.

[10] Allaoui S, Boisse P, Chatel S, Hamila N, Hivet G, Soulat D, et al. Experimental and numerical analyses of textile reinforcement forming of a tetrahedral shape. Composites Part A: Applied Science and Manufacturing 2011;42:612-22.

[11] Harrison P, Gomes R, Curado-Correia N. Press forming a 0/90 cross-ply advanced thermoplastic composite using the double-dome benchmark geometry. Composites Part A: Applied Science and Manufacturing 2013;54:56-69.

[12] Gatouillat S, Bareggi A, Vidal-Sallé E, Boisse P. Meso modelling for composite preform shaping – Simulation of the loss of cohesion of the woven fibre network. Composites Part A: Applied Science and Manufacturing 2013;54:135-44.

[13] Guzman-Maldonado E, Hamila N, Naouar N, Moulin G, Boisse P. Simulation of thermoplastic prepreg thermoforming based on a visco-hyperelastic model and a thermal homogenization. Materials & Design 2016;93:431-42.

[14] Boisse P, Zouari B, Gasser A. A mesoscopic approach for the simulation of woven fibre composite forming. Composites Science and Technology 2005;65:429-36.

[15] Haghi Kashani M, Hosseini A, Sassani F, Ko F, Milani A. The Role of Intra-Yarn Shear in Integrated Multi-Scale Deformation Analyses of Woven Fabrics: A Critical Review. Critical Reviews in Solid State and Materials Sciences 2017:1-20.

[16] Jauffrès D, Sherwood JA, Morris CD, Chen J. Discrete mesoscopic modeling for the simulation of woven-fabric reinforcement forming. International Journal of Material Forming 2009;3:1205-16.

[17] Erol O, Powers B, Keefe M. Development of a non-orthogonal macroscale material model for advanced woven fabrics based on mesoscale structure. Composites Part B: Engineering 2017;110:497-510.

[18] Boisse P, Hamila N, Vidal-Sallé E, Dumont F. Simulation of wrinkling during textile composite reinforcement forming. Influence of tensile, in-plane shear and bending stiffnesses. Composites Science and Technology 2011;71:683-92.

[19] Pazmino J, Mathieu S, Carvelli V, Boisse P, Lomov SV. Numerical modelling of forming of a non-crimp 3D orthogonal weave E-glass composite reinforcement. Composites Part A: Applied Science and Manufacturing 2015;72:207-18.

[20] Peng X, Ding F. Validation of a non-orthogonal constitutive model for woven composite fabrics via hemispherical stamping simulation. Composites Part A: Applied Science and Manufacturing 2011;42:400-7.

[21] Guzman-Maldonado E, Hamila N, Boisse P, Bikard J. Thermomechanical analysis, modelling and simulation of the forming of pre-impregnated thermoplastics composites. Composites Part A: Applied Science and Manufacturing 2015;78:211-22.

[22] Cao J, Akkerman R, Boisse P, Chen J, Cheng HS, de Graaf EF, et al. Characterization of mechanical behavior of woven fabrics: Experimental methods and benchmark results. Composites Part A: Applied Science and Manufacturing 2008;39:1037-53.

[23] Sharma SB, Sutcliffe MPF, Chang SH. Characterisation of material properties for draping of dry woven composite material. Composites Part A: Applied Science and Manufacturing 2003;34:1167-75.

[24] Hamila N, Boisse P. Locking in simulation of composite reinforcement deformations. Analysis and treatment. Composites Part A: Applied Science and Manufacturing 2013;53:109-17.

[25] Barbagallo G, Madeo A, Azehaf I, Giorgio I, Morestin F, Boisse P. Bias extension test on an unbalanced woven composite reinforcement: Experiments and modeling via a second-gradient continuum approach. Journal of Composite Materials 2016;51:153-70.

[26] Boisse P, Hamila N, Guzman-Maldonado E, Madeo A, Hivet G, dell'Isola F. The bias-extension test for the analysis of in-plane shear properties of textile composite reinforcements and prepregs: a review. International Journal of Material Forming 2016;10:473-92.

[27] Parsons EM, King MJ, Socrate S. Modeling yarn slip in woven fabric at the continuum level: Simulations of ballistic impact. Journal of the Mechanics and Physics of Solids 2013;61:265-92.

[28] Zhang D, Chen L, Wang Y, Sun Y, Jia N, Qian K. Bias tensile strength behaviors of woven fabric: theoretical and experimental. The Journal of The Textile Institute 2017;108:1753-61.

[29] Boisse P, Hamila N, Guzman-Maldonado E, Madeo A, Hivet G, Dell'Isola F. The bias-extension test for the analysis of in-plane shear properties of textile composite reinforcements and prepregs: a review. International Journal of Material Forming 2017;10:473-92.

[30] Chen Q, Boisse P, Park CH, Saouab A, Bréard J. Intra/inter-ply shear behaviors of continuous fiber reinforced thermoplastic composites in thermoforming processes. Composite Structures 2011;93:1692-703.

[31] Harrison P, Clifford MJ, Long AC. Shear characterisation of viscous woven textile composites: a comparison between picture frame and bias extension experiments. Composites Science and Technology 2004;64:1453-65.

[32] Lomov SV, Barburski M, Stoilova T, Verpoest I, Akkerman R, Loendersloot R, et al. Carbon composites based on multiaxial multiply stitched preforms. Part 3: Biaxial tension, picture frame and compression tests of the preforms. Composites Part A: Applied Science and Manufacturing 2005;36:1188-206.

[33] Willems A, Lomov SV, Verpoest I, Vandepitte D. Optical strain fields in shear and tensile testing of textile reinforcements. Composites Science and Technology 2008;68:807-19.

[34] Carvelli V, Pazmino J, Lomov SV, Verpoest I. Deformability of a non-crimp 3D orthogonal weave E-glass composite reinforcement. Composites Science and Technology 2012;73:9-18.

[35] Mohan RP, Alshahrani H, Hojjati M. Investigation of intra-ply shear behavior of out-of-autoclave carbon/epoxy prepreg. Journal of Composite Materials 2016;50:4251-68.

[36] Azhari F, Banthia N. Cement-based sensors with carbon fibers and carbon nanotubes for piezoresistive sensing. Cement and Concrete Composites 2012;34:866-73.

[37] Nosrat-Nezami F, Gereke T, Eberdt C, Cherif C. Characterisation of the shear–tension coupling of carbon-fibre fabric under controlled membrane tensions for precise simulative predictions of industrial preforming processes. Composites Part A: Applied Science and Manufacturing 2014;67:131-9.

[38] Lebrun G, Bureau MN, Denault J. Evaluation of bias-extension and picture-frame test methods for the measurement of intraply shear properties of PP/glass commingled fabrics. Composite Structures 2003;61:341-52.

[39] Komeili M, Milani AS. Shear response of woven fabric composites under meso-level uncertainties. Journal of Composite Materials 2012;47:2331-41.

[40] Mitchell C, Dangora L, Bielmeier C, Sherwood J. Investigation into the changes in bending stiffness of a textile reinforced composite due to in-plane fabric shear: Part 1 – Experiment. Composites Part A: Applied Science and Manufacturing 2016;85:94-102.

[41] Zhu B, Yu T, Tao X. An experimental study of in-plane large shear deformation of woven fabric composite. Composites Science and Technology 2007;67:252-61.

[42] Colman AG, Bridgens BN, Gosling PD, Jou GT, Hsu XY. Shear behaviour of architectural fabrics subjected to biaxial tensile loads. Composites Part A: Applied Science and Manufacturing 2014;66:163-74.

[43] Lomov SV, Boisse P, Deluycker E, Morestin F, Vanclooster K, Vandepitte D, et al. Full-field strain measurements in textile deformability studies. Composites Part A: Applied Science and Manufacturing 2008;39:1232-44.

[44] Lussier D. Shear characterization of textile composite formability. 2002.

[45] Na W, Ahn H, Han S, Harrison P, Park JK, Jeong E, et al. Shear behavior of a shear thickening fluid-impregnated aramid fabrics at high shear rate. Composites Part B: Engineering 2016;97:162-75.

[46] Li L, Zhao Y, Vuong H-g-n, Chen Y, Yang J, Duan Y. In-plane shear investigation of biaxial carbon non-crimp fabrics with experimental tests and finite element modeling. Materials & Design 2014;63:757-65.

[47] El-Sabbagh A, Taha I. Characterization of the draping behavior of jute woven fabrics for applications of natural-fiber/epoxy composites. Journal of Applied Polymer Science 2013;130:1453-65.

[48] Döbrich O, Gereke T, Cherif C. A Finite Element Based Approach for the Accurate Determination of the Shear Behaviour of Textiles with the Picture-Frame Shear Test. Key Engineering Materials 2013;554-557:1105-15.

[49] Dangora LM, Hansen CJ, Mitchell CJ, Sherwood JA, Parker JC. Challenges associated with shear characterization of a cross-ply thermoplastic lamina using picture frame tests. Composites Part A: Applied Science and Manufacturing 2015;78:181-90.

[50] Milani AS, Nemes JA, Lebrun G, Bureau MN. A comparative analysis of a modified picture frame test for characterization of woven fabrics. Polymer Composites 2009:NA-NA.

[51] Hübner M, Rocher JE, Allaoui S, Hivet G, Gereke T, Cherif C. Simulation-based investigations on the drape behavior of 3D woven fabrics made of commingled yarns. International Journal of Material Forming 2015;9:591-9.

[52] Zhou G, Zhao Y, Guo F, Xu W. A smart high accuracy silicon piezoresistive pressure sensor temperature compensation system. Sensors 2014;14:12174-90.

[53] Wu G, Xu D, Xiong B, Wang Y. Wheatstone bridge piezoresistive sensing for bulk-mode micromechanical resonator. Applied Physics Letters 2012;101:193505.

[54] Adams TM, Layton RA. Introductory MEMS: fabrication and applications: Springer Science & Business Media; 2009.

[55] Doll JC, Pruitt BL. Piezoresistor design and applications: Springer; 2013.

[56] Cole DP, Henry TC, Gardea F, Haynes RA. Interphase mechanical behavior of carbon fiber reinforced polymer exposed to cyclic loading. Composites Science and Technology 2017;151:202-10.

[57] Yao X, Luan C, Zhang D, Lan L, Fu J. Evaluation of carbon fiber-embedded 3D printed structures for strengthening and structural-health monitoring. Materials & Design 2017;114:424-32.

[58] Ferreira RTL, Amatte IC, Dutra TA, Bürger D. Experimental characterization and micrography of 3D printed PLA and PLA reinforced with short carbon fibers. Composites Part B: Engineering 2017;124:88-100.

[59] Azhari F, Banthia N. Carbon Fiber-Reinforced Cementitious Composites for Tensile Strain Sensing. ACI Materials Journal 2017;114.

[60] Lambiase F, Ko D-C. Two-steps clinching of aluminum and Carbon Fiber Reinforced Polymer sheets. Composite Structures 2017;164:180-8.

[61] D'Alessandro A, Rallini M, Ubertini F, Materazzi AL, Kenny JM. Investigations on scalable fabrication procedures for self-sensing carbon nanotube cement-matrix composites for SHM applications. Cement and Concrete Composites 2016;65:200-13.

[62] Chung DDL. Processing-structure-property relationships of continuous carbon fiber polymer-matrix composites. Materials Science and Engineering: R: Reports 2017;113:1-29.

[63] Wang X, Fu X, Chung D. Strain sensing using carbon fiber. Journal of Materials Research 1999;14:790-802.

[64] Kalashnyk N, Faulques E, Schjødt-Thomsen J, Jensen LR, Rauhe JCM, Pyrz R. Strain sensing in single carbon fiber epoxy composites by simultaneous in-situ Raman and piezoresistance measurements. Carbon 2016;109:124-30.

[65] Yao X, Luan C, Zhang D, Lan L, Fu J. Evaluation of carbon fiber-embedded 3D printed structures for strengthening and structural-health monitoring. Materials & Design 2017;114:424-32.

[66] Baeza FJ, Galao O, Zornoza E, Garcés P. Effect of aspect ratio on strain sensing capacity of carbon fiber reinforced cement composites. Materials & Design 2013;51:1085-94.

[67] Payakaniti P, Pinitsoontorn S, Thongbai P, Amornkitbamrung V, Chindaprasirt P. Electrical conductivity and compressive strength of carbon fiber reinforced fly ash geopolymeric composites. Construction and Building Materials 2017;135:164-76.

[68] Goldfeld Y, Ben-Aarosh S, Rabinovitch O, Quadflieg T, Gries T. Integrated self-monitoring of carbon based textile reinforced concrete beams under repeated loading in the un-cracked region. Carbon 2016;98:238-49.

[69] Wang D, Chung D. Through-thickness piezoresistivity in a carbon fiber polymer-matrix structural composite for electrical-resistance-based through-thickness strain sensing. Carbon 2013;60:129-38.

[70] Chava S, Choudhary S, Namilae S. Delamination Detection in Carbon Fiber Composites using Piezoresistive Nanocomposites. 58th AIAA/ASCE/AHS/ASC Structures, Structural Dynamics, and Materials Conference2017. p. 1298.

[71] Kalashnyk N, Faulques E, Schjødt-Thomsen J, Jensen LR, Rauhe JCM, Pyrz R. Monitoring self-sensing damage of multiple carbon fiber composites using piezoresistivity. Synthetic Metals 2017;224:56-62.

[72] Kwon D-J, Shin P-S, Kim J-H, Wang Z-J, DeVries KL, Park J-M. Detection of damage in cylindrical parts of carbon fiber/epoxy composites using electrical resistance (ER) measurements. Composites Part B: Engineering 2016;99:528-32.

[73] Wen J, Xia Z, Choy F. Damage detection of carbon fiber reinforced polymer composites via electrical resistance measurement. Composites Part B: Engineering 2011;42:77-86.

[74] Salvado R, Lopes C, Szojda L, Araújo P, Gorski M, Velez FJ, et al. Carbon fiber epoxy composites for both strengthening and health monitoring of structures. Sensors 2015;15:10753-70.

[75] Matsuzaki R, Yamamoto K, Todoroki A. Crack swarm inspection for estimation of crack location in carbon fiber reinforced plastics: A numerical study. Composite Structures 2017;160:36-42.

[76] Saifeldeen MA, Fouad N, Huang H, Wu Z. Advancement of long-gauge carbon fiber line sensors for strain measurements in structures. Journal of Intelligent Material Systems and Structures 2016:1045389X16665974.

[77] Yang CQ, Wang XL, Jiao YJ, Ding YL, Zhang YF, Wu ZS. Linear strain sensing performance of continuous high strength carbon fibre reinforced polymer composites. Composites Part B: Engineering 2016;102:86-93.

[78] Fouad N, Saifeldeen M, Huang H, Wu Z. Development of Long-gauge Carbon Fiber Stain Sensors for Structural Health Monitoring.

[79] Johnson TM, Fullwood DT, Hansen G. Strain monitoring of carbon fiber composite via embedded nickel nano-particles. Composites Part B: Engineering 2012;43:1155-63.

[80] Ramirez M, Chung DDL. Electromechanical, self-sensing and viscoelastic behavior of carbon fiber tows. Carbon 2016;110:8-16.

[81] Yan Y, Sencadas V, Zhang J, Zu G, Wei D, Jiang Z. Processing, characterisation and electromechanical behaviour of elastomeric multiwall carbon nanotubes-poly (glycerol sebacate)

nanocomposites for piezoresistive sensors applications. Composites Science and Technology 2017;142:163-70.

[82] Wang L, Ma F, Shi Q, Liu H, Wang X. Study on compressive resistance creep and recovery of flexible pressure sensitive material based on carbon black filled silicone rubber composite. Sensors and Actuators A: Physical 2011;165:207-15.

[83] Zheng H, Zhu S, Li Z. Continuous deformation monitoring by polymer-matrix carbon fiber sensitive layer. Journal of Wuhan University of Technology-Mater Sci Ed 2016;31:705-12.

[84] Kang I, Heung YY, Kim JH, Lee JW, Gollapudi R, Subramaniam S, et al. Introduction to carbon nanotube and nanofiber smart materials. Composites Part B: Engineering 2006;37:382-94.

[85] Zhou Y, Zhou Y, Deng H, Fu Q. A novel route towards tunable piezoresistive behavior in conductive polymer composites: Addition of insulating filler with different size and surface characteristics. Composites Part A: Applied Science and Manufacturing 2017;96:99-109.

[86] Zhang B, Li B, Jiang S. Noncovalently functionalized multi-walled carbon nanotube with core-dualshell nanostructure for improved piezoresistive sensitivity of poly(dimethyl siloxane) nanocomposites. Composites Part A: Applied Science and Manufacturing 2017;94:124-32.

[87] Luo C, Liu N, Zhang H, Liu W, Yue Y, Wang S, et al. A new approach for ultrahigh-performance piezoresistive sensor based on wrinkled PPy film with electrospun PVA nanowires as spacer. Nano Energy 2017;41:527-34.

[88] Sanli A, Benchirouf A, Müller C, Kanoun O. Piezoresistive performance characterization of strain sensitive multi-walled carbon nanotube-epoxy nanocomposites. Sensors and Actuators A: Physical 2017;254:61-8.

[89] Coiai S, Passaglia E, Pucci A, Ruggeri G. Nanocomposites based on thermoplastic polymers and functional nanofiller for sensor applications. Materials 2015;8:3377-427.

[90] Hou Y, Wang D, Zhang X-M, Zhao H, Zha J-W, Dang Z-M. Positive piezoresistive behavior of electrically conductive alkyl-functionalized graphene/polydimethylsilicone nanocomposites. Journal of Materials Chemistry C 2013;1:515-21.

[91] Wu H, Qi Y, Wang Z, Zhao W, Li X, Qian L. Low percolation threshold in flexible graphene/acrylic polyurethane composites with tunable negative permittivity. Composites Science and Technology 2017;151:79-84.

[92] Yang L, Wang R, Song Q, Liu Y, Zhao Q, Shen Y. One-pot preparation of porous piezoresistive sensor with high strain sensitivity via emulsion-templated polymerization. Composites Part A: Applied Science and Manufacturing 2017;101:195-8.

[93] Makireddi S, Shivaprasad S, Kosuri G, Varghese FV, Balasubramaniam K. Electro-elastic and piezoresistive behavior of flexible MWCNT/PMMA nanocomposite films prepared by solvent casting method for structural health monitoring applications. Composites Science and Technology 2015;118:101-7.

[94] Ryu S, Lee P, Chou JB, Xu R, Zhao R, Hart AJ, et al. Extremely elastic wearable carbon nanotube fiber strain sensor for monitoring of human motion. ACS nano 2015;9:5929-36.

[95] DeGraff J, Liang R, Le MQ, Capsal J-F, Ganet F, Cottinet P-J. Printable low-cost and flexible carbon nanotube buckypaper motion sensors. Materials & Design 2017;133:47-53.

[96] Li S, Park JG, Wang S, Liang R, Zhang C, Wang B. Working mechanisms of strain sensors utilizing aligned carbon nanotube network and aerosol jet printed electrodes. Carbon 2014;73:303-9.

[97] Aly K, Li A, Bradford PD. Strain sensing in composites using aligned carbon nanotube sheets embedded in the interlaminar region. Composites Part A: Applied Science and Manufacturing 2016;90:536-48.

[98] Yan Y, Sencadas V, Zhang J, Zu G, Wei D, Jiang Z. Processing, characterisation and electromechanical behaviour of elastomeric multiwall carbon nanotubes-poly (glycerol sebacate)

nanocomposites for piezoresistive sensors applications. Composites Science and Technology 2017;142:163-70.

[99] Lozano-Pérez C, Cauich-Rodríguez JV, Avilés F. Influence of rigid segment and carbon nanotube concentration on the cyclic piezoresistive and hysteretic behavior of multiwall carbon nanotube/segmented polyurethane composites. Composites Science and Technology 2016;128:25-32.

[100] Lozano-Pérez C, Cauich-Rodríguez JV, Avilés F. Influence of rigid segment content on the piezoresistive behavior of multiwall carbon nanotube/segmented polyurethane composites. Journal of Applied Polymer Science 2017;134:n/a-n/a.

[101] Zheng Y, Li Y, Li Z, Wang Y, Dai K, Zheng G, et al. The effect of filler dimensionality on the electromechanical performance of polydimethylsiloxane based conductive nanocomposites for flexible strain sensors. Composites Science and Technology 2017;139:64-73.

[102] Fan Q, Qin Z, Gao S, Wu Y, Pionteck J, Mäder E, et al. The use of a carbon nanotube layer on a polyurethane multifilament substrate for monitoring strains as large as 400%. Carbon 2012;50:4085-92.

[103] Wang Y, Mi H, Zheng Q, Zhang H, Ma Z, Gong S. Highly stretchable and sensitive piezoresistive carbon nanotube/elastomeric triisocyanate-crosslinked polytetrahydrofuran nanocomposites. Journal of Materials Chemistry C 2016;4:460-7.

[104] Ferreira A, Lanceros-Mendez S. Piezoresistive response of spray-printed carbon nanotube/poly(vinylidene fluoride) composites. Composites Part B: Engineering 2016;96:242-7.

[105] Luo S, Liu T. Structure–property–processing relationships of single-wall carbon nanotube thin film piezoresistive sensors. Carbon 2013;59:315-24.

[106] Liu H, Li Y, Dai K, Zheng G, Liu C, Shen C, et al. Electrically conductive thermoplastic elastomer nanocomposites at ultralow graphene loading levels for strain sensor applications. Journal of Materials Chemistry C 2016;4:157-66.

[107] Li X, Huang W, Yao G, Gao M, Wei X, Liu Z, et al. Highly sensitive flexible tactile sensors based on microstructured multiwall carbon nanotube arrays. Scripta Materialia 2017;129:61-4.

[108] Wang X, Sparkman J, Gou J. Strain sensing of printed carbon nanotube sensors on polyurethane substrate with spray deposition modeling. Composites Communications 2017;3:1-6.

[109] Liu H, 刘虎, Huang W, 黄文举, Gao J, 高嘉辰, et al. Piezoresistive behavior of porous carbon nanotube-thermoplastic polyurethane conductive nanocomposites with ultrahigh compressibility. Applied Physics Letters 2016;108:011904.

[110] Oliva-Avilés AI, Avilés F, Sosa V. Electrical and piezoresistive properties of multi-walled carbon nanotube/polymer composite films aligned by an electric field. Carbon 2011;49:2989-97.

[111] Goh PS, Ismail AF, Ng BC. Directional alignment of carbon nanotubes in polymer matrices: Contemporary approaches and future advances. Composites Part A: Applied Science and Manufacturing 2014;56:103-26.

[112] Sharma A, Tripathi B, Vijay Y. Dramatic improvement in properties of magnetically aligned CNT/polymer nanocomposites. Journal of Membrane Science 2010;361:89-95.

[113] Cheng Q, Wang J, Jiang K, Li Q, Fan S. Fabrication and properties of aligned multiwalled carbon nanotube-reinforced epoxy composites. Journal of Materials Research 2008;23:2975-83.

[114] Cooper CA, Ravich D, Lips D, Mayer J, Wagner HD. Distribution and alignment of carbon nanotubes and nanofibrils in a polymer matrix. Composites science and technology 2002;62:1105-12.

[115] Li W, Wang Q, Dai J. Anisotropic properties of aligned SWNT modified poly (methyl methacrylate) nanocomposites. Bulletin of Materials Science 2006;29:313-6.

[116] Jung YJ, Kar S, Talapatra S, Soldano C, Viswanathan G, Li X, et al. Aligned carbon nanotube− polymer hybrid architectures for diverse flexible electronic applications. Nano letters 2006;6:413-8.

[117] Liu H, Dong M, Huang W, Gao J, Dai K, Guo J, et al. Lightweight conductive graphene/thermoplastic polyurethane foams with ultrahigh compressibility for piezoresistive sensing. Journal of Materials Chemistry C 2017;5:73-83.

[118] Gonçalves BF, Oliveira J, Costa P, Correia V, Martins P, Botelho G, et al. Development of water-based printable piezoresistive sensors for large strain applications. Composites Part B: Engineering 2017;112:344-52.

[119] Zhai T, Li D, Fei G, Xia H. Piezoresistive and compression resistance relaxation behavior of water blown carbon nanotube/polyurethane composite foam. Composites Part A: Applied Science and Manufacturing 2015;72:108-14.

[120] Souri H, Nam I, Lee H. Electrical properties and piezoresistive evaluation of polyurethane-based composites with carbon nano-materials. Composites Science and Technology 2015;121:41-8.

[121] Kalanadhabhatla SK. Piezoresistivity Behavior of Polydimethylsiloxane Based Conducting Composites for Printing on Textiles: North Carolina State University; 2012.

[122] Toprakci HA, Kalanadhabhatla SK, Spontak RJ, Ghosh TK. Polymer Nanocomposites Containing Carbon Nanofibers as Soft Printable Sensors Exhibiting Strain-Reversible Piezoresistivity. Advanced Functional Materials 2013;23:5536-42.

[123] Hong J, Pan Z, ZheWang, Yao M, Chen J, Zhang Y. A large-strain weft-knitted sensor fabricated by conductive UHMWPE/PANI composite yarns. Sensors and Actuators A: Physical 2016;238:307-16.

[124] Vidhate S, Chung J, Vaidyanathan V, D'souza NA. Resistive-conductive transitions in the time-dependent piezoresponse of PVDF-MWCNT nanocomposites. Polymer journal 2010;42:567.

[125] Tamburrano A, Sarasini F, De Bellis G, D’Aloia A, Sarto MS. The piezoresistive effect in graphene-based polymeric composites. Nanotechnology 2013;24:465702.

[126] Atif R, Shyha I, Inam F. Mechanical, Thermal, and Electrical Properties of Graphene-Epoxy Nanocomposites—A Review. Polymers 2016;8:281.

[127] Yan C, Wang J, Kang W, Cui M, Wang X, Foo CY, et al. Highly stretchable piezoresistive graphene–nanocellulose nanopaper for strain sensors. Advanced materials 2014;26:2022-7.

[128] Wang Y, Yang R, Shi Z, Zhang L, Shi D, Wang E, et al. Super-elastic graphene ripples for flexible strain sensors. ACS nano 2011;5:3645-50.

[129] Qiu L, Bulut Coskun M, Tang Y, Liu JZ, Alan T, Ding J, et al. Ultrafast Dynamic Piezoresistive Response of Graphene-Based Cellular Elastomers. Advanced Materials 2016;28:194-200.

[130] Xu R, Lu Y, Jiang C, Chen J, Mao P, Gao G, et al. Facile fabrication of three-dimensional graphene foam/poly (dimethylsiloxane) composites and their potential application as strain sensor. ACS applied materials & interfaces 2014;6:13455-60.

[131] Luo N, Huang Y, Liu J, Chen SC, Wong CP, Zhao N. Hollow-Structured Graphene–Silicone-Composite-Based Piezoresistive Sensors: Decoupled Property Tuning and Bending Reliability. Advanced materials 2017.

[132] Wang Y, Wang L, Yang T, Li X, Zang X, Zhu M, et al. Wearable and highly sensitive graphene strain sensors for human motion monitoring. Advanced Functional Materials 2014;24:4666-70.

[133] Tung TT, Karunagaran R, Tran DN, Gao B, Nag-Chowdhury S, Pillin I, et al. Engineering of graphene/epoxy nanocomposites with improved distribution of graphene nanosheets for advanced piezo-resistive mechanical sensing. Journal of Materials Chemistry C 2016;4:3422-30.

[134] Park JJ, Hyun WJ, Mun SC, Park YT, Park OO. Highly stretchable and wearable graphene strain sensors with controllable sensitivity for human motion monitoring. ACS applied materials & interfaces 2015;7:6317-24.

[135] Tung TT, Robert C, Castro M, Feller JF, Kim TY, Suh KS. Enhancing the sensitivity of graphene/polyurethane nanocomposite flexible piezo-resistive pressure sensors with magnetite nano-spacers. Carbon 2016;108:450-60.

[136] Wei Y, Chen S, Dong X, Lin Y, Liu L. Flexible piezoresistive sensors based on "dynamic bridging effect" of silver nanowires toward graphene. Carbon 2017;113:395-403.

[137] Zha JW, Huang W, Wang SJ, Zhang DL, Li RK, Dang ZM. Difunctional Graphene–Fe3O4 Hybrid Nanosheet/Polydimethylsiloxane Nanocomposites with High Positive Piezoresistive and Superparamagnetism Properties as Flexible Touch Sensors. Advanced Materials Interfaces 2016;3.

[138] Yin H, Peng X, Du T, Guo Z. Draping of plain woven carbon fabrics over a double-curvature mold. Composites Science and Technology 2014;92:64-9.

[139] Zhang H, Bilotti E, Peijs T. The use of carbon nanotubes for damage sensing and structural health monitoring in laminated composites: a review. Nanocomposites 2015;1:167-84.

[140] Weck D, Sauer S, Adam F, Starke E, Böhm R, Modler N. Embedded Sensor Networks for Textile-Reinforced Thermoplastics: Sensor Network Design and Mechanical Composite Performance. Advanced Engineering Materials 2016;18:444-51.

[141] Schaaf K, Cook B, Ghezzo F, Starr A, Nemat-Nasser S. Mechanical properties of composite materials with integrated embedded sensor networks. Smart structures and materials: International Society for Optics and Photonics; 2005. p. 781-5.

[142] Konka HP, Wahab MA, Lian K. Piezoelectric fiber composite transducers for health monitoring in composite structures. Sensors and Actuators A: Physical 2013;194:84-94.

[143] Boukabache H, Escriba C, Fourniols J-Y. Toward smart aerospace structures: Design of a piezoelectric sensor and its analog interface for flaw detection. Sensors 2014;14:20543-61.

[144] Müller M, Müller B, Hensel S, Nestler M, Jahn SF, Müller R, et al. Structural integration of piezoceramic fibers in deep drawn sheet metal for material-integrated health monitoring. Mechatronics 2016;34:100-10.

[145] Dziendzikowski M, Kurnyta A, Dragan K, Klysz S, Leski A. In situ Barely Visible Impact Damage detection and localization for composite structures using surface mounted and embedded PZT transducers: A comparative study. Mechanical Systems and Signal Processing 2016;78:91-106.

[146] Baptista FG, Budoya DE, de Almeida VA, Ulson JAC. An experimental study on the effect of temperature on piezoelectric sensors for impedance-based structural health monitoring. Sensors 2014;14:1208-27.

[147] Zou D, Liu T, Liang C, Huang Y, Zhang F, Du C. An experimental investigation on the health monitoring of concrete structures using piezoelectric transducers at various environmental temperatures. Journal of Intelligent Material Systems and Structures 2015;26:1028-34.

[148] Sun S, Han B, Jiang S, Yu X, Wang Y, Li H, et al. Nano graphite platelets-enabled piezoresistive cementitious composites for structural health monitoring. Construction and Building Materials 2017;136:314-28.

[149] Han B, Yu X, Kwon E. A self-sensing carbon nanotube/cement composite for traffic monitoring. Nanotechnology 2009;20:445501.

[150] Konsta-Gdoutos MS, Aza CA. Self sensing carbon nanotube (CNT) and nanofiber (CNF) cementitious composites for real time damage assessment in smart structures. Cement and Concrete Composites 2014;53:162-9.

[151] D'Alessandro A, Ubertini F, Laflamme S, Rallini M, Materazzi AL, Kenny JM. Strain sensitivity of carbon nanotube cement-based composites for structural health monitoring. SPIE Smart Structures and Materials+ Nondestructive Evaluation and Health Monitoring: International Society for Optics and Photonics; 2016. p. 980319--8.

[152] Aly K, Li A, Bradford PD. Compressive piezoresistive behavior of carbon nanotube sheets embedded in woven glass fiber reinforced composites. Composites Part B: Engineering 2017;116:459-70.

[153] Picot OT, Rocha VG, Ferraro C, Ni N, D'elia E, Meille S, et al. Using graphene networks to build bioinspired self-monitoring ceramics. Nature Communications 2017;8.

[154] Ali MA, Umer R, Khan KA, Samad YA, Liao K, Cantwell W. Graphene coated piezo-resistive fabrics for liquid composite molding process monitoring. Composites Science and Technology 2017.

[155] Jerkovic I, Koncar V, Grancaric AM. New Textile Sensors for In Situ Structural Health Monitoring of Textile Reinforced Thermoplastic Composites Based on the Conductive Poly (3, 4-ethylenedioxythiophene)-poly (styrenesulfonate) Polymer Complex. Sensors 2017;17:2297.

[156] Balaji R, Sasikumar M. A nanometallic nickel-coated, glass-fibre-based structural health monitoring system for polymer composites. Smart Materials and Structures 2017;26.

[157] Moriche R, Jiménez-Suárez A, Sánchez M, Prolongo SG, Ureña A. Graphene nanoplatelets coated glass fibre fabrics as strain sensors. Composites Science and Technology 2017;146:59-64.

[158] He D, Fan B, Zhao H, Lu X, Yang M, Liu Y, et al. Design of Electrically Conductive Structural Composites by Modulating Aligned CVD-Grown Carbon Nanotube Length on Glass Fibers. ACS applied materials & interfaces 2017;9:2948-58.

[159] Luo S, Liu T. Graphite nanoplatelet enabled embeddable fiber sensor for in situ curing monitoring and structural health monitoring of polymeric composites. ACS applied materials & interfaces 2014;6:9314-20.

[160] Wang S, Chung DDL. Self-sensing of flexural strain and damage in carbon fiber polymer-matrix composite by electrical resistance measurement. Carbon 2006;44:2739-51.

[161] Wen S, Chung D. Self-sensing of flexural damage and strain in carbon fiber reinforced cement and effect of embedded steel reinforcing bars. Carbon 2006;44:1496-502.

[162] Grant E, Livingston F, Craver M, Hegarty-Craver M, McMaster S. Characterizing conductive yarns for pressure sensors applications. SENSORS, 2015 IEEE: IEEE; 2015. p. 1-4.

[163] Alexopoulos N, Bartholome C, Poulin P, Marioli-Riga Z. Structural health monitoring of glass fiber reinforced composites using embedded carbon nanotube (CNT) fibers. Composites Science and Technology 2010;70:260-71.

[164] Haentzsche E, Mueller R, Ruder T, Nocke A, Cherif C. Integrative manufacturing of textile-based sensors for spatially resolved structural health monitoring tasks of large-scaled composite components. Materials Science Forum: Trans Tech Publ; 2015. p. 571-8.

[165] Fernández-Toribio JC, Íñiguez-Rábago A, Vilà J, González C, Ridruejo Á, Vilatela JJ. A Composite Fabrication Sensor Based on Electrochemical Doping of Carbon Nanotube Yarns. Advanced Functional Materials 2016;26:7139-47.

[166] Wiegand N, Haupt M, Mäder E, Cherif C. A Comparative Study on the Textile Processing of Carbon and Multifunctional Glass Fiber Sensor Yarns for Structural Health Monitoring. Advanced Engineering Materials 2015.

[167] Onggar T, Häntzsche E, Nocke A, Hund R, Cherif C. Sensor yarns for real-time in situ detection of damage behavior for the purpose of structural health monitoring of textile-reinforced thermoset composites: development of a continuous wet-chemical silvering process for high-performance filament yarn. Smart Materials and Structures 2017;26:045013.

[168] Sebastian J, Schehl N, Bouchard M, Boehle M, Li L, Lagounov A, et al. Health monitoring of structural composites with embedded carbon nanotube coated glass fiber sensors. Carbon 2014;66:191-200.

[169] He D, Fan B, Zhao H, Lu X, Yang M, Liu Y, et al. Design of Electrically Conductive Structural Composites by Modulating Aligned CVD-Grown Carbon Nanotube Length on Glass Fibers. ACS Applied Materials & Interfaces 2017.

[170] Luo S, Obitayo W, Liu T. SWCNT-thin-film-enabled fiber sensors for lifelong structural health monitoring of polymeric composites - From manufacturing to utilization to failure. Carbon 2014;76:321-9.

[171] Wiegand N, Mäder E. Multifunctional Interphases: Percolation Behavior, Interphase Modification, and Electro-Mechanical Response of Carbon Nanotubes in Glass Fiber Polypropylene Composites. Advanced Engineering Materials 2015.

[172] Hong J, Pan Z, Yao M, Zhang X. Preparation and properties of continuously produced conductive UHMWPE/PANI composite yarns based on in-situ polymerization. Synthetic Metals 2014;193:117-24.

[173] Hong J, Pan Z, Tian L, Yao M, Wang H, Chen J, et al. Continuous fabrication of conductive UHMWPE yarns based on in-situ polymerization with different doping acids. Synthetic Metals 2015;209:512-20.

[174] Park HJ, Kim W-J, Ah CS, Jun Y, Yun YJ. Solution-processed Au–Ag core–shell nanoparticle-decorated yarns for human motion monitoring. RSC Advances 2017;7:10539-44.

[175] Haentzsche E, Mueller R, Huebner M, Ruder T, Unger R, Nocke A, et al. Manufacturing technology of integrated textile-based sensor networks for in situ monitoring applications of composite wind turbine blades. Smart Materials and Structures 2016;25:105012.

[176] Trifigny N, Kelly FM, Cochrane C, Boussu F, Koncar V, Soulat D. PEDOT: PSS-based piezo-resistive sensors applied to reinforcement glass fibres for in situ measurement during the composite material weaving process. Sensors 2013;13:10749-64.

[177] Risicato J-V, Kelly F, Soulat D, Legrand X, Trümper W, Cochrane C, et al. A complex shaped reinforced thermoplastic composite part made of commingled yarns with integrated sensor. Applied Composite Materials 2015;22:81-98.

[178] Liu Y, Levitt A, Kara C, Sahin C, Dion G, Dandekar KR. An improved design of wearable strain sensor based on knitted RFID technology. Antenna Measurements & Applications (CAMA), 2016 IEEE Conference on: IEEE; 2016. p. 1-4.

[179] Zhu F, Hu J, Zhang H, Shi J, Yang X. Breathing measurement on the basis of contact resistance of cross-overlapping conductive yarns. Fibers and Polymers 2017;18:369-75.

[180] Haentzsche E, Mueller R, Bardl G, Nocke A, Cherif C. Warp Knitted Textile-Based Sensors for In-Situ Structural Health Monitoring of Wind Turbine Blades. Journal of Fashion Technology & Textile Engineering 2016;2016.

[181] Foroughi J, Spinks GM, Aziz S, Mirabedini A, Jeiranikhameneh A, Wallace GG, et al. Knitted Carbon-Nanotube-Sheath/Spandex-Core Elastomeric Yarns for Artificial Muscles and Strain Sensing. ACS nano 2016;10:9129-35.

[182] Zhu B, Yu T, Zhang H, Tao X. Experimental investigation of formability of commingled woven composite preform in stamping operation. Composites Part B: Engineering 2011;42:289-95.

[183] JERKOVIC I, Dufour C, Legrand X, Tao X, Boussu F, GRANCARIC AM, et al. E-glass/polypropylene sensor yarns developed by roll to roll coating procedure. 2015.

[184] GRANCARIC AM, JERKOVIC I, Dufour C, BOUSSU F, LEGRAND X, KONCAR V. Glass/polypropylene sensor yarns integration during weaving of 2D structure. polymer composites (CPC) 2015;5:6.

[185] Dufour C, Jerkovic I, Boussu F, Wang P, Soulat D, Grancaric AM, et al. Global and local observations of 3D warp interlock fabric behaviour during forming process. AIP Conference Proceedings: AIP Publishing; 2016. p. 170017.

[186] Abot JL, Silva EC, Kiyono CY, Thomas GP. Strain Gauge Sensors Comprised Of Carbon Nanotube Yarn: Concept, Modeling and Fabrication. Blucher Material Science Proceedings 2014;1:101-.

[187] Atalay O, Kennon WR, Husain MD. Textile-based weft knitted strain sensors: Effect of fabric parameters on sensor properties. Sensors 2013;13:11114-27.

[188] Peng XQ, Cao J. A continuum mechanics-based non-orthogonal constitutive model for woven composite fabrics. Composites Part A: Applied Science and Manufacturing 2005;36:859-74.

[189] Xue P, Peng X, Cao J. A non-orthogonal constitutive model for characterizing woven composites. Composites part A: Applied Science and manufacturing 2003;34:183-93.

[190] Milani AS, Nemes JA, Abeyaratne RC, Holzapfel GA. A method for the approximation of non-uniform fiber misalignment in textile composites using picture frame test. Composites Part A: Applied Science and Manufacturing 2007;38:1493-501.

[191] Harrison P. Normalisation of biaxial bias extension test results considering shear tension coupling. Composites Part A: Applied Science and Manufacturing 2012;43:1546-54.

[192] King MJ, Jearanaisilawong P, Socrate S. A continuum constitutive model for the mechanical behavior of woven fabrics. International journal of solids and structures 2005;42:3867-96.

[193] Lin G, Yuan X, Luo X, He G, Tan H. Effect of misalignment on shear response of plain woven fabric in picture frame test: experiments and finite element modelling. The Journal of The Textile Institute 2015;107:1296-304.

[194] Hivet G, Duong AV. A contribution to the analysis of the intrinsic shear behavior of fabrics. Journal of Composite Materials 2010;45:695-716.

[195] Lin G, Yuan X, Luo X, He G, Tan H. Effect of misalignment on shear response of plain woven fabric in picture frame test: experiments and finite element modelling. The Journal of The Textile Institute 2016;107:1296-304.

[196] Lomov SV, Willems A, Verpoest I, Zhu Y, Barburski M, Stoilova T. Picture Frame Test of Woven Composite Reinforcements with a Full-Field Strain Registration. Textile Research Journal 2016;76:243-52.

[197] Zhang Y, Sun F, Wang Y, Chen L, Pan N. Study on intra/inter-ply shear deformation of three dimensional woven preforms for composite materials. Materials & Design 2013;49:151-9.

[198] Harrison P, Abdiwi F, Guo Z, Potluri P, Yu WR. Characterising the shear–tension coupling and wrinkling behaviour of woven engineering fabrics. Composites Part A: Applied Science and Manufacturing 2012;43:903-14.

[199] Zhu D, Mobasher B, Vaidya A, Rajan SD. Mechanical behaviors of Kevlar 49 fabric subjected to uniaxial, biaxial tension and in-plane large shear deformation. Composites Science and Technology 2013;74:121-30.

[200] Komeili M, Milani AS. On effect of shear-tension coupling in forming simulation of woven fabric reinforcements. Composites Part B: Engineering 2016;99:17-29.

[201] Kashani MH, Rashidi A, Crawford BJ, Milani AS. Analysis of a two-way tension-shear coupling in woven fabrics under combined loading tests: Global to local transformation of non-orthogonal normalized forces and displacements. Composites Part A: Applied Science and Manufacturing 2016;88:272-85.

[202] Kashani MH, Rashidi A, Crawford BJ, Milani AS. Analysis of a two-way tension-shear coupling in woven fabrics under combined loading tests: Global to local transformation of non-orthogonal normalized forces and displacements. Composites Part A: Applied Science and Manufacturing 2016;88:272-85.

[203] Peng XQ, Cao J, Chen J, Xue P, Lussier DS, Liu L. Experimental and numerical analysis on normalization of picture frame tests for composite materials. Composites Science and Technology 2004;64:11-21.

[204] Hosseini A, Kashani MH, Sassani F, Milani AS, Ko FK. Identifying the distinct shear wrinkling behavior of woven composite preforms under bias extension and picture frame tests. Composite Structures 2018;185:764-73.

[205] Sun F, Zhang Y, Chen L, Zhang M, Pan N. Shear properties of three-dimensional woven composite reinforcements. Polymer Composites 2017;38:244-51.

[206] Rashidi A, Milani AS. A multi-step biaxial bias extension test for wrinkling/de-wrinkling characterization of woven fabrics: Towards optimum forming design guidelines. Materials & Design 2018;146:273-85.

[207] Harrison P, Taylor E, Alsayednoor J. Improving the accuracy of the uniaxial bias extension test on engineering fabrics using a simple wrinkle mitigation technique. Composites Part A: Applied Science and Manufacturing 2018;108:53-61.

[208] Alsayednoor J, Lennard F, Yu WR, Harrison P. Influence of specimen pre-shear and wrinkling on the accuracy of uniaxial bias extension test results. Composites Part A: Applied Science and Manufacturing 2017;101:81-97.

[209] Gupta TD, Gacoin T, Rowe A. Piezoresistive Properties of Ag/Silica Nano-Composite Thin Films Close to the Percolation Threshold. Advanced Functional Materials 2014;24:4522-7.

[210] Lee C, Jug L, Meng E. High strain biocompatible polydimethylsiloxane-based conductive graphene and multiwalled carbon nanotube nanocomposite strain sensors. Applied Physics Letters 2013;102:183511.

[211] Vidhate S, Chung J, Vaidyanathan V, D'Souza N. Time dependent piezoresistive behavior of polyvinylidene fluoride/carbon nanotube conductive composite. Materials Letters 2009;63:1771-3.

[212] Wang M, Zhang K, Dai XX, Li Y, Guo J, Liu H, et al. Enhanced electrical conductivity and piezoresistive sensing in multi-wall carbon nanotubes/polydimethylsiloxane nanocomposites via the construction of a self-segregated structure. Nanoscale 2017.

[213] Rizvi R, Cochrane B, Biddiss E, Naguib H. Piezoresistance characterization of poly(dimethyl-siloxane) and poly(ethylene) carbon nanotube composites. Smart Materials and Structures 2011;20:094003.

[214] Zhang R, Baxendale M, Peijs T. Universal resistivity–strain dependence of carbon nanotube/polymer composites. Physical Review B 2007;76:195433.

[215] Pandey G, Wolters M, Thostenson ET, Heider D. Localized functionally modified glass fibers with carbon nanotube networks for crack sensing in composites using time domain reflectometry. Carbon 2012;50:3816-25.

[216] Yap HW, Lakes RS, Carpick RW. Mechanical instabilities of individual multiwalled carbon nanotubes under cyclic axial compression. Nano letters 2007;7:1149-54.

[217] Souri H, Nam IW, Lee HK. Electrical properties and piezoresistive evaluation of polyurethane-based composites with carbon nano-materials. Composites Science and Technology 2015;121:41-8.

[218] Karahan Toprakci HA. Pizoresistive Properties of Polyvinyl Chloride Composites. 2012.

[219] Toprakci HAK, Kalanadhabhatla SK, Spontak RJ, Ghosh TK. Polymer Nanocomposites Containing Carbon Nanofibers as Soft Printable Sensors Exhibiting Strain-Reversible Piezoresistivity. Advanced Functional Materials 2013;23:5536-42.

[220] Daelemans L, Faes J, Allaoui S, Hivet G, Dierick M, Van Hoorebeke L, et al. Finite element simulation of the woven geometry and mechanical behaviour of a 3D woven dry fabric under tensile and shear loading using the digital element method. Composites Science and Technology 2016;137:177-87.

[221] Colman A, Bridgens B, Gosling P, Jou G-T, Hsu X-Y. Shear behaviour of architectural fabrics subjected to biaxial tensile loads. Composites Part A: Applied Science and Manufacturing 2014;66:163-74.

[222] Harrison P, Abdiwi F, Guo Z, Potluri P, Yu W. Characterising the shear–tension coupling and wrinkling behaviour of woven engineering fabrics. Composites Part A: Applied Science and Manufacturing 2012;43:903-14.

[223] Kashani MH, Hosseini A, Sassani F, Ko FK, Milani AS. Understanding different types of coupling in mechanical behavior of woven fabric reinforcements: A critical review and analysis. Composite Structures 2017;179:558-67.

[224] Milani A, Nemes J, Abeyaratne R, Holzapfel GA. A method for the approximation of non-uniform fiber misalignment in textile composites using picture frame test. Composites Part A: Applied Science and Manufacturing 2007;38:1493-501.